THEORETICAL STUDIES ON THE ULTRAFAST PHOTODISSOCIATION OF MOLECULES.

by

EMMA LOUISE CHAPMAN

A thesis submitted to
the University of Birmingham
for the examination of
DOCTOR OF PHILOSOPHY

School of Chemistry
University of Birmingham
July 2009

Abstract

Ultrafast photodissociation is a fundamental process in nature. In this thesis we present a study of three very different systems which undergo photodissociation on the femtosecond timescale. A major feature of these processes is the often complex topology of the potential energy surfaces due to coupling between the nuclear and electron motion: termed vibronic coupling.

A known feature in potential energy surfaces due to vibronic coupling is the conical intersection and these play a role in all three systems studied. In the first study we investigate NH_3, which exhibits an intersection between the ground and first excited state. As a consequence the dissociation occurs on both states. We use two models to study this system, a 2D and a 6D, contrasting greatly in their complexity and ability to describe the whole molecule. Wavepacket dynamics are used to probe the reaction mechanism and to calculate the branching ratio.

A detailed investigation of electronic structure theory methods forms a large part of this research. We apply it to the FNO molecule, a system in which there is coupling amongst the states giving rise to certain topological features on the first excited state. These features are both subtle and difficult to reproduce with *ab initio* methods. We also present a potential fit of this data and implement wavepacket dynamics simulations on the surfaces.

A study of $Cr(CO)_6$ using electronic structure theory is the final system investigated in this work. In contrast to the other systems, $Cr(CO)_6$ has many low lying excited electronic states and we investigate this system using Complete Active Space Self-Consistent Field (CASSCF) methods. Using a large active space allows us to include all of the states of interest within one calculation.

Acknowledgements

Firstly I would like to express my gratitude to my supervisor Dr Graham Worth who has given me much support and encouragement throughout my PhD. Not only a source of knowledge whenever I needed it, and it was often, but I must also thank him for his kindness and patience when the going got tough.

I have made many great friends since coming to Birmingham and would like to thank everyone from the Worth, Johnston, Tremayne and Britton groups, past and present, Andy Bennett, Liana Vella Zarb, Adam and Nicola Cowell, Dan Binks, Heather Rose, Oliver Paz Borbon, Duncan Bell and Andy Logsdail. I would also like to thank Jan Novak and Jon Smale for their proof reading skills and Tom Penfold for all the computational help.

I would like to give special thanks to Kousik Giri for all his help with ammonia and for his infinite patience and attention to detail. Special thanks also to Cristina Sanz Sanz who has shared her knowledge with me and pointed me in the right direction when I needed it.

Finally I would like to thank my family and especially my mum for help in difficult times and my partner Guy, whose continued support has been unwavering and invaluable throughout my PhD.

This thesis and the work described in it are entirely my own, except where I have acknowledged *either* help from a named person *or* a reference is given to a published source or a thesis. Text taken from another source will be enclosed in quotation marks and a reference will be given.

August 12, 2009

Contents

List of Figures

List of Tables

Glossary

$-\frac{\hbar^2}{2m}\frac{d^2\psi(x)}{dx^2} + V(x)\psi(x) = E\psi(x)$ Time-independent Schrödinger equation

$\hat{H} = -\frac{\hbar^2}{2m}\nabla^2\Psi(\mathbf{x},t) + V(\mathbf{x})$ Hamiltonian operator

$\hbar = \frac{h}{2\pi}$ h bar

$\nabla^2 = \frac{\partial^2}{\partial x^2} + \frac{\partial^2}{\partial y^2} + \frac{\partial^2}{\partial z^2}$ Laplacian

$i\hbar\frac{\partial}{\partial t}\Psi(\mathbf{x},t) = \hat{H}\Psi(\mathbf{x},t)$ Time-dependent Schrödinger equation

BO Born Oppenheimer

C(t) Time autocorrelation function

CAP Complex absorbing potential

CAS Complete active space

CASPT2 Complete active space with second-order perturbation theory

CASSCF Complete active space self consistent field

CGTO Contracted Gaussian type orbitals

CI Conical intersection

COM Centre of mass

CSF Configuration state function

CT Charge transfer

DOF Degrees of freedom

DVR Discrete variable representation

ECP Effective Core Potential

EOM-CCSD Equation-of-motion coupled cluster singles and doubles

ET Electron transfer

FBR Finite basis representation

FC Franck Condon

FFT Fast Fourier transform

fs Femtosecond

GTO Gaussian type orbitals

HDMR High-dimensional model representation

HF Hartree Fock

HOMO Highest occupied molecular orbital

i $= \sqrt{-1}$

JT Jahn-Teller

KE Kinetic energy

LF Ligand field

LUMO Lowest unoccupied molecular orbital

LVC Linear vibronic coupling

MC Metal centred

MC-QDPT Multi-configuration quasi-degenerate perturbation theory

MCSCF Multi-configuration self consistent field

MCTDH Multiconfiguration time-dependent hartree

MLCT Metal-to-ligand charge transfer

MRCI multi-reference configuration interaction

PES Potential energy surfaces

ps picosecond

SCF Self consistent field

STO Slater type orbitals

UV Ultra violet

VEE Vertical Excitation Energy

VMI Velocity map imaging

Chapter 1

Introduction

The breaking of a chemical bond induced by the absorption of one or more photons is termed photodissociation. These reactions occur at the femtosecond, 10^{-15}s, timescale and have invoked much interest both from experimentalists and theoreticians due to their fundamental nature in chemistry. Chemical reactions involving the absorption of light are many and varied and the importance of our understanding of them is evident in many areas of science, for example in atmospheric chemistry, biochemistry and physics. Photosynthesis in plants and the production of ozone are examples of reactions where photochemistry occurs and are both vital for the sustainability of life on earth.

In the ozone cycle [1, 2] ultra violet (UV) radiation from the sun causes O_2 to dissociate giving 2 oxygen atoms which can then react with more O_2 to form ozone, O_3,

$O_2 + h\nu \rightarrow 2O$

$O + O_2 + M \rightarrow O_3 + M$

where M indicates a third body required for the conservation of energy.

Ozone itself also undergoes dissociation when excited by particular wavelengths of UV light

$O_3 + h\nu \rightarrow O + O_2$

whereupon the oxygen atom may combine with O_2 to reform ozone or may react with an oxygen atom from another ozone molecule to form O_2

$O + O_2 \rightarrow O_3$ or

$O_3 + O \rightarrow 2O_2$.

The highest levels of ozone are found in the stratosphere where it absorbs harmful UV radiation from the sun protecting us from an increased risk of skin cancer. It is important that we have a detailed understanding of the dissociation mechanisms involved in processes such as the ozone cycle which are so vital to life on earth.

Recent advances in the development of laser technology [3] have made it possible to observe ultrafast photodissociation in real time and with major developments in time dependent quantum mechanical methodology, a high level of correlation between experiment and theory is now achievable.

Many experimental studies have been carried out on systems undergoing photodissociation and classic examples of this are cyanogen iodide, ICN, and sodium iodide, NaI, on which pioneering pump probe studies were carried out by Zewail *et al* [4–6]. This type of experiment involves two laser pulses, a pump and a probe pulse. The ultrashort pump pulse initiates the reaction by excitation of the sample. After an appropriate time delay the probe pulse is used to monitor the reaction. The time delay between the pump and probe pulses can be varied and measurements taken as a function of time. With this technique the process of bond breaking can be viewed in real time.

Experimental real time studies of the reaction of I-CN → [I ⋯ CN] → I + CN have shown that it takes 205 ± 30 fs for complete dissociation to occur and that following electronic excitation ICN dissociates through two exit channels [7, 8]

$$\begin{aligned} \mathrm{ICN} + h\nu &\rightarrow \mathrm{I}(^2\mathrm{P}_{3/2}) + \mathrm{CN}(\mathrm{X}^2\Sigma^+) \\ &\rightarrow \mathrm{I}^*(^2\mathrm{P}_{1/2}) + \mathrm{CN}(\mathrm{X}^2\Sigma^+) \end{aligned}$$

where iodine atoms are produced either in the ground spin-orbit state, $I(^2P_{3/2})$, or in the excited state, $I^*(^2P_{1/2})$. For both channels CN is produced in its ground electronic state, ($X^2\Sigma^+$). Figure 1.1 shows a schematic representation of the potential energy curves of ICN. After excitation to the repulsive excited state by a pump pulse set at 306 nm the reaction is probed for the formation of the free CN radical which can be monitored by laser-induced fluorescence. The probe is set to 388.5 nm, the absorption peak for free CN.

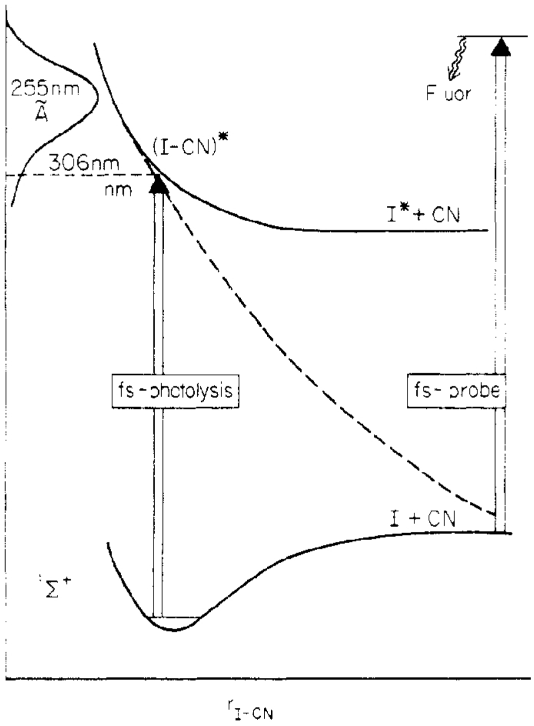

Fig. 1.1: Schematic representation of the ICN potential energy curves taken from Zewail *et al* [9] showing the vertical excitation from the ground to the excited state.

NaI is a good example of one of the features that arise in photodissociation reactions, that of the avoided crossing. The non-crossing rule states that in a 1D system potential energy curves corresponding to electronic states of the same symmetry cannot cross. If we consider NaI we see that there are two states, one ionic and one covalent, which at some point cross with each other. The ground state undergoes a change in character from ionic $Na^+ + I^-$ to Na + I in atomic form. To obtain the best description of the wavefunction for NaI it is necessary to consider a mixing of these two states.

This mixing causes the two states to repel one another and at the crossing point the curves now exhibit an avoided crossing. However the case for polyatomic molecules is different in that states of the same symmetry may cross and form a conical intersection (CI) [10–13] and it is found to be a common occurrence in photochemical reactions of polyatomic molecules [14, 15]. An avoided crossing or CI provides a pathway for the molecule to cross between states and is one of the reasons why this area of chemistry invokes so much interest to experimentalists and theoreticians alike.

For NaI the ionic and covalent potential energy curves as a function of internuclear separation, R, are shown in figure 1.2. The study showed that on initial excitation

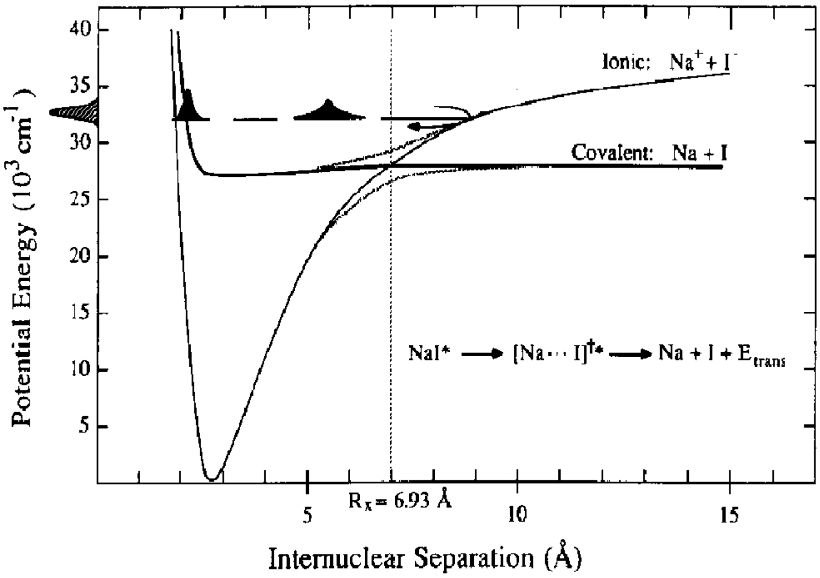

Fig. 1.2: Schematic representation of the NaI potential energy curves showing the avoided crossing between the covalent and ionic states taken from Zewail *et al* [16].

by the pump pulse that Na^+I^- was promoted to the covalent surface. As the bond dissociates the probe monitors the wavepacket. The wavepacket proceeds along this covalent surface whereupon it encounters the avoided crossing between the two states at $R = 6.93$ Å. At this point a small portion of the wavepacket continues along the covalent curve, via the avoided crossing, where it finds its way to dissociation to produce Na + I. The larger portion of the wavepacket follows the ionic potential but does not have enough energy to produce $Na^+ + I^-$ and so it oscillates back and forth with a small portion of the wavepacket yielding Na + I each time it encounters the crossing. The experimental realisation for this is shown in a plot of the oscillation of the wavepacket in the well in figure 1.3. Each peak on the lower plot corresponds to the wavepacket returning to its initial position and over time it can be seen that there is a definite decay as more Na + I is produced. The upper plot in figure 1.3 is a measure of the amount of neutral Na produced over time and of course this increases stepwise as the reaction proceeds.

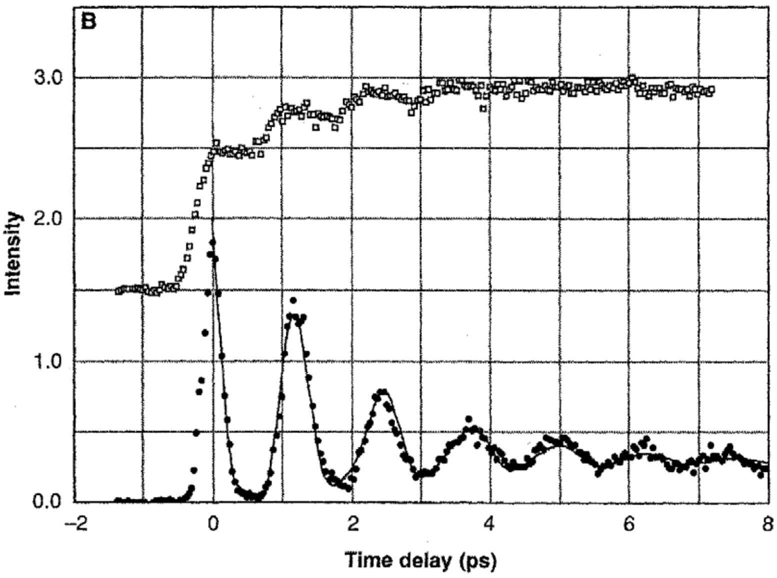

Fig. 1.3: The lower plot shows the oscillation of the NaI wavepacket and the upper plot the amount of neutral Na produced over time. Reproduced from Zewail *et al* [4]

The aforementioned examples illustrate the detailed information that can be obtained experimentally using ultrafast laser techniques. We now turn our attention to theoretical methods. Many theoretical quantum mechanical studies have been carried out on systems which undergo photodissociation. Examples include CINO [17], H_2O [18], H_2S [19], CH_3ONO [20,21] and CH_3I [22]. Major developments in theoretical methods in recent years are evident in these studies. Multi-dimensional potential energy surfaces (PES) have been calculated for each of these systems for their ground and excited states using *ab initio* methods. The advances of theoretical methods mean that it is now possible to study complex systems in detail and at time scales corresponding to bond breaking and formation.

By studying systems that undergo ultrafast photodissociation scientists are coming closer to achieving one of the ultimate goals in chemistry, to be able to control the outcome of a reaction. Photodissociation plays a fundamental role in the advancement of coherent control with the use of lasers. As well as using femtosecond lasers to probe chemical reactions such as NaI and ICN they can also be used for the control of selective bond breaking. One such example is the control of the reaction of HOD with H atoms [23, 24]. The two product channels of the reaction are

$H + HOD \rightarrow H_2 + OD$ and

$H + HOD \rightarrow HD + OH$.

The fact that the O-H and O-D frequencies are well separated, 3706 and 2727 cm^{-1} respectively, means that each bond can be stretched independently. A study by Crim *et al* [25] found that if they excited the third overtone of the O-H stretching vibration that the products H_2 + OD were produced at least two orders of magnitude more frequently than the other outcome. Similarly the dissociation of HOD has been studied [26]. The reaction yields either OH + D or OD + H and by excitation with UV light corresponding to the first excited state the product ratio can be controlled. By exciting the third overtone of the HO-D vibration, the products D + OH are exclusively selected for [27].

One of the simplest physical observables of any study on photodissociation, experimental or theoretical, is the absorption spectrum for a particular molecule. From this, much information can be obtained about energy levels, molecular geometries and the nature of chemical bonds. Quite often the spectrum is obtained experimentally using spectroscopy and although this is a vital tool for examining atomic and molecular structure, it does not provide a complete insight into the mechanism of the dissociation reaction.

In order to delve more deeply into the mechanisms of these reactions, we look to computer simulation methods. Theoretical quantum mechanical techniques enable scientists to probe the mechanisms of these reactions on a state to state level yielding information which cannot be obtained experimentally by spectroscopy. Central to this approach is the ability to solve the Schrödinger equation

$$i\hbar\frac{\partial\Psi}{\partial t} = \hat{H}\Psi(\mathbf{x},t) \tag{1.1}$$

and for this to be achieved for all but the simplest of systems we turn to the Born-Oppenheimer (BO) approximation. The fact that the mass of the nuclei is much larger than that of the electrons means that the electrons react instantaneously to changes in position of the nuclei and as a consequence the nuclear and electronic motion can be separated. The physical picture created here of the nuclei moving on a single PES created by the electrons is a familiar one. As a result, the general procedure for a theoretical study is firstly to generate the PES on which the dynamics will be carried out, secondly to carry out the wavepacket dynamics and thirdly to analyse the results. Generating the PES is usually carried out using electronic structure theory, or *ab initio* methods, and really it is this step which dictates the validity of the succeeding steps. Calculation of PES can be an arduous task but the importance of their accuracy cannot be stressed too highly.

The basis for generating the PES is the ability to solve the time-independent electronic Schrödinger equation. This is carried out within the BO approximation where the nuclei are held at various fixed geometries and the Schrödinger equation is solved for the electrons. PES obtained in this way are termed *adiabatic.* It is a common occurrence in photodissociation processes that two PES can become degenerate at some point and intersect with one another and form a CI. For reactions where a CI is involved it is not possible to separate the electronic and nuclear motions at the intersection and as a consequence the BO approximation is no longer valid.

An example of a CI between two states is shown in figure 1.4 showing the characteristic cone shape (taken from Cederbaum *et al* [14]). A CI between two PES facilitates the ultrafast radiationless decay of an excited state and there are some very prominent examples in nature where this occurs. Photosynthesis has been widely studied [28–30] but perhaps one of the most intriguing aspects of this process is the electron transfer (ET) which occurs from reduced pheophytin to the photosynthetic acceptor quinone. This initial ET initiates the start of a flow of electrons down an electron transport chain and is fundamental to the whole process. It is now known that the ET between pheophytin and quinone takes place via a CI [31] and that it occurs at the femtosecond timescale. Another well documented example is the cis-trans isomerisation reaction of retinal in the eye [32]. When light enters the eye it is absorbed by rhodopsin which

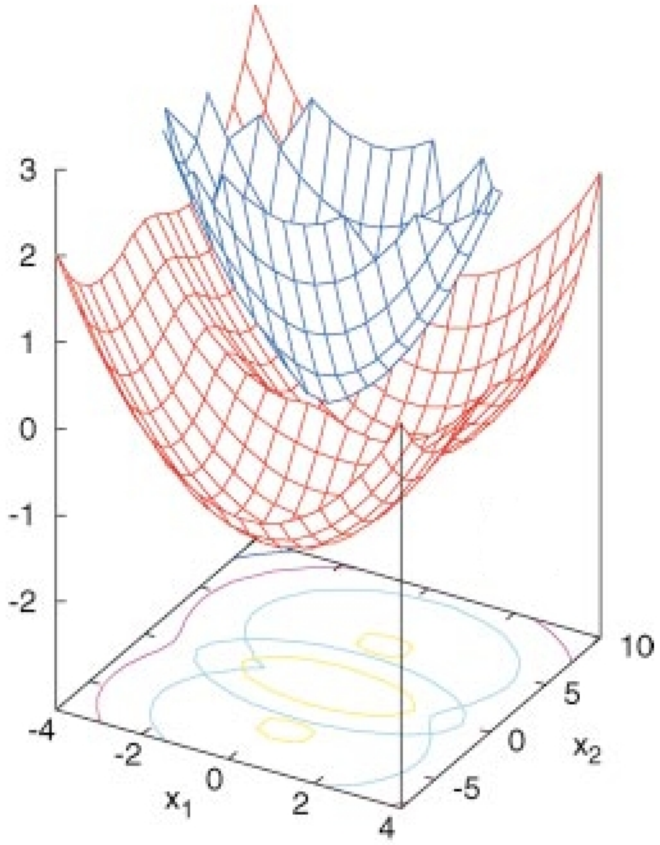

Fig. 1.4: An example of a conical intersection between two electronic states [14].

is composed of cis-retinal. The photoisomerisation of cis-retinal to trans-retinal is the initial event that occurs in vision and has been shown to occur within ∼200 fs [33]. Theoretical studies carried out on models of the retinal chromophore have shown the presence of a CI [34]. Taken from Stock *et al* [35] figure 1.5 shows the photoisomerisation of retinal modelled by a two state system where the wavepacket can be seen bifurcating, dividing into two parts, at the CI where the major part of it reaches the ground state trans configuration at t = 200 fs.

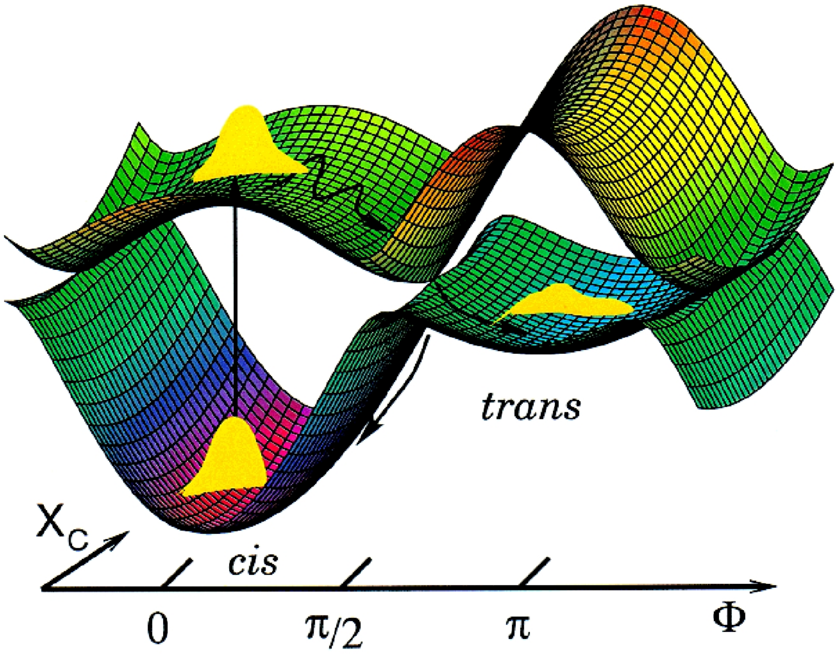

Fig. 1.5: The adiabatic PES of the cis-trans isomerisation of retinal taken from Stock *et al* [35] showing the wavepacket bifurcating at the conical intersection.

When a CI is present it is usual to turn to the *diabatic* representation. In the adiabatic representation there are terms due to the nuclear kinetic energy (KE) that couple the PES and at the point of an avoided crossing or an intersection these coupling terms can no longer be ignored and become singular. Staying in the adiabatic basis makes these terms very difficult to deal with computationally whereas in the diabatic basis the coupling terms can be dealt with more easily. By solving the time-dependent Schrödinger equation the dynamics can be implemented yielding results that show a wavepacket evolving in time across a PES. A visual display of the dissociative process in terms of its electronic states offers an insight unobtainable with experimental techniques.

In this study we look at the ultrafast photodissociation of three molecules, ammonia, NH_3, nitrosyl fluoride, FNO and chromium hexacarbonyl, $Cr(CO)_6$. These three molecules exhibit different aspects of photodissociation and require very different approaches.

NH_3 exhibits a CI between the ground and first excited states and as a result of this the reaction proceeds both adiabatically in the first excited state or non-adiabatically via the CI in the ground state. To investigate NH_3 we will use PES previously calculated by Truhlar *et al* to implement the wavepacket dynamics. The dynamics will be carried out on the diabatic ground and first excited states. Two models will be used, a 2D and a 6D, both encompassing the umbrella bending mode of NH_3 to which the main progression in the absorption spectrum is attributed. In this context 2D and 6D refer to the DOF included in the model with the 2D allowing motion of one proton relative to the rest of the molecule via an N-H bond length and a single angle. The 6D model contains 6 DOF represented by 3 angles and 3 N-H bond lengths.

The 2D model will offer a simplified representation of the umbrella bending mode of NH_3 which is excited in the first excited electronic state and precedes the dissociation of the N-H bond. The 6D model in contrast to the 2D will provide a more accurate description of the total system and will make an interesting comparison with the 2D model in terms of the spectrum and the dynamics. The 6D model is a challenging prospect in terms of the fitting of the PES and carrying out the wavepacket dynamics. The use of the 6D model surpasses any previous work carried out on this system. Absorption spectra will be generated for both models and analysis carried out to ascertain the branching ratios.

For FNO the aim is to calculate the PES from scratch for the ground and low lying singlet excited states using *ab initio* electronic structure calculations. This will form the major part of the study for this molecule and a range of methods will be used. The starting point will be the Complete Active Space Self Consistent Field (CASSCF) method where a full valence active space will be used. The CASSCF wavefunction will then be used as a reference wavefunction for the Complete Active Space with Second-Order Perturbation Theory (CASPT2) and Multi-Reference Configuration Interaction (MRCI) methods, which, unlike the CASSCF will account for dynamic correlation. Creating surfaces with these different methods will provide a thorough study with respect to the advantages and disadvantages of each method and how well they perform in the dissociative region. Such a thorough study of the PES has not been undertaken before. The adiabatic PES will be then be used to carry out time-dependent wavepacket dynamics to generate the absorption spectrum. As a comparison to the *ab initio* surfaces we will investigate the technique of fitting an analytical function to the data points and creating a model potential. The couplings between the states will be calculated so that a more thorough understanding of this system can be gained in terms of the influence of the higher excited states on the $1^1A''$ state and how this affects the spectrum. The level of calculations used in this study will supercede any previous work and investigation of the coupling between the excited states will provide a new insight into the photodissociation of the molecule.

In the context of electronic states $Cr(CO)_6$ is a molecule which possesses many of them at low lying energies. On photodissociation $Cr(CO)_6$ loses a single CO ligand and in this study extensive calculations will be carried out using the CASSCF method to calculate potential energy curves along the dissociation coordinate. A thorough study of different active spaces will be carried out with regard to previous work. This molecule is a classic example of how the choice of active space can affect the results in terms of the ordering of the states. We will extend on previous theoretical studies by using a larger CAS space than has been used before to include all the states of interest within one calculation. It is well established that the mechanism for photodissociation for this molecule is a complex one and although numerous studies have been carried out the results show variations as to the ordering of the electronic states and, therefore, discrepancies as to which states are involved in the dissociation.

There is no doubt that photodissociation reactions are complex and varied and play an important role in many of the fundamental reactions that occur in nature. The ultrafast timescales at which these reactions occur aided by the presence of a CI makes them a challenging prospect for investigation both experimentally and computationally.

Chapter 2

Theory: Solving the Time-Dependent Schrödinger Equation

2.1 Introduction

An overview of the theory which underlies this study will be given in this chapter. Central to this investigation is the ability to solve the Schrödinger equation. Starting with the full time-dependent Schrödinger equation and integrating out the electronic degrees of freedom (DOF) from this leads logically on to the BO approximation within which the adiabatic PES are generated. To generate the surfaces we require solutions to the clamped nuclei eigenvalue equation. Whilst the nuclei are held at fixed geometries, the Schrödinger equation is solved for the electrons which depend only parametrically on the nuclear coordinates. The PES obtained from this are termed adiabatic. Although the nuclear and electronic motion are treated separately in the adiabatic representation there are terms due to the nuclear KE operator that couple the states. If these terms are small then the BO approximation can be invoked and these terms can be ignored. As is commonly the case with photodissociation reactions, where two or more electronic states couple with each other, a CI is formed making it possible for molecules to make the transition between electronic states [36]. It is in the region of a CI where the coupling terms become large and the BO approximation breaks down. It is then more convenient to consider the diabatic representation where the coupling terms are contained within the potential.

Calculating PES has formed a major part of this study and the technique of potential fitting will be described here. A model Hamiltonian is constructed from the fitting of an analytical function to data points obtained from *ab initio* calculations.

2.2 The Schrödinger Equation

The time-dependent Schrödinger equation is written

$$i\hbar\frac{\partial}{\partial t}\Psi(\mathbf{x},t) = \hat{H}\Psi(\mathbf{x},t) \tag{2.1}$$

where Ψ is the wavefunction dependent on time, $\mathbf{x}$ are the nuclear and electron coordinates and i is $\sqrt{-1}$. $\hat{H}$ is the Hamiltonian operator which contains the kinetic and potential energy terms

$$\hat{H} = -\frac{\hbar^2}{2m}\nabla^2 + V(\mathbf{x}) \tag{2.2}$$

where $\nabla^2 = \frac{\partial^2}{\partial x^2} + \frac{\partial^2}{\partial y^2} + \frac{\partial^2}{\partial z^2}$ and is known as the Laplacian and $V(\mathbf{x})$ is the time-independent potential energy. Equation 2.1 contains the derivative of Ψ with respect to time which means that if Ψ is known at time $t = 0$ then it can be calculated at some later time t. The physical significance of the wavefunction is that $|\Psi|^2 d\tau = \Psi^*\Psi$ is the probability density, where Ψ^* is the complex conjugate of Ψ. In other words the probability of finding a particle in the volume element $d\tau$ is proportional to the square of the wavefunction. The square of a normalised wavefunction has a value of 1,

$$\int_{-\infty}^{\infty} \Psi^*\Psi d\tau = 1. \tag{2.3}$$

The time-independent Schrödinger equation can be derived from the time-dependent form. As long as the potential energy, V, is time-independent the time and space dependent parts of equation 2.1 can be separated and written as

$$\Psi(\mathbf{x},t) = f(t)\psi(\mathbf{x}). \tag{2.4}$$

Substituting this into equation 2.1 gives

$$i\hbar\frac{\partial f(t)}{\partial t}\psi(\mathbf{x}) = -\frac{\hbar^2}{2m}\nabla^2 f(t)\psi(\mathbf{x}) + V(\mathbf{x})f(t)\psi(\mathbf{x}) \tag{2.5}$$

and then dividing both sides by $f(t)\psi$ gives

$$i\hbar\frac{1}{f(t)}\frac{\partial f(t)}{\partial t} = -\frac{\hbar^2}{2m}\frac{1}{\psi(\mathbf{x})}\frac{d^2\psi(\mathbf{x})}{dx^2} + V(\mathbf{x}). \tag{2.6}$$

The right hand side of equation 2.6 is a function of x only and is independent of a change in t, whereas the left hand side is a function of t only and is independent of a change in x. As the two sides are equal to one another there has to be some function which each side equates to that does not depend either on x or on t and must, therefore, be a constant. This constant has units of energy and is labelled as E.

Equating first the left hand side of equation 2.6 to E and then the right hand side it can be written as two separate equations

$$i\hbar\frac{\partial f(t)}{\partial t} = Ef(t) \tag{2.7}$$

$$-\frac{\hbar^2}{2m}\frac{d^2\psi(\mathbf{x})}{dx^2} + V(\mathbf{x})\psi(\mathbf{x}) = E\psi(\mathbf{x}) \tag{2.8}$$

Equation 2.7 has the solution

$$f(t) = e^{-iEt/\hbar} \tag{2.9}$$

and the complete wavefunction, $\Psi = \psi f(t)$ can be written

$$\Psi(\mathbf{x}, t) = \psi(\mathbf{x})e^{-iEt/\hbar}. \tag{2.10}$$

Equation 2.8 is the time-independent Schrödinger equation and its general form is

$$\hat{H}\psi = E\psi. \tag{2.11}$$

It is an eigenvalue equation where E is the eigenvalue and can take on certain discrete values and ψ is the eigenfunction or eigenstate.

2.3 The Clamped Nucleus Hamiltonian

In order to solve the Schrödinger equation for even the simplest of molecules the BO approximation [37, 38] must be used. This approximation is based on the fact that the mass of an electron is much smaller than that of a nucleus which means that the electrons can adjust instantaneously to changes in the positions of the nuclei. For this reason the electronic and nuclear motions can be treated separately. As a starting point, the Schrödinger equation can be solved for the electrons at fixed nuclear coordinates. The potential and KE terms for the nuclei and electrons can be separated within the Hamiltonian operator and written as

$$\hat{H} = \hat{T}_{nu} + \hat{T}_e + \hat{V}_{ne} + \hat{V}_{ee} + \hat{V}_{nn} \tag{2.12}$$

where $\hat{T}_{nu}$ and $\hat{T}_e$ are the KE operators for the nuclei and electrons and $\hat{V}_{ne}$, $\hat{V}_{ee}$ and $\hat{V}_{nn}$ are the operators for the nuclear-electron, electron-electron and nuclear-nuclear potential energies respectively. The molecular Hamiltonian is written in full as

$$\begin{aligned} \hat{H} = & - \frac{\hbar^2}{2}\sum_{\alpha}\frac{1}{m_\alpha}\nabla^2_\alpha - \frac{\hbar^2}{2m_e}\sum_i \nabla^2_i \\ & - \sum_\alpha\sum_i \frac{Z_\alpha e^2}{r_{i\alpha}} + \sum_\alpha\sum_{\beta>\alpha}\frac{Z_\alpha Z_\beta e^2}{r_{\alpha\beta}} + \sum_j\sum_{i>j}\frac{e^2}{r_{ij}} \end{aligned} \tag{2.13}$$

where α and β refer to nuclei, i and j to electrons, $r_{i\alpha}$, $r_{\alpha\beta}$ and r_{ij} refer to the distance between electron i and nucleus α, the distance between nuclei α and β with atomic numbers Z_α and Z_β and the distance between electrons i and j respectively.

If the KE of the nuclei, $\hat{T}_{nu}$, is set to zero the electronic Hamiltonian is obtained

$$\hat{H}_{el} = \hat{T}_e + \hat{V}_{ne} + \hat{V}_{ee} + \hat{V}_{nn}. \tag{2.14}$$

The operator $\hat{H}_{el}$ depends only parametrically on $\mathbf{R}$, the nuclear coordinates, and its eigenvalues, $V_i(\mathbf{R})$, and eigenfunctions, $\Phi_i(\mathbf{r};\mathbf{R})$, fulfil

$$\hat{H}_{el}\Phi_i(\mathbf{r};\mathbf{R}) = V_i(\mathbf{R})\Phi_i(\mathbf{r};\mathbf{R}) \tag{2.15}$$

where **r** denotes the electronic coordinates, or in matrix form

$$\langle \Phi_i | \hat{H}_{el} | \Phi_j \rangle = V_i \delta_{ij} \tag{2.16}$$

where $\Phi_i(\mathbf{r};\mathbf{R})$ and V_i are adiabatic eigenfunctions and eigenvalues of the electrons with the fixed nuclear coordinates as parameters and there is a set of these equations for each nuclear geometry.

2.4 The Adiabatic Representation

We now return to the full time-dependent Schrödinger equation. The total Hamiltonian, equation 2.12, can be written

$$\hat{H}(\mathbf{R},\mathbf{r}) = \hat{T}_{nu}(\mathbf{R}) + \hat{H}_{el}(\mathbf{R};\mathbf{r}). \tag{2.17}$$

The total molecular wavefunction can be expanded in terms of the adiabatic eigenfunctions, $\Phi_i(\mathbf{r};\mathbf{R})$, from the clamped nuclei equation which are the solutions to the electronic Schrödinger equation

$$\psi(\mathbf{r},\mathbf{R}) = \sum_i \chi_i(\mathbf{R})\Phi_i(\mathbf{r};\mathbf{R}) \tag{2.18}$$

where $\chi_i(\mathbf{R})$ are the expansion coefficients. Representing the wavefunction in this way means that the electronic Hamiltonian is diagonal with the nuclear KE terms off diagonal and it is these terms that couple the PES. By substituting equation 2.18 into the time-independent Schrödinger equation 2.11 multiplying from the left with $\langle \Phi_i |$ and integrating over all the electronic coordinates we get a set of coupled equations for the nuclear wavefunctions

$$\sum_j \langle \Phi_i | \hat{T}_{nu} | \Phi_j \chi_j(R) \rangle + [V_i(R) - E]\chi_i(R) = 0 \tag{2.19}$$

where the electronic states i and j are coupled through the nuclear KE operator

$$[\hat{T}_n \mathbf{1} + \hat{\mathbf{V}} - \hat{\Lambda}]\chi = i\hbar \frac{\partial \chi}{\partial t} \tag{2.20}$$

where $\hat{\mathbf{\Lambda}}$ is the non-adiabatic coupling matrix, $\hat{\mathbf{V}}$ the potential energy matrix and χ the nuclear wavefunction [36]. The coupling matrix contains the first and second derivatives $\frac{\partial}{\partial R_i}$ and $\frac{\partial^2}{\partial R_i^2}$ which means that in order to solve equation 2.19 the first and second order derivatives for the electronic wavefunctions would need to be solved. This would be an extremely complex task in the adiabatic representation and so it is usual to invoke the approximation that if the derivatives are small and this coupling can be neglected then equation 2.19 reduces to

$$[\hat{T}_{nu}(R) + V_i(R) - E]\chi_i(R) = 0 \tag{2.21}$$

where there is no coupling and V_i is a set of adiabatic PES.

2.5 Vibronic Coupling and the Diabatic Representation

Although solving the Schrödinger equation within the the BO approximation works well for many systems the approximation breaks down for ultrafast processes where vibronic coupling occurs and it is no longer possible to separate the nuclear and electronic motions. In cases where the coupling is significant these terms cannot be ignored and this is found to be particularly common in the photochemistry of polyatomic molecules. The difficulty comes when trying to calculate the derivatives of the electronic wavefunctions when in the adiabatic representation. The aim is to make these derivatives absent or as small as possible and one way of doing this is to choose the electronic basis functions to be independent of the nuclear coordinates, $\Phi(r; R) \rightarrow \Phi(r; R_0)$, so that the electronic wavefunctions do not change with nuclear geometry. This is termed the *crude adiabatic basis*. We now turn our attention to the adiabatic diabatic transformation. To change to the diabatic representation a unitary transformation is used

$$\mathbf{W} = \mathbf{S}\mathbf{V}\mathbf{S}^\dagger \tag{2.22}$$

where $\mathbf{W}$ is the diabatic potential matrix with the coupling terms contained within the potentials, $\mathbf{S}$ is a transformation matrix and $\mathbf{S}^\dagger$ its conjugate transpose. For a 2 state system, at each fixed nuclear geometry the transformation can be written

$$\begin{pmatrix} \Phi_i^d \\ \Phi_j^d \end{pmatrix} = \begin{pmatrix} \cos\alpha & \sin\alpha \\ -\sin\alpha & \cos\alpha \end{pmatrix} \begin{pmatrix} \Phi_i^a \\ \Phi_j^a \end{pmatrix} \tag{2.23}$$

where $\Phi_{i,j}^a$ and $\Phi_{i,j}^d$ are the adiabatic and diabatic electronic wavefunctions respectively and α is the mixing angle between the two adiabatic states dependent on the coordinates $\mathbf{R}$ and $\mathbf{r}$. From equation 2.23 we can write

$$W_{ii}^d = \langle\Phi_i^d|\hat{H}_{el}|\Phi_i^d\rangle = V_i^a\cos^2\alpha + V_j^a\sin^2\alpha \tag{2.24}$$

$$W_{jj}^d = \langle\Phi_j^d|\hat{H}_{el}|\Phi_j^d\rangle = V_i^a\sin^2\alpha + V_j^a\cos^2\alpha \tag{2.25}$$

for the on-diagonal terms and

$$W_{ij}^d = \langle\Phi_i^d|\hat{H}_{el}|\Phi_j^d\rangle = (V_i^a - V_j^a)\cos\alpha\sin\alpha \tag{2.26}$$

for the off-diagonal terms where $W_{12}^d = W_{21}^d$. $V_{1,2}^a$ are the adiabatic potential energies and $W_{1,2}^d$ are the potential energies in the diabatic representation and W_{12}^d is the coupling between the two electronic states.

The general requirements when choosing the mixing angle, α, are that the surfaces are smooth [12] and that

$$\nabla\mathbf{S} + \mathbf{F}\mathbf{S} = 0 \tag{2.27}$$

where $\mathbf{S}$ is the transformation matrix and $\mathbf{F}$ is defined as the non-adiabatic coupling vector

$$\begin{aligned} \mathbf{F}_{ij} &= \langle\Phi_i^a|\frac{\partial}{\partial R}\Phi_j^a\rangle \\ &= \frac{1}{E_i - E_j}\langle\Phi_i^a|\frac{\partial\hat{H}_{el}}{\partial R}\Phi_j^a\rangle. \end{aligned} \tag{2.28}$$

Thus $\mathbf{F}_{ij}$ is inversely dependent on the energy gap between the 2 states, so as the gap becomes smaller the coupling increases and of course it becomes infinite if the 2 states become degenerate.

It is useful at this point to summarise and clarify the terms adiabatic, non-adiabatic and diabatic. We refer to a reaction which proceeds via more than one electronic state as non-adiabatic and the nuclear kinetic energy terms which couple the states are termed the non-adiabatic coupling elements. When we choose to ignore these coupling terms we treat the states within the adiabatic representation. If these terms are large and coupling cannot be ignored then we work within the diabatic representation where the coupling is contained within the potential functions.

2.6 The Vibronic Coupling Model Hamiltonian

For a system in which vibronic coupling becomes a necessary consideration a multi-state PES must be constructed. An analytical function can be fitted to *ab initio* data for this purpose and the parameters for the model Hamiltonian deduced from the fitting. The vibronic coupling Hamiltonian was first derived by Cederbaum *et al* [39] and has been used successfully to describe a number of systems in which non-adiabatic effects are important. Examples include butatriene [40], allene [41] and benzene [42]. The vibronic coupling model Hamiltonian is written as the sum of the diabatic potential operator matrices

$$\mathbf{H} = \mathbf{H}^{(0)} + \mathbf{W}^{(0)} + \mathbf{W}^{(1)} + \mathbf{W}^{(2)} + \dots \tag{2.29}$$

where $\mathbf{H}^{(0)}$ is the ground state Hamiltonian containing the KE operator and the potential terms. The matrices $\mathbf{W}^{n}$ contain terms that fit the model potentials to the excited electronic states. Before excitation the molecule is assumed to be in its electronic and vibrational ground state and $\mathbf{H}^{(0)}$ is written in its harmonic approximation as

$$H^{0}(\mathbf{Q}) = \sum_{\alpha}^{f} \frac{\omega_\alpha}{2} \left(-\frac{\partial^2}{\partial Q_\alpha^2} + Q_\alpha^2 \right) \tag{2.30}$$

where the sum is over the nuclear coordinates, $\mathbf{Q}$, which are the ground state normal modes (mass-frequency scaled) and f denotes the number of DOF. The diabatic operator matrices, $\mathbf{W}$, are expanded around the equilibrium point of the ground state and contain matrix elements

$$\begin{aligned} W_{ij}^{(0)} &= \langle \Phi_i(\mathbf{Q_0}) | H_{el} | \Phi_j(\mathbf{Q_0}) \rangle \\ W_{ii}^{(1)} &= \sum_{\alpha} \kappa_{\alpha}^{i} Q_{\alpha} \\ W_{ij}^{(1)} &= \sum_{\alpha} \lambda_{\alpha}^{ij} Q_{\alpha} \\ W_{ii}^{(2)} &= \sum_{\alpha\beta} \gamma_{\alpha\beta}^{i} Q_{\alpha} Q_{\beta} \end{aligned} \tag{2.31}$$

where Φ_i are the diabatic electronic functions. The on-diagonal coefficients $\kappa_{\alpha}^{(i)}$ are related to the derivative of the adiabatic potential and the off-diagonal coefficients $\lambda_{\alpha}^{(ij)}$ is the non-adiabatic coupling between the states

$$\begin{aligned} \kappa_{\alpha}^{(i)} &= \langle \Phi_{(i)} | \frac{\partial H}{\partial Q_{\alpha}} | \Phi_{(i)} \rangle \\ \lambda_{\alpha}^{(ij)} &= \langle \Phi_{(i)} | \frac{\partial H}{\partial Q_{\alpha}} | \Phi_{(j)} \rangle \end{aligned} \tag{2.32}$$

where $\Phi_{(i)}$ and $\Phi_{(j)}$ are the excited electronic states and the derivatives evaluated at $\mathbf{Q}_0$. $\gamma_{\alpha\beta}^{(i)}$ and $\mu_{\alpha\beta}^{(ij)}$ are the second derivatives in the adiabatic representation at $\mathbf{Q}_0$

$$\begin{aligned} \gamma_{\alpha\beta}^{(i)} &= \langle \Phi_{(i)} | \frac{\partial^2 H_{el}}{\partial Q_{\alpha} \partial Q_{\beta}} | \Phi_{(i)} \rangle \\ \mu_{\alpha\beta}^{(ij)} &= \langle \Phi_i | \frac{\partial^2 H_{el}}{\partial Q_{\alpha} Q_{\beta}} | \Phi_j \rangle . \end{aligned} \tag{2.33}$$

Assuming there are only 2 interacting electronic states and including only terms up to second order, the expansion takes the form

$$\begin{aligned} H = {} & T_n \mathbf{1} + \sum_{\alpha=1}^{f} \frac{\omega_{\alpha}}{2} Q_{\alpha}^2 \mathbf{1} + \begin{pmatrix} E_1 & 0 \\ 0 & E_2 \end{pmatrix} \\ & + \sum_{\alpha \epsilon G_1} \begin{pmatrix} \kappa_{\alpha}^{(1)} & 0 \\ 0 & \kappa_{\alpha}^{(2)} \end{pmatrix} Q_{\alpha} \\ & + \sum_{(\alpha,\beta) \epsilon G_2} \begin{pmatrix} \gamma_{\alpha,\beta}^{(1)} & 0 \\ 0 & \gamma_{\alpha,\beta}^{(2)} \end{pmatrix} Q_{\alpha} Q_{\beta} \end{aligned}$$

$$
\begin{aligned}
&+\sum_{\alpha\epsilon G_3}\begin{pmatrix} 0 & \lambda_\alpha \\ \lambda_i & 0 \end{pmatrix} Q_\alpha \\
&+\sum_{(\alpha,\beta)\epsilon G_4}\begin{pmatrix} 0 & \mu_{\alpha,\beta} \\ \mu_{\alpha,\beta} & 0 \end{pmatrix} Q_\alpha Q_\beta
\end{aligned}
\tag{2.34}
$$

The first two terms are the ground state Hamiltonian and the two energies, E_1 and E_2 are the vertical excitation energies (VEE). The next four terms describe the linear and bilinear coupling. Many of these expansion coefficients are zero by symmetry. An integral is only non-zero if the integrand is totally symmetric. For this to be non-zero the product of the irreducible representations must contain the totally symmetric representation, Γ_A:

$$\Gamma_\alpha \times \Gamma_{Q_i} \times \Gamma_\beta \supset \Gamma_A. \tag{2.35}$$

where Γ_α and Γ_β are the symmetries of the electronic states and Γ_{Q_i} the symmetry of the coordinate. For κ, $\alpha = \beta$ and the integral is zero unless Q_i is a totally symmetric mode.

$$\Gamma_\alpha \times \Gamma_{Q_i} \times \Gamma_\alpha \supset \Gamma_A. \tag{2.36}$$

The off-diagonal coefficients depend on the symmetries of the states. Thus the sums run over sets of modes, G_1 is the set of totally symmetric modes and G_3 the set of asymmetric modes which provide linear coupling between the two states. G_2 and G_4 provide the interstate and intrastate coupling respectively with G_2 being the pairs of modes whose product is totally symmetric.

$$
\begin{aligned}
G_1 &: \Gamma_i \supset \Gamma_A \\
G_2 &: \Gamma_i \times \Gamma_j \supset \Gamma_A \\
G_3 &: \Gamma_i \supset \Gamma_\alpha \times \Gamma_\beta \\
G_4 &: \Gamma_i \times \Gamma_j \supset \Gamma_\alpha \times \Gamma_\beta.
\end{aligned}
\tag{2.37}
$$

When only the linear coupling terms are included i.e. when γ and μ are set to zero, the result is the linear vibronic coupling (LVC) model. Extensions can be made by adding higher order terms for polyatomic systems where several normal modes need to be included.

Chapter 3

Methodology

3.1 Introduction

The PES are generated by solving the electronic Schrödinger equation at fixed nuclear geometries using *ab initio* electronic structure methods. The phrase *ab initio* means 'from the beginning' and in this context means that no experimental data is used and that all information is derived from theoretical calculations. The simplest method and invariably the starting point is Hartree Fock (HF) theory, a mean field method where the wavefunction is described by a single secular determinant. HF treats the electron-electron repulsion as an average and, therefore, neglects electron correlation. As a consequence it gives accurate results at equilibrium bond distances but fails in its description of the dissociating molecule.

More advanced methods are required to describe the photodissociation process and the ones used in this study are CASSCF, CASPT2, MS-MR-CASPT2 and MRCI. CASSCF is a self consistent field (SCF) method where a particular set of orbitals and electrons are selected from which to create many electron configurations. This method uses several secular determinants to describe the wavefunction and accounts for dynamic correlation within the active space but not outside of it. CASPT2 is a perturbation theory to second order which takes into account all the dynamic correlation using a single CASSCF reference state. The MS-MR-CASPT2 method has also been used in this study and is better suited than CASPT2 for calculating excited states which are close in energy. The configuration interaction method uses a linear combination of configuration state functions (CSF). If the expansion were to include all possible CSF this would be a full configuration interaction which solves exactly the electronic Schrödinger equation. The MRCI method used in this study uses more than one reference determinant and is a much better suited method for calculating excited states.

To calculate the time evolution of a system it is necessary to solve the time dependent Schrödinger equation and propagate the nuclear wavepacket over the PES. All wavepacket dynamics in this study were carried out using the multiconfiguration time-dependent hartree (MCTDH) method [43]. This method has been shown to be capable of treating much larger systems than other wavepacket propagation methods.

After the surfaces have been generated and the dynamics carried out on them, the results must be analysed and translated into some meaningful form. For photodissociation reactions the absorption spectrum is often the most vital piece of information. From the time evolution of a wavepacket an autocorrelation function [44] can be generated. The autocorrelation function is a measure of the overlap of the wavepacket at some later time with itself at time $t = 0$. A Fourier transform of the autocorrelation function from the time domain to the frequency domain [45] yields the absorption spectrum.

3.2 Electronic Structure Theory

3.2.1 Basis Sets

When *ab initio* methods are used to solve the Schrödinger equation the molecular orbitals are expressed as a linear combination of atomic orbitals

$$\phi_i = \sum c_{i\alpha}\chi_\alpha. \tag{3.1}$$

The molecular orbitals are unknown functions but may be expanded in a set of known functions, a basis set. The accuracy of a finite basis set depends not only on the size of the basis but also on the ability of the basis function to represent the unknown function. Two types of functions are commonly used in *ab initio* methods, Slater Type Orbitals (STO) and Gaussian Type Orbitals (GTO).

STO take the form

$$\chi_{\zeta,n,l,m}(r,\theta,\varphi) = NY_{l,m}(\theta,\varphi)r^{n-1}e^{-\zeta r} \tag{3.2}$$

where N is a normalisation constant, ζ is the orbital exponent related to the effective charge of the nucleus, r is the distance of the electron from the atomic nucleus and $Y_{l,m}$ are spherical harmonic functions. The spherical harmonic part of the function is what determines whether the orbital is a s, p, d, f, etc function and the radial part is represented by a polynomial in r multiplied by the exponential in r. The only way that a radial node can be expressed is by having a linear combination of STO.

The GTO can be written in terms of polar or cartesian coordinates and take the form

$$\begin{aligned} \chi_{\zeta,n,l,m}(r,\theta,\varphi) &= NY_{l,m}(\theta,\varphi)r^{(2n-2-l)}e^{-\zeta r^2} \\ \chi_{\zeta,l_x,l_y,l_z}(x,y,z) &= Nx^{l_x}, y^{l_y}, z^{l_z}e^{-\zeta r^2} \end{aligned} \tag{3.3}$$

where the sum of l_x, l_y and l_z determines the type of orbital.

After having chosen which type of function is to be used the next factor to consider is the number of functions. A minimal basis set represents the smallest number of functions that could be used to contain all of the electrons of a neutral atom.

In this study the Pople style 6-31G* basis set has been used. This is known as a split-valence double-zeta basis set where the core orbital is a *contracted* GTO (CGTO) made up of 6 Gaussians and the valence is described by two orbitals, one CGTO made of 3 Gaussians, and one single Gaussian. The CGTO's are the result of combining the full set of functions into a smaller set by forming fixed linear combinations. The justification for this comes when we realise that although the core orbitals in an atom are energetically important they do not play a crucial part in bonding and as they do not change significantly with respect to the bonding neither do the MO expansion coefficients in front of these functions and they can therefore be grouped together and treated as one function. The * in the 6-31G* is a polarisation function. This involves adding a higher angular momentum term to improve the description of a bond between two atoms. For example the bond between two H atoms which involves the s-orbitals can be better described by having a p-orbital added which serves to distort the s-orbitals. Likewise d-orbitals can be used to polarise p-orbitals, f-orbitals for d-orbitals etc. In methods such as CASPT2 where dynamic electron correlation is accounted for it is essential to use higher angular momentum functions. Dynamic correlation is a close range effect and is the energy lowering obtained by electrons avoiding one another. For example when two electrons are on opposite sides of the nucleus the basis set needs functions with different angular momenta. So to describe the angular correction of an s-function one would need p-, d-, f-functions etc. The dynamic correlation energy in a method such as CASPT2 converges more slowly with respect to basis sets than the HF method.

In this study we have also used double-zeta, LANLDZ, and triple-zeta, Dunning TZ, basis sets. This simply refers to the number of basis functions that are used for each atomic orbital. This introduces a higher level of accuracy but is also more computationally expensive.

3.2.2 Hartree Fock Theory

HF is one of the techniques used to solve the electronic Schrödinger equation and is often the starting point for many *ab initio* studies. The basis of this method is that the motion of each electron can be described by a single particle function, an orbital, and that electron-electron repulsion is treated in an average way. The assumption is made that each electron moves in an average potential which is due to all the other electrons and the nuclei. Using the clamped nucleus Hamiltonian, section 2.3, we can write the electronic Schrödinger equation

$$[\hat{T}_e(\mathbf{r}) + \hat{V}_{en}(\mathbf{r},\mathbf{R}) + \hat{V}_{nn}(\mathbf{R}) + \hat{V}_{ee}(\mathbf{r})]\Psi(\mathbf{r},\mathbf{R}) = E_{el}(R)\Psi(\mathbf{r};\mathbf{R}) \tag{3.4}$$

where $\mathbf{r}$ and $\mathbf{R}$ are the electronic and nuclear coordinates respectively. For each fixed nuclear geometry there is a set of electronic wavefunctions which satisfy $\hat{H}_e\Psi_e = E_e\Psi_e$. The nuclear-nuclear repulsion is a constant at a given fixed nuclear geometry as it is not dependent on the electron coordinates. The electron-nuclear attraction and the KE of the electrons are a sum of terms, each depending on only one electron coordinate whereas the electron-electron repulsion depends on two coordinates

$$\begin{aligned}
\mathbf{T}_e &= -\sum_{i=1}^{N}\frac{1}{2}\nabla_i^2 \\
\mathbf{V}_{ne} &= -\sum_{i=1}^{N}\sum_{a}\frac{Z_a}{\mid \mathbf{R}_a - \mathbf{r}_i \mid} \\
\mathbf{V}_{ee} &= \sum_{i=1}^{N}\sum_{j\,i}^{N}\frac{1}{\mid \mathbf{r}_i - \mathbf{r}_j \mid} \\
\mathbf{V}_{nn} &= \sum_{a}\sum_{b\,a}\frac{Z_a}{Z_b}\mid \mathbf{R}_a - \mathbf{R}_b \mid
\end{aligned} \tag{3.5}$$

The one and two electron operators are written

$$\begin{aligned}
\mathbf{h}_i &= -\frac{1}{2}\nabla_i^2 - \sum_{a}\frac{Z_a}{|\mathbf{R}_a - \mathbf{r}_i|} \\
\mathbf{g}_{ij} &= \frac{1}{|\mathbf{r}_i - \mathbf{r}_j|} \\
\mathbf{H}_e &= \sum_{i=1}^{N}\mathbf{h}_i + \sum_{i=1}^{N}\sum_{j>i}^{N}\mathbf{g}_{ij} + V_{nn}
\end{aligned} \tag{3.6}$$

where $\mathbf{h}_i$ describes the motion of electron i and $\mathbf{g}_{ij}$ is the two electron operator for the electron-electron repulsion. If we ignore this coupling, $\mathbf{g}_{ij}$, then the Hamiltonian is a sum of one electron terms

$$h_i\varphi_i = \epsilon_i\varphi_i \tag{3.7}$$

where ϵ_i is the energy of electron i. To solve, a product of one-electron wavefunctions is used and is known as a Hartree product

$$\Psi_e = \varphi_1^{(1)} \varphi_2^{(2)} ..... \tag{3.8}$$

This does not take into account the spin of the electrons or the Pauli exclusion principle for fermions which states that the wavefunction must be anti symmetric with respect to exchange of any two electron coordinates. These requirements are satisfied by writing the total wavefunction as a Slater determinant and expressing the one electron wavefunctions as spin orbitals, $\phi_a(i)$. For N electrons and N spin orbitals the determinant takes the form

$$\Phi = \frac{1}{\sqrt{N!}} \begin{vmatrix} \phi_1(1) & \phi_2(1) & \cdots & \phi_N(1) \\ \phi_1(2) & \phi_2(2) & \cdots & \phi_N(2) \\ \cdots & \cdots & \cdots & \cdots \\ \phi_1(N) & \phi_2(N) & \cdots & \phi_N(N) \end{vmatrix}, \quad \langle \phi_i | \phi_j \rangle = \delta_{ij} \tag{3.9}$$

which can be written as a sum of permutations over the diagonal of the determinant

$$\Phi = |\phi_1(1)\phi_2(2) \cdots \phi_N(N)\rangle. \tag{3.10}$$

The one electron functions are a product of a spatial orbital and a spin function, α or β and are orthonormal.

Now the Schrödinger equation is solved for Φ using the variational principle with Ψ as a trial wavefunction. Another approximation made in this method is that the trial wavefunction is made up of a single determinant resulting in a neglect of electron correlation treating the electron-electron repulsion as an average. From this single determinant the variational principle is used to derive the HF equations. The variational principle states that any trial wavefunction will have an energy higher than that of the true energy. The condition imposed on the orbitals when they are optimised is that they reduce the energy of the determinant.

From the two electron operator two terms are obtained, one is the coulomb integral, $\mathbf{J}_{ij}$, which describes the coulombic repulsion between electrons i and j and the other the exchange integral, $\mathbf{K}_{ij}$

$$\mathbf{J_j}\phi_\mathbf{i}(\mathbf{1}) = \left(\int \phi_\mathbf{j}^*(\mathbf{2})\frac{\mathbf{1}}{\mathbf{r_{ij}}}\phi_\mathbf{j}(\mathbf{2})\mathbf{d}\tau_\mathbf{2}\right)\phi_\mathbf{i}(\mathbf{1}) \tag{3.11}$$

$$\mathbf{K_j}\phi_\mathbf{i}(\mathbf{1}) = \left(\int \phi_\mathbf{j}^*(\mathbf{2})\frac{\mathbf{1}}{\mathbf{r_{ij}}}\phi_\mathbf{i}(\mathbf{2})\mathbf{d}\tau_\mathbf{2}\right)\phi_\mathbf{j}(\mathbf{1}). \tag{3.12}$$

We can now introduce the Fock operator, a one-electron operator which describes the KE of an electron, which is written

$$\mathbf{F_i} = \mathbf{h_i} + \sum_\mathbf{j}^\mathbf{N}(\mathbf{J_j} - \mathbf{K_j}) \tag{3.13}$$

and now the HF equations are

$$\mathbf{F_i}\phi_\mathbf{i} = \varepsilon_\mathbf{i}\phi_\mathbf{i}. \tag{3.14}$$

Introducing a basis set and denoting the atomic orbital basis functions as χ we can write the expansion

$$\phi_i = \sum_\alpha^M c_{\alpha i}\chi_\alpha \tag{3.15}$$

where χ is a sum of functions, generally Gaussian functions, representing the atomic orbitals and c are the coefficients which are calculated by the SCF method. The origin of the SCF method is that an initial guess is taken for the coefficients in equation 3.15 and the secular equations are solved using this initial guess to give new values for $c_{\alpha i}$. The secular equations being the solutions to the determinant which give the energies of the molecular orbitals in the molecule. These new values will then be used to solve the secular equations again until the new values obtained are identical to the previous ones. This is then a 'self-consistent' result. A basis with M members results in $2M$ different spin orbitals and by ordering the orbitals in terms of their energy and placing n electrons in the n lowest orbitals the HF wavefunction Φ_0 is created. The HF equations, 3.14, can then be written

$$\mathbf{F_i}\sum_\alpha^\mathbf{M}\mathbf{c}_{\alpha\mathbf{i}}\chi_\alpha = \varepsilon_\mathbf{i}\sum_\alpha^\mathbf{M}\mathbf{c}_{\alpha\mathbf{i}}\chi_\alpha \tag{3.16}$$

The SCF approach is then used to solve these equations. Multiplying equation 3.16 from the left by a specific basis function and integrating gives the Roothan Hall equations [46] in matrix form

$$\mathbf{FC} = \mathbf{SC}\varepsilon \tag{3.17}$$

where ε is a diagonal matrix of the orbital energies.

3.2.3 Electron Correlation Methods

The HF method treats electron-electron repulsion as an average by selecting only a single determinant for the trial wavefunction. The difference between the HF energy and the exact solution of the nonrelativistic Schrödinger equation is termed the *Electron Correlation* energy. There are two types of correlation energy, dynamic and static. Dynamic correlation is a short range effect due to the interaction of the electrons and becomes important when electrons approach one another. The description of dynamic correlation is improved upon by increasing the number of configurations used in the calculation to allow for near degeneracy effects. Static correlation, a long range effect, is when a single electronic configuration is not sufficient to describe the character of a wavefunction. It becomes important when a molecule dissociates. HF theory gives equal probability to a diatomic molecule splitting homolytically or heterolitically and a breakdown in the theory becomes apparent at large internuclear distances with dissociation energies often being substantially over estimated.

In order to create an improved method it is necessary to have a trial wavefunction which consists of more than one determinant

$$\Psi = a_0\Phi_{HF} + \sum_{i=1} a_i\Phi_i. \tag{3.18}$$

The determinants are classified according to the number of electrons which are promoted to virtual orbitals with reference to Φ_0. A symmetry adapted linear combination of these determinants is termed a CSF. Methods which use a linear combination of determinants for the trial wavefunction are configuration interaction methods. At the extreme, a full configuration interaction calculation would be a method which uses all available CSF but which would produce the best result possible for a given basis. However, full configuration interaction is computationally unmanageable for all but the smallest of systems so truncated methods such as CASSCF are implemented.

3.2.4 Complete Active Space Self Consistent Field (CASSCF)

In the CASSCF [47] method a linear combination of determinants is used. In this method not only are the coefficients for the determinants optimised but also the molecular orbitals which are used to generate them. The optimisation is an iterative procedure. By using more than one determinant to describe the wavefunction the energy of the system is lowered by accounting for the static correlation within the system. This is achieved by allowing the orbitals to become traditionally occupied and, therefore, producing a more flexible wavefunction with a much improved description of dissociation over the HF wavefunction. The dynamic correlation can be improved upon by increasing the number of electronic configurations but the dynamic correlation accounted for in CASSCF is all within the active space and is not accounted for in the inactive space or between the active and inactive electrons. In the CASSCF method a set of orbitals is chosen as an active space to perform configuration interaction upon with all other orbitals in the molecule termed as inactive. The inactive orbitals have a fixed occupancy of either 0 or 2 electrons throughout the calculation whilst the remaining electrons are distributed within the active orbitals in every possible way to produce the CSF and the wavefunction is written as a linear combination of all the CSF. The active orbitals are usually a set of some of the highest occupied and lowest unoccupied orbitals calculated by HF as a starting point to CASSCF. In depth knowledge of the system being studied is vital for choosing which orbitals to include in the active space. Careful consideration must be given to the particular process under scrutiny, to which electronic states may be involved and hence which orbitals will play a role in the reaction. Computational considerations will also place a restriction on the number of orbitals that can be included in the active space. The number of singlet CSF for N electrons and M basis functions is given by

$$CSF = \frac{M!(M+1)!}{(\frac{N}{2})!(\frac{N}{2}+1)!(M-\frac{N}{2})!(M-\frac{N}{2}+1)!} \tag{3.19}$$

so, for example a 10 electron 10 orbital active space would have 19 400 singlet CSF.

3.2.5 Multi-Reference Configuration Interaction (MRCI)

The configuration interaction [48] method uses a linear combination of determinants as a trial wavefunction. The expansion coefficients for the determinants are determined by requiring that the energy be a minimum. Determinants may be singly, doubly, triply etc. excited

$$\begin{aligned}\Psi_{CI} &= a_0\Phi_{SCF} + \sum_S a_S\Phi_S + \sum_D a_D\Phi_D + \sum_T a_T\Phi_T \\ &= \sum_{i=0} a_i\Phi_i. \end{aligned} \tag{3.20}$$

If all possible CSF are included in this expansion it is a full configuration interaction. The singly excited configurations do not introduce a significant level of electron correlation but rather it is the double excitations that are most important. The method may be truncated to reduce the number of determinants in the expansion. For example CISD is limited to single and double excitations only.

The configuration interaction method is based on the variational principle to account for electron correlation. By using variational parameters the weights for different terms in the wavefunction can be changed, for example the ionic terms for a dissociating diatomic molecule disappear at large internuclear separations. Unlike CASSCF the molecular orbital coefficients are not reoptimised in this method.

The configuration interaction method leads to a matrix eigenvalue equation

$$\mathbf{Hc} = \mathbf{eSc} \tag{3.21}$$

where **c** is a vector of coefficients, **e** is the eigenvalue matrix containing the energies of the states and the elements of the Hamiltonian and overlap matrices are

$$\begin{aligned} \mathbf{H}_{ij} &= \langle \Phi_i | \mathbf{H}_{el} | \Phi_j \rangle \\ \mathbf{S}_{ij} &= \langle \Phi_i | \Phi_j \rangle = \delta_{ij}. \end{aligned} \tag{3.22}$$

Exciting electrons out of a single determinant as in equation 3.20 corresponds to having a HF type wavefunction as reference. The MRCI method uses a CASSCF wavefunction as reference where electrons are excited out of all of the determinants. This gives a better correlation of the ground and excited states.

Using this method means that the calculations become more computationally demanding, the number of electronic configurations increases by a factor which is approximately equal to the number of configurations in the CASSCF.

3.2.6 Complete Active Space with Second-Order Perturbation Theory (CASPT2)

The superiority of the CASPT2 [49, 50] method over CASSCF is due to its ability to account for dynamic correlation and it is also computationally cheaper than MRCI. The CASSCF multi reference wavefunction is used as a starting point for the CASPT2 calculations and the perturbation, taken to second order, is implemented using orbital excitation operators which are applied to the reference wavefunction. The theory behind this method is based on the fact that the perturbation to the Hamiltonian is so small that it only differs slightly from a known solution. The Schrödinger equation for a known solution is written

$$\hat{H}_0 |\psi_n\rangle = E_n |\psi_n\rangle \tag{3.23}$$

where $\psi_n\rangle$ are the eigenstates with energies E_n. A small perturbation is added to the Hamiltonian

$$\hat{H} = \hat{H}_0 + \lambda \hat{H}' \tag{3.24}$$

where λ determines the strength of the perturbation and takes a value between 0 and 1. $\hat{H}_0$ is the sum of one electron Fock operators and $\hat{H}'$ is the difference between the full Hamiltonian and $\hat{H}_0$. The new equation which will then be solved is written

$$\hat{H}|\psi\rangle = E|\psi\rangle \tag{3.25}$$

where $\hat{H}$ is the perturbed Hamiltonian from equation 3.24 and $|\psi\rangle$ and E are the new perturbed wavefunction and energy. The aim is to see how the perturbed Hamiltonian changes the energy and the wavefunction and as both are dependent upon λ we can write them as a power series in terms of λ

$$\begin{aligned} E &= E_n + \lambda E^{[1]} + \lambda^2 E^{[2]} + \cdots && (3.26) \\ |\psi\rangle &= |\psi_n\rangle + \lambda|\phi_1\rangle + \lambda^2|\phi_2\rangle + \cdots && (3.27) \end{aligned}$$

where $|\psi_n\rangle$ and E_n are the known eigenfunction and energy without an added perturbation. Substituting equations 3.26 and 3.27 into equation 3.25 gives the following

$$\begin{aligned} (\hat{H}_0 + \lambda\hat{H}')(|\psi\rangle &+ \lambda|\phi_1\rangle + \lambda^2|\phi_2\rangle + \cdots) && (3.28) \\ = (E_n &+ \lambda E^{[1]} + \lambda^2 E^{[2]} + \cdots)(|\psi_n\rangle + \lambda|\phi_1\rangle + \lambda^2|\phi_2\rangle + \cdots) && (3.29) \end{aligned}$$

This equation can be applied to any value of λ so terms with the same power of λ can be collected to give

$$\lambda^0 \quad \hat{H}_n|\phi_n\rangle = E_n|\psi_n\rangle \tag{3.30}$$

$$\lambda^1 \quad \lambda\hat{H}'|\psi_n\rangle + \lambda\hat{H}_0|\phi_1\rangle = \lambda E_n|\phi_1\rangle + \lambda E^{[1]}|\psi_n\rangle \tag{3.31}$$

$$\lambda^2 \quad \lambda^2\hat{H}_0|\phi_2\rangle + \lambda^2\hat{H}'|\phi_1\rangle = \lambda^2 E^1|\phi_1\rangle + \lambda^2|\psi_n\rangle + \lambda^2 E_n|\phi_2\rangle \tag{3.32}$$

where equation 3.30 is the original unperturbed Schrödinger equation, however for equations 3.31 and 3.32 it must be ascertained how $|\phi_1\rangle$ and $|\phi_2\rangle$ change when operated on by $\hat{H}_0$. Because the solutions to the unperturbed Schrödinger equation generate a complete set of functions which form an orthonormal basis the unknown first order correction to the wavefunction can be expanded in these functions. This is the *Rayleigh-Schrödinger* perturbation theory

$$|\phi_1\rangle = c_1|\psi_1\rangle + c_2|\psi_2\rangle + \cdots + c_m|\psi_m\rangle + \cdots = \sum_i c_i|\psi_i\rangle \tag{3.33}$$

$$|\phi_2\rangle = \sum_i d_i|\psi_i\rangle. \tag{3.34}$$

Now when $\hat{H}_0$ is applied to equation 3.33 and 3.34 it gives the energy

$$\hat{H}_0|\phi_1\rangle = \hat{H}_0\left(\sum_i c_i|\psi_i\rangle\right) = \sum_i E_i c_i|\psi_i\rangle \tag{3.35}$$

and

$$\hat{H}_0|\phi_2\rangle = \sum_i E_i d_i|\psi_i\rangle. \tag{3.36}$$

Thus using equation 3.35 for the action of applying $\hat{H}_0$ to $|\phi_1\rangle$, equation 3.31 can be written

$$\lambda\hat{H}'|\psi_n\rangle + \lambda\sum_i E_i c_i|\psi_i\rangle = \lambda E_n\sum_i c_i|\psi\rangle + \lambda E^{[1]}|\psi_n\rangle. \tag{3.37}$$

This equation needs to be solved to find $E^{[1]}$. Multiplying from the left by the original eigenfunction, $\langle\psi_n|$, and integrating gives

$$\lambda\langle\psi_n|\hat{H}'|\psi_n\rangle + \lambda E_n c_n = \lambda E_n c_n + \lambda E^{[1]} \tag{3.38}$$

so

$$\lambda E^{[1]} = \langle\psi_n|\lambda\hat{H}'|\psi_n\rangle. \tag{3.39}$$

Starting from equation 3.32 analogous formulas can be generated for the second-order correction to the energy. So to find $\lambda^2E^{[2]}$ substitute equations 3.33 and 3.34 into equation 3.32 and when $\hat{H}_0$ operates on the sum of eigenvectors as in equation 3.36 it is written

$$\lambda^2\sum_i d_iE_i|\psi_i\rangle + \lambda^2\hat{H}'\sum_i c_i|\psi_i\rangle = \lambda^2E^{[1]}\sum_i c_i|\psi_i\rangle + \lambda^2E^{[2]}|\psi_n + \lambda^2E_n\sum_i d_i|\psi_i\rangle. \tag{3.40}$$

Then multiply from the left by $\langle\psi_n|$ and substitute $\langle\psi_n|\lambda\hat{H}'|\psi_n\rangle$ for $E^{[1]}$ and solve for $\lambda^2 E^{[2]}$

$$\lambda^2 E^{[2]} = \lambda^2 \sum_i c_i \langle\psi_n|\hat{H}'|\psi_i\rangle - \lambda^2 c_n \langle\psi_n|\hat{H}'|\psi_n\rangle \tag{3.41}$$

where the right hand side is the sum over all eigenfunctions ψ_i minus the eigenfunction ψ_n which can be written as

$$\lambda^2 E^{[2]} = \lambda^2 \sum_{i\neq n} c_i \langle\psi_n|\hat{H}'|\psi_i\rangle. \tag{3.42}$$

To find the coefficients, c_i, apply an eigenfunction, $\langle\psi_m|$ to both sides of equation 3.37, where $\langle\psi_m| \neq \langle\psi_n|$ and this gives

$$\lambda\langle\psi_m|\hat{H}'|\psi_n\rangle + \lambda E_m c_m - \lambda E_m c_m = 0 \tag{3.43}$$

and then

$$c_m = \frac{\langle\psi_m|\hat{H}'|\psi_n\rangle}{E_n - E_m}. \tag{3.44}$$

This expression can then be substituted for the coefficients in equation 3.42 to give $\lambda^2 E^{[2]}$

$$\begin{aligned} \lambda^2 E^{[2]} &= \sum_{i\neq n} \frac{\langle\psi_n|\lambda\hat{H}'|\psi_i\rangle\langle\psi_i|\lambda\hat{H}'|\psi_n\rangle}{E_n - E_i} \\ &= \sum_{i\neq n} \frac{|\langle\psi_n|\lambda\hat{H}'|\psi_i\rangle|^2}{E_n - E_i}. \end{aligned} \tag{3.45}$$

It is also possible to calculate the change in the wavefunction due to the perturbation. Referring back to equation 3.27 the lowest order change to $|\psi_n\rangle$ is given by $\lambda|\phi_1\rangle$ which is expressed as a sum over the unperturbed eigenfunctions in equation 3.33 and the coefficients, c_i which are given by equation 3.44. The coefficients can be substituted into equation 3.33 to give

$$\lambda|\phi_1\rangle = \sum_{i\neq n} \frac{\langle\psi_i|\lambda\hat{H}'|\psi_n\rangle}{E_n - E_i}|\psi_i\rangle \tag{3.46}$$

$$= \sum_{i\neq n} \frac{\langle\psi_i|\hat{H}'|\psi_n\rangle}{E_n - E_i}|\psi_i\rangle \tag{3.47}$$

The CASPT2 method has been applied to many different systems in molecular structure determination for ground and excited states [51] and calculations of binding energies in transition metal compounds [52, 53] as well as photochemistry where it has been found to yield accurate results. For example when the method was applied to the electronic spectrum of the nickel atom and the benzene excitation energies were computed with errors less than 0.2 eV.

The CASPT2 method uses a single CASSCF wavefunction as reference and as a result is inadequate in regions of avoided crossings. The MS-MR-CASPT2 method uses a multi-dimensional reference space spanned by two or more state average CASSCF states and a level shift can be applied to avoid intruder state problems [54].

3.3 Wavepacket Dynamics

3.3.1 Relaxing the Wavepacket

It is possible to obtain a ground state eigenfunction by propagating a wavepacket in imaginary time, ie. changing t to $i\tau$ and using the equation

$$H\Psi = -\frac{\partial\Psi}{\partial\tau}. \tag{3.48}$$

To see how this works if we write a wavepacket in terms of a set of eigenfunctions

$$\Psi(x,t) = \sum_i c_i\psi_i(x)e^{-i\frac{E}{\hbar}t} \tag{3.49}$$

then after this transformation

$$\Psi = \sum_i c_i\psi_i e^{-\frac{E}{\hbar}\tau}. \tag{3.50}$$

As time progresses, the eigenstates decay, with the lowest energy state ($E = 0$) being left [55].

3.3.2 Time-Dependency of a Wavepacket

From equation 3.49 we see that the wavepacket is time-dependent. This is only valid when ψ is written as a superposition of eigenfunctions

$$\Psi(x,t) = a\psi_E(x)e^{-i\frac{E}{\hbar}t} + b\psi_{E'}(x)e^{-i\frac{E'}{\hbar}t}. \qquad (3.51)$$

Then the probability density can be written

$$|\Psi(x,t)|^2 = |a|^2|\psi_E(x)|^2 + |b|^2|\psi_{E'}(x)|^2 + 2Re\left(a^*b\psi^*_E(x)\psi_{E'}(x)e^{-i\frac{(E'-E)t}{\hbar}}\right). \qquad (3.52)$$

The third term on the right is the interference term due to the superposition of the two states and it is this term which contains the time dependency.

3.3.3 Multiconfiguration Time-Dependent Hartree (MCTDH) Method

MCTDH [56, 57] is an algorithm for solving the time-dependent Schrödinger equation. The method is capable of treating multi-dimensional, non-adiabatic systems in which surfaces are strongly coupled. In standard propagation methods, in which the wavepacket and Hamiltonian are represented by a time-independent product basis, the calculation becomes computationally impossible as the number of DOF increases. The MCTDH method accounts for this by representing the wavefunction using a number of so called *single particle functions* (SPFs) which may be one- or multi-dimensional and are time-dependent.

In atomic units where $\hbar = 1$, the time-dependent Schrödinger equation is written

$$i\dot{\Psi} = \hat{H}\Psi. \qquad (3.53)$$

The MCTDH wavefunction ansatz to solve the time-dependent Schrödinger equation is written

$$\Psi(q_1, \cdots q_f, t) = \sum_{j_1=1}^{n_1} \cdots \sum_{j_f=1}^{n_f} A_{j_1 \cdots j_f}(t)\varphi^{(1)}_{j_1}(q_1,t)\cdots\varphi^{(f)}_{j_f}(q_f,t) \qquad (3.54)$$

where $q_1 \cdots q_f$ are the nuclear coordinates, $A_{j1 \cdots j_f}$ are the time-dependent expansion coefficients and $\varphi^{(1)}_{j_1} \cdots \varphi^{(f)}_{j_f}$ are the time-dependent SPFs for each DOF. Convergence for a dynamics calculation is achieved by increasing the number of SPFs until the property that is being studied no longer changes. In a photodissociation reaction, for example, an absorption spectrum that no longer changes would show that convergence had been reached.

Using a composite index for simplicity where $J = j_1 \cdots \mathrm{j}_f$ and $\Phi_J = \varphi_{j_1} \cdots \varphi_{j_f}$, we can write

$$i \sum_J \dot{A}_J |\Phi_J\rangle = \sum_J H A_J |\Phi_J\rangle. \tag{3.55}$$

Multiplying from the left by $\langle \Phi_L|$

$$i \sum_J \dot{A}_J \langle \Phi_L | \Phi_J \rangle = \sum_J A_J \langle \Phi_L | H | \Phi_J \rangle \tag{3.56}$$

where $\langle \Phi_L | \Phi_J \rangle = \delta_{LJ}$, gives a solution for A

$$\begin{aligned} i\dot{A}_J &= \sum_J A_J \Phi_J \\ &= \sum_L \langle \Phi_J | H | \Phi_L \rangle A_L. \end{aligned} \tag{3.57}$$

If Φ is time-independent then this is the full solution. For MCTDH Φ depends on time and a variational solution to the time-dependent Schrödinger equation is provided by a coupled set of equations for the expansion coefficients and for the SPFs

$$\begin{aligned} i\dot{\mathbf{A}} &= \mathcal{K}\mathbf{A} \\ i\dot{\varphi}^{(\kappa)} &= (1 - P^{(\kappa)})(\rho^{(\kappa)})^{-1}\mathcal{H}^{(\kappa)}\varphi^{(\kappa)} \end{aligned} \tag{3.58}$$

where $\mathcal{K}$ is the Hamiltonian operator

$$\mathcal{K}_{JL} = \langle \Phi_J | H | \Phi_L \rangle \tag{3.59}$$

and is time-dependent due to the SPFs and ρ is a density matrix defined as

$$\rho^{(\kappa)}_{ab} = \langle \Psi^{(\kappa)}_a | \Psi^{(\kappa)}_b \rangle. \tag{3.60}$$

$P^{(\kappa)}$ is the projector onto the space spanned by the SPFs

$$P^{(\kappa)} = \sum_j |\varphi_j^{(\kappa)}\rangle\langle\varphi_j^{(\kappa)}| \tag{3.61}$$

and the operator $(1 - P^{(\kappa)})$ ensures that the time derivative of the SPF is orthogonal to the space spanned by the functions.

The integrals of the form

$$\begin{aligned} \mathcal{K} &= \langle\Phi_J|T + V|\Phi_L\rangle \\ &= \langle\varphi_{j_1}^{(1)} \cdots \varphi_{j_f}^{(f)}|T + V|\varphi_{j_1}^{(1)} \cdots \varphi_{j_f}^{(f)}\rangle \end{aligned} \tag{3.62}$$

need to be solved in order to solve the equations of motion for the coefficients and for the SPFs, equation 3.58. The multi-dimensional integral can be conveniently evaluated if the SPFs are represented using a discrete variable representation (DVR) as a basis set. This means that the matrix elements of the potential energy operator, $V(x)$, are diagonal. The matrix elements of the KE operator can also be evaluated in the related finite basis representation (FBR).

3.3.4 Discrete Variable Representation (DVR)

The DVR [58] is a grid point representation which is used for representing wavefunctions and operators and in which the potential energy matrix is diagonal. DVR representation solves the problem of having to evaluate integrals. The idea of a DVR is to use a set of orthonormal functions that give an analytic solution for the momentum operator, and hence KE. This is the FBR. By diagonalising the position operator in the FBR a set of grid points and DVR functions are produced. Several DVR's have been used in this study and are described briefly in this section.

The Legendre DVR, based on the Legendre functions, is used for angular DOF because the Legendre functions are eigenfunctions of the angular momentum operator. The exponential and fast Fourier transform (FFT) DVR's share the property that they satisfy periodic boundary conditions which occur, for example, in torsional motion.

The exponential DVR uses plane waves as basis functions and is, therefore often used to describe dissociative DOF. The harmonic oscillator DVR uses harmonic oscillator functions as basis functions and is used for vibrational motion. The Sine DVR uses the particle-in-a-box eigenfunctions as basis. For a full review see [56].

3.3.5 Time autocorrelation functions

After the wavepacket dynamics have been carried out for a particular system then the analysis is the next step. One of the simplest observables which can be obtained is the absorption spectrum. Spectra computed from the time-dependent Schrödinger equation are done so from an autocorrelation function. A time autocorrelation function, $C(t)$, indicates how a physical variable, in this case a wavepacket, is correlated to its initial value. In the case of a wavepacket it is a representation of the overlap of the wavepacket at t with the initial wavepacket at $t = 0$

$$C(t) = \langle \psi(0) | \psi(t) \rangle. \tag{3.63}$$

The absorption spectrum, $\sigma(\omega)$, for a particular molecule is generated by Fourier transform of $C(t)$ to the frequency domain [45]

$$\sigma(\omega) \propto \omega \int_{-\infty}^{\infty} dt\; C(t) e^{i\omega t} \tag{3.64}$$

which for practical reasons can be written

$$\sigma(\omega) \propto \omega Re \int_{0}^{\infty} dt\; C(t) e^{i\omega t}. \tag{3.65}$$

3.3.6 Flux Analysis

When a molecule undergoes photodissociation on a set of coupled PES the reaction may proceed on more than one state. A measure of the amount of dissociation which occurs on a particular state compared with that of a second state is termed a branching ratio. The branching ratio for a reaction is determined by calculating the quantum flux, or the amount of the wavepacket, going into a particular channel. This is done by placing a complex absorbing potential (CAP) on the channel of interest and then measuring the amount of the wavepacket that interacts with the CAP [59]. CAPs are usually used in wavepacket dynamics to absorb parts of the wavepacket that reach the end of the grid and hence to prevent reflection of the wavepacket [60, 61]. The CAPs used in MCTDH take the form

$$-iW(Q) = -i\eta(Q - Q_c)^n \Theta(Q - Q_c) \tag{3.66}$$

where Θ is a function whose value changes abruptly from 0 to 1, a step function, Q_c is the starting point for the CAP, η is the CAP strength and n an integer. For a photodissociation reaction a CAP can be placed on the dissociative channel to measure the amount of dissociating wavepacket. For reactions in which there is more than one exit channel, the flux may be calculated for individual electronic states. In the case of ammonia the reaction proceeds via a CI and dissociation takes place on the ground and first excited state so by measuring the quantum flux for each state independently, a branching ratio can be calculated. The Hamiltonian for the system can be written

$$H = H_0^\gamma + V_I^\gamma \tag{3.67}$$

where V_I^γ is the potential for the dissociation channel, γ, and H_0^γ is the free Hamiltonian which can be separated into two parts, a KE part for the relative motion of the dissociating part of the molecule with the remaining part, and the internal Hamiltonian which operates on all internal DOF

$$H_0^\gamma = T_R^\gamma + H_{int}^\gamma \tag{3.68}$$

where

$$T_R^\gamma = -\frac{1}{2m}\frac{\partial^2}{\partial R^2}. \tag{3.69}$$

The flux which passes into the dissociation channel, γ, can be described as the change in population of this channel with respect to time and can be written

$$\frac{d}{dt}\langle\Psi|\Theta_\gamma|\Psi\rangle = i\langle\Psi|[H, \Theta_\gamma]|\Psi\rangle \tag{3.70}$$

where Θ is a function equal to 1 in the asymptotic region and zero everywhere else. It follows on from here that the flux operator can then be written as

$$\hat{F}_\gamma = i[H, \Theta_\gamma]. \tag{3.71}$$

Using a step function which is equal to one for all positive values and zero otherwise, Θ_γ can be written

$$\Theta_\gamma = \theta(R_\gamma - R_{\gamma c}). \tag{3.72}$$

When a CAP is used it is added to the Hamiltonian

$$\tilde{H} = H - iW, \tag{3.73}$$

focusing on one channel and dropping the subscript γ

$$\begin{aligned} \hat{F} &= i[H - iW, \Theta] \\ &= iH\Theta + W\Theta - i\Theta H + \Theta W \\ &= iH\Theta + 2W - i\Theta H \\ &= i[H, \Theta] + 2W. \end{aligned} \tag{3.74}$$

To calculate the total flux into the channel we need to evaluate the integral

$$\int_0^T dt\langle\Psi(t)|F|\Psi(t)\rangle = dt\langle\Psi|\Theta|\Psi\rangle + \int_0^T 2\langle\Psi|W|\Psi\rangle dt. \tag{3.75}$$

The first term on the right is equal to zero at the initial and final values for t, at T the wavepacket has been absorbed by the CAP, so then the total flux is calculated from

$$2\int\langle\Psi|W|\Psi\rangle dt. \tag{3.76}$$

Chapter 4

Full-Dimensional Coupled Surface Photodissociation Study of NH_3

4.1 Literature Review

The photodissociation of ammonia has been the subject of many studies both theoretical and experimental [62–65]. It is well known that the ground state has a double minimum in the inversion or umbrella mode where the minima are equivalent pyramidal, C_{3v}, structures. The first singlet excited state has a single minimum at the D_{3h} planar geometry where a conical intersection exists between the 2 states. On promotion to the first excited state, $NH_3(\tilde{A}\,^1A_2'')$, there are two possible routes to dissociation: non-adiabatically via the CI in the ground electronic state to form $NH_2(\tilde{X}\,^2B_1) + H$, and adiabatically in the first excited state to form $NH_2(\tilde{A}\,^2A_1) + H$.

The competition between these two routes has been the subject of some experimental work by Crim *et al* [66]. Using velocity map imaging (VMI) the paths to dissociation were studied for different vibrations in the excited state. They found that molecules with an excited symmetric N-H stretch (ν_1) dissociated to produce ground state NH_2 and that the antisymmetric N-H stretch (ν_3) resulted in production of NH_2 in the excited $\tilde{A}\,^2A_1$ state. They concluded that the antisymmetric stretching mode caused the photodissociation to avoid the CI. The most recent work, carried out by Stavros *et al* [67] is an experimental study looking at how the timescale to dissociation is dependent on the internal energy of the NH_2 fragment. By using pump/probe spectroscopy and VMI they were able to study the dissociation in real time following the excitation of the umbrella mode and investigate the different pathways on which the process occurs. They found that the different final states of the NH_2 correlated with different dissociation lifetimes of the NH bond. They did not however produce any branching ratios for the competition between the two states.

Further investigation of the dissociation on these two surfaces is the subject of this study and after carrying out wavepacket dynamics on the coupled PES we will carry out a flux analysis for the ground and excited states and produce a branching ratio for the reaction.

The experimental absorption spectrum, figure 4.1, is dominated by one main progression attributed to the ν_2 umbrella mode [68] with a frequency of 968.3 and 878 cm^{-1} for the ground and excited state respectively [69].

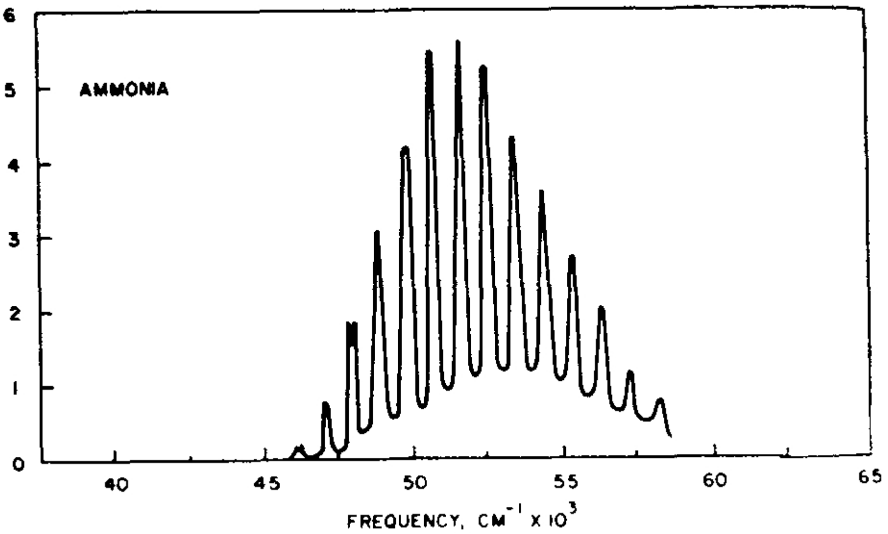

Fig. 4.1: Experimental absorption spectrum for NH_3 taken from Tannenbaum *et al* [68].

A theoretical investigation was carried out by Tannor *et al* [70] using a model which was tailored to reproduce the absorption spectrum. The spectrum was calculated using time-dependent methods and by placing a wavepacket in each of the two lowest vibrational eigenstates they were successful in reproducing the single progression in the umbrella mode.

The most recent work by Guo *et al* [71] was a full-dimensional quantum dynamics study where they investigated the dissociation dynamics of NH_3 and ND_3. Their study involved carrying out wavepacket dynamics specifically in the well of the excited state, ignoring the S_0/S_1 CI that is crucial for the photodissociation. Again they calculated a spectrum from the two lowest vibrational eigenstates and managed to reproduce many of the features from the experimental spectrum.

The diabatic PES with coupling have been calculated by Truhlar *et al* [72, 73] using multi-configuration quasi-degenerate perturbation theory (MC-QDPT) with a state-averaged CASSCF reference function over 3600 reference geometries of NH_3. The active space contained 8 electrons in 7 orbitals. This included 3 bonding N-H molecular orbitals and one non-bonding orbital centered on the N atom and 3 virtual orbitals to include the 2 antibonding N-H orbitals and 1 Rydberg-type orbital with 3s character centered on the N atom. They used a 6-311++G(3df,3pd) basis set with 6 sets of 6 Cartesian d functions (3 on N, 1 on each H) and 1 set of 10 Cartesian f functions (on N). They produced the adiabatic and diabatic surfaces for the ground and first excited states and the coupling between them and it is these surfaces which will be used in this study.

Two models which contrast greatly in their complexity are used for this investigation. We first use a 2D model which provides a description of the umbrella mode of NH_3 with the motion of just one proton relative to the fixed NH_2 group, and then a 6D model which surpasses any previous work of this nature carried out on NH_3 in its description of the photodissociation of the entire molecule. The two models make for an interesting comparisons in terms of their effect on the dynamics and the branching ratios.

4.2 The Kinetic Energy Operator

Firstly we must choose the coordinates for the KE operator. Binding coordinates are representative of the bond lengths and the bending mode of the molecule but the KE operator written in these coordinates is complicated. We therefore use Jacobi coordinates to represent the molecule where the KE operator is of a simpler form.

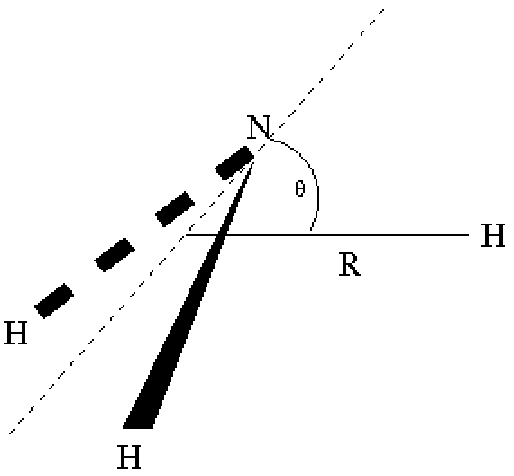

Fig. 4.2: 2D NH_3 model with DOF R and θ defining the umbrella mode by the motion of one proton relative to a fixed NH_2 group.

4.2.1 The 2 Dimensional Model

The 2D model in Jacobi coordinates is shown in figure 4.2. The molecule is expressed in terms of the dissociating H atom where R is the distance between H and the centre of mass (COM) of the NH_2, and θ which is the angle that R makes with the plane of the NH_2. When $\theta = 0$ then the molecule adopts the planar D_{3h} geometry. The H-N-H angle of the NH_2 group is held at 120°. The molecule is thus treated as a pseudotriatomic. A triatomic molecule which undergoes dissociation of one of its atoms can be best described in terms of Jacobi coordinates, R, r and θ.

The full KE operator for this system is written [74]

$$\begin{aligned} H = & - \frac{1}{2\mu_R}\frac{\partial^2}{\partial R^2} - \frac{1}{2\mu_r}\frac{\partial^2}{\partial r^2} + \frac{\hat{j}^2}{2\mu_r r^2} \\ & + \frac{1}{2\mu_R R^2}[J(J+1) - 2K^2 + \hat{j}^2] \end{aligned} \tag{4.1}$$

where μ refers to the reduced masses

$$\mu_r = \frac{m_A m_B}{m_A + m_B} \tag{4.2}$$

$$\mu_R = \frac{m_C(m_A + m_B)}{m_A + m_B + m_C} \tag{4.3}$$

and $\hat{j}$ is the angular momentum operator, which in spherical coordinates can be written

$$\hat{j}^2 = -\left(\frac{1}{\sin\theta}\frac{\partial}{\partial\theta}\sin\theta\frac{\partial}{\partial\theta} - \frac{K^2}{\sin^2\theta}\right). \tag{4.4}$$

J is the total angular momentum and K is the projection of J onto R. In this study we take $J = 0$. This means that the terms with J and K in equation 4.1 will drop out.

For our 2D NH_3 system r is a constant and we can rewrite the KE operator in terms of R and θ as

$$H(R,\theta) = -\frac{1}{2\mu_R}\frac{\partial^2}{\partial R^2} - \frac{1}{2I}\left(\frac{1}{\sin\theta}\frac{\partial}{\partial\theta}\sin\theta\frac{\partial}{\partial\theta}\right) \tag{4.5}$$

where $\mathrm{I}^{-1} = (\mu R^2)^{-1} + (mr^2)^{-1}$, $\mu = M_H M_{NH_2}/M_{NH_3}$, $m = 2M_H M_N/M_{NH_2}$ and $r = 1.9199616 \cos(\pi/3)$ bohr which is the fixed distance between the N atom and the COM of the two H atoms.

4.2.2 The 6 Dimensional Model

The 6D model [75], figure 4.3, has an N-H bond length, r_2, defining the bond between N and H_1. From the COM of r_2 comes r_1 defining the position of H_3 and with an in plane angle, θ, which defines the angle between r_1 and r_2. The dissociative H atom is defined relative to the COM of r_1 with length R and with two angles, γ and ϕ, where γ is the in plane angle and ϕ the out of plane and is equivalent to the angle θ of the 2D model.

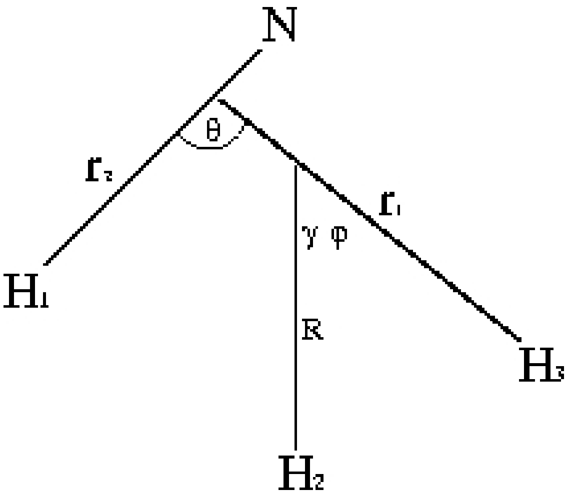

Fig. 4.3: 6D NH_3 model with DOF r_1, r_2, R, θ, γ and ϕ.

We now look at the 6D NH_3 and the KE operator which is used for this system. From Meyer *et al* [76] the KE operator for a tetra-atomic molecule can be written using Jacobi coordinates as

$$\begin{aligned}
2\hat{T} &= \sum_{i=1}^{3}\left(-\frac{1}{\mu_i}\frac{\partial^2}{\partial R_i^2}\right) - \left(\frac{1}{\mu_1 R_1^2}+\frac{1}{\mu_3 R_3^2}\right) j_1^2 \\
&- \left(\frac{1}{\mu_2 R_2^2}+\frac{1}{\mu_3 R_3^2}\right) j_2^2 + \frac{1}{\mu_3 R_3^2}\left[j_{iz}^2 + j_{1+}\times j_{2-} + j_{1-}j_{2+}\right] \\
&+ \frac{1}{\mu_3 R_3^2}\left[J(J+1) + 2\frac{\partial}{\partial\varphi_2}\left(\frac{\partial}{\partial\varphi_2}+\frac{\partial}{\partial\varphi_1}\right)\right] \\
&- \frac{C_+(J,K)}{\mu_3 R_3^2}\left[j_{1+}+j_{2+}\right] - \frac{C_-(J,K)}{\mu_3 R_3^2}\left[j_{1-}+j_{2-}\right] \qquad (4.6)
\end{aligned}$$

where the angular momentum operators for the spherical angles associated with the COM of r_1 and r_2 are

$$\begin{aligned}
j_i^2 &= \left[\frac{1}{\sin\theta_i}\frac{\partial}{\partial\theta_i}\sin\theta_i\frac{\partial}{\partial\theta_i}+\frac{1}{\sin^2\theta_i}\frac{\partial^2}{\partial\varphi_i}\right] \\
j_{iz}^2 &= 2\frac{\partial^2}{\partial\varphi_i}
\end{aligned}$$

$$
\begin{aligned}
j_{1+} &= e^{i\varphi_1}\left(\frac{\partial}{\partial\theta_1} + i\cot\theta_1\frac{\partial}{\partial\varphi_1}\right)\\
j_{2-} &= e^{i\varphi_2}\left(-\frac{\partial}{\partial\theta_2} + i\cot\theta_2\frac{\partial}{\partial\varphi_2}\right)\\
j_{1-} &= e^{-i\varphi_1}\left(-\frac{\partial}{\partial\theta_1} + i\cot\theta_1\frac{\partial}{\partial\varphi_1}\right)\\
j_{2+} &= e^{-i\varphi_2}\left(\frac{\partial}{\partial\theta_2} + i\cot\theta_2\frac{\partial}{\partial\varphi_2}\right) \qquad (4.7)
\end{aligned}
$$

for i = 1,2 and

$$
C_{\pm}(J,K) = \sqrt{J(J+1) - K(K+1)} \qquad (4.8)
$$

where J is the total angular momentum with component K and R_3.

For NH_3, the transformation $\varphi = \varphi_2 - \varphi_1$ and $\kappa = \varphi_1$ results in a form that can be used directly with the potential surfaces. Thus for $J = 0$ the 6D NH_3 KE operator is written

$$
\begin{aligned}
2\hat{T} &= \sum_{i=1}^{3}\left(-\frac{1}{\mu_i}\frac{\partial^2}{\partial r_1, r_2, R}\right) - \left(\frac{1}{\mu_1 r_2^2} + \frac{1}{\mu_3 r_1^2}\right)\\
&\quad \left[\frac{1}{\sin\theta}\frac{\partial}{\partial\theta}\sin\theta\frac{\partial}{\partial\theta} + \frac{1}{\sin^2\theta^2}\frac{\partial^2}{\partial\kappa^2}\right]\\
&- \left(\frac{1}{\mu_2 R^2} + \frac{1}{\mu_3 r_1^2}\right)\left[\frac{1}{\sin\gamma}\frac{\partial}{\partial\gamma}\sin\gamma\frac{\partial}{\partial\gamma}\frac{1}{\sin^2\gamma}\frac{\partial^2}{\partial\gamma^2}\right]\\
&- \left(\frac{1}{\mu_1 r_1^2} + \frac{1}{\mu_3 r_2^2}\right)\left[\frac{1}{\sin^2\theta}\left(\frac{\partial^2}{\partial\varphi^2} - 2\frac{\partial}{\partial\kappa}\frac{\partial}{\partial\varphi}\right)\right]\\
+ &\ e^{i\kappa}\left(\frac{\partial}{\partial\theta} + i\cot\theta\left(\frac{\partial}{\partial\kappa} - \frac{\partial}{\partial\varphi}\right)\right) \times e^{-i(\varphi+\kappa)}\left(-\frac{\partial}{\partial\kappa} + i\cot\kappa\frac{\partial}{\partial\kappa}\right)\\
+ &\ e^{-i\kappa}\left(-\frac{\partial}{\partial\theta} + i\cot\theta\left(\frac{\partial}{\partial\kappa} - \frac{\partial}{\partial\varphi}\right)\right) e^{i(\kappa+\varphi)}\left(\frac{\partial}{\partial\kappa} + i\cot\theta\frac{\partial}{\partial\varphi_2}\right)\Bigg]\\
+ &\ \frac{1}{\mu_2\gamma_1^2}\left[J(J+1) + \left(2\frac{\partial}{\partial\varphi}\frac{\partial}{\partial\kappa} + 2\frac{\partial^2}{\partial\kappa^2} + 2\frac{\partial^2}{\partial\kappa^2} + 2\frac{\partial}{\partial\varphi^2}\right)\right] \qquad (4.9)
\end{aligned}
$$

where

$$\mu_1 = \frac{m_N m_H}{m_N + m_H} \tag{4.10}$$

$$\mu_2 = \frac{m_H(m_N + 2m_H)}{m_N + 3m_H} \tag{4.11}$$

$$\mu_3 = \frac{m_H(m_N + m_H)}{m_N + 2m_H}. \tag{4.12}$$

4.3 Potential Energy Surfaces

For the 2D model, values of the potential can be calculated directly from the Truhlar potential at all the grid points. For the 6D model case, however, this is not possible as it would require a 6D grid of points which is too large for any computer. A more convenient form of the potential function is thus required. The method used is based on the high-dimensional model representation (HDMR) [77] where a potential energy function is represented in terms of known values on planes or lines through a cut in the surface

$$V(\mathbf{q}) = V_0 + \sum_i V_i^{(1)}(q_i) + \sum_{ij} V_{ij}^{(2)}(q_i, q_j) + \sum_{ijk} V_{ijk}^{(3)}(q_i, q_j, q_k) + \cdots \tag{4.13}$$

where $V_i^{(1)}$ and $V_{ij}^{(2)}$ are 1D and 2D functions etc. dependent on coordinates q_i.

The HDMR method thus aims to reproduce a high-dimensional surface by a low-order polynomial. This is very efficient for use in quantum dynamics simulations but is only accurate in a region around the reference point. This is fine for calculating low-lying vibrational states for which it has had great success [78] but presents a problem in a photodissociation process which covers a wide region of the PES. We thus need to expand the surface around a set of reference points which is a non-trivial problem.

For ammonia, reference points were chosen along each DOF, including the global minimum. These reference points are then connected by switching functions to provide smooth interpolation between regions of the surface. In one-dimension, a potential changes its reference point if

$$V(x) = S_1(x)V_1(x) + (1 - S_1(x))V_2(x) \tag{4.14}$$

where S_1 is a switching function which defines the line along which the potential expansion switches from one reference point to the next, and V_1 and V_2 are one-dimensional functions with different reference points, x_1 and x_2 respectively. A plot of switching functions is shown in figure 4.4 showing how the function varies smoothly from a value of one to zero. In this case reference points are at 0.5, 2.0, 3.5 and 5.0. Even for the NH_3 multi-dimensional potential functions, one-dimensional switching functions were used to retain the structure of the HDMR expansion, i.e. a low order polynomial expansion. As a result, all combinations of reference points were required.

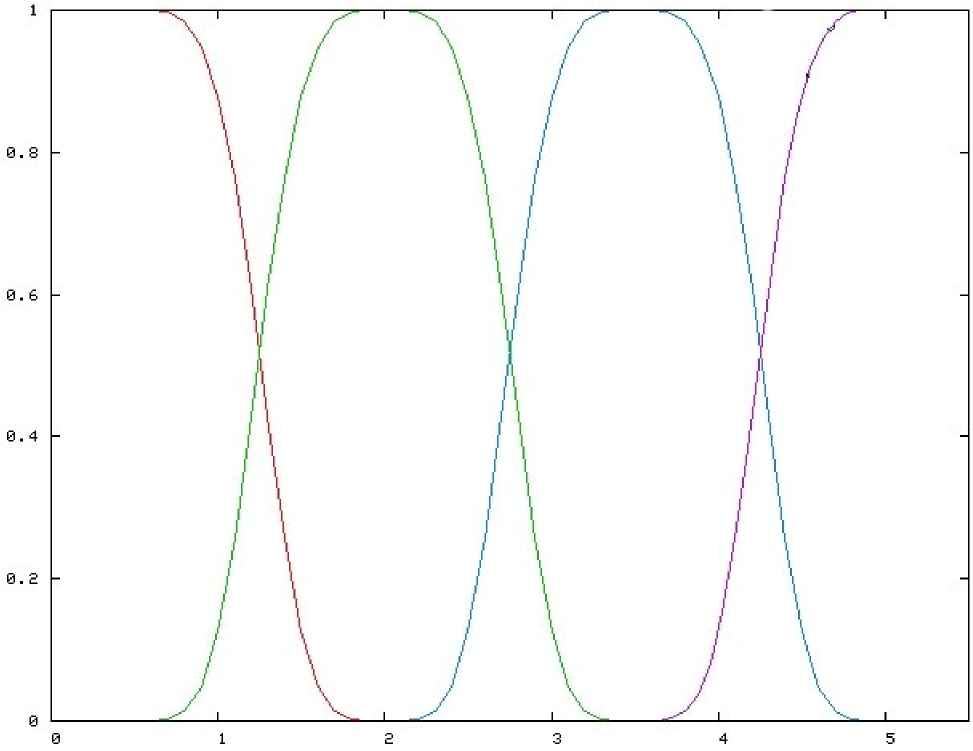

Fig. 4.4: A plot of the 1-dimensional switching functions which provide the interpolation between reference points.

As an example of this, we take two of the DOF used in NH_3, r_1 and r_2. Figure 4.5 shows a 2D plane in r_1 and r_2. Two points have been selected along each coordinate, making four reference points marked a, b, c and d on figure 4.5. S_1 and S_2 refer to the

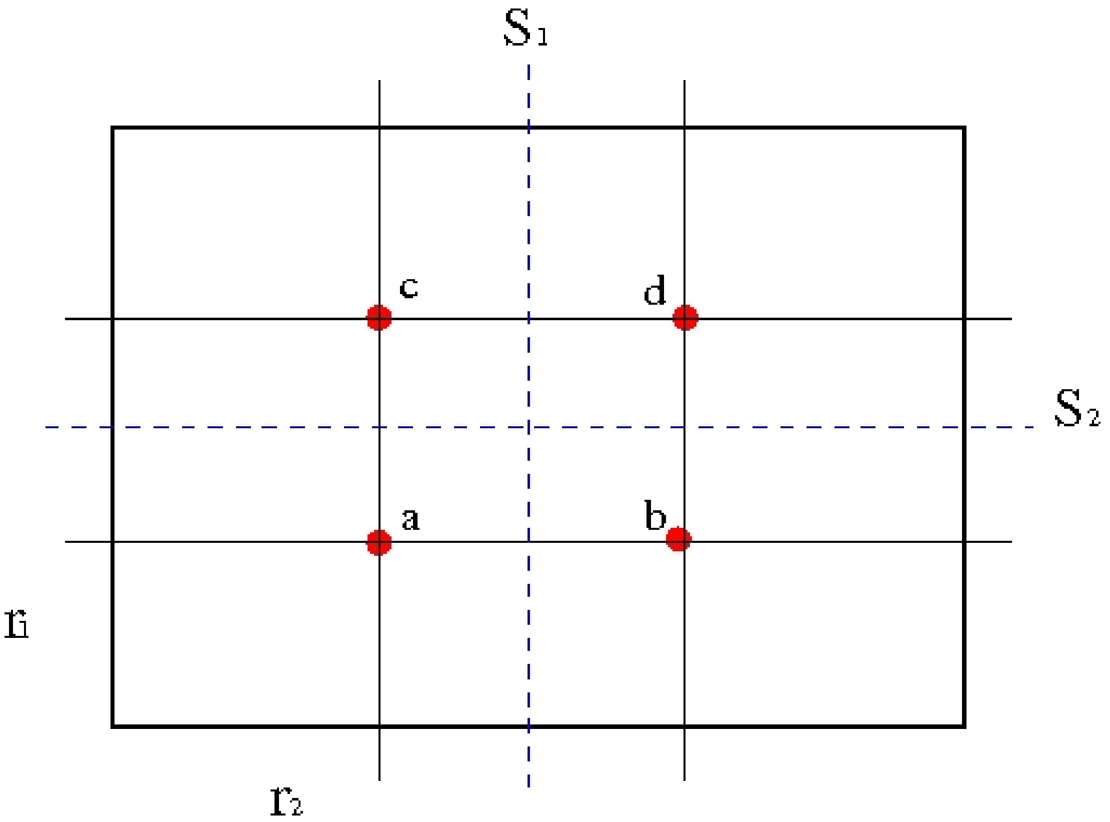

Fig. 4.5: A 2D surface in r_1 and r_2 showing how 1D switching functions are used to interpolate between two reference points along each coordinate.

switching functions which are of the form

$$S(x) = \exp[-(x - x_0 + x_l)1.825/swl]^4 \tag{4.15}$$

where x_0 are the reference values for each DOF and $x - x_0$ is the displacement from the reference geometry. The parameter x_l specifies the starting point of the switching function, and can be used to specify whether it starts on the left or the right of the reference point. The value of 1.825 is an empirical parameter chosen to give the correct steepness and swl is the length of the function.

The potential function for a 2D surface with 4 reference points using switching functions as shown in figure 4.5 is defined as

$$
\begin{aligned}
V &= V_a + V_b + V_{ab} + V_c + V_d + V_{cd} \\
V_a &= V_a^{(1)} + V_a^{(2)} - V_a^{(0)} \\
V_b &= V_b^{(1)} + V_b^{(2)} - V_b^{(0)} \\
V_{ab} &= S_{1a} V_a + S_{1b} V_b \\
V_c &= V_c^{(1)} + V_c^{(2)} - V_c^{(0)} \\
V_d &= V_d^{(1)} + V_d^{(2)} - V_d^{(0)} \\
V_{cd} &= S_{1c} V_c + S_{1d} V_d \\
V_{tot} &= S_{2a} V_{ab} + S_{2b} V_{cd}. \qquad (4.16)
\end{aligned}
$$

where $S_{1b} = 1 - S_{1a}$.

The same philosophy is used to build up the 6D functions as sums of pair potentials. The 1D and 2D functions were then obtained numerically on the grid.

The reference points chosen for the ground, first excited state and for the coupling functions are shown in table 4.1. As a result we have selected 12 points for the ground and first excited states and 10 for the coupling, making 72 reference points for the potential expansion and 32 for the coupling.

Table 4.1: Reference points along each DOF for multi-reference HDMR fitting of the 6D ammonia ground, first excited state and adiabatic coupling functions. Values for R, r_1 and r_2 are in au and for γ, ϕ and θ in radians.

	$\tilde{X}(^1A')$ and $\tilde{A}(^1A'')$			Coupling		Equilibrium Values
R	2.0	4.4	7.0	3.8	6.6	2.0
r_1, r_2	1.9	5.2		2.0	5.0	1.9
γ	0.93193492	1.89023285		1.1488278	2.20965774	1.89
ϕ	0.9125	2.1625	4.975	1.225	3.1	2.10
θ	0.8459181	1.90908808		0.8459181	1.90908088	1.91

4.4 Computational Details

As well as providing an interesting comparison with the 6D model, the 2D model is a relatively simple starting point for the analysis and can be investigated in detail without being too time consuming so that valuable information can be gained in preparation for the complex 6D calculations. For the 2D dynamics the time-dependent wavepacket was propagated on a grid in R and θ with $N_R = 62$ between 1.0 and 14.0 au and $N_\theta = 61$ between -2.0 and 2.0 rad. A FFT DVR was used for the dissociative DOF, R, and an exponential DVR for θ. A CAP was placed on the dissociative channel at 10.0 au to prevent reflection of the wavepacket at the grid edges. The flux analysis was carried out by measuring the amount of dissociating wavepacket going into the CAP for both the ground and excited states as a function of time.

For the 6D dynamics, the wavepacket was propagated on a grid with the $N_R = 62$ between 1.5 and 7.6, N_{r_1} and $N_{r_2} = 47$ between 1.4 and 6.0 au, $N_\gamma = 29$ between 2.5 and 0.7, $N_\phi = 17$ between 0.6 and 5.6 and $N_\theta = 32$ between 2.6 and 0.7 rad. The DVR's used were a FFT for R and r_1, sin DVR for r_2, a Legendre DVR for γ and θ and an exponential DVR for ϕ. A CAP was placed along R at 5.0 au and at r_1 and r_2 at 4.5 au to prevent the wavepacket hitting the grid ends.

4.5 Results for 2D Model

4.5.1 2D Potential Energy Surfaces

The $\tilde{X}$ ground and $\tilde{A}$ excited state surfaces used in the dynamics are shown in figure 4.6 and are taken from Truhlar *et al* [72, 73]. The characteristic double minima is visible in the ground state and the CI can be seen at $\theta = 0$ where NH_3 is in the planar D_{3h} configuration.

Due to the double well potential the two lowest vibrational states, ψ_0 and ψ_1, are very close in energy ($\Delta\ E = 0.79$ cm^{-1}). In a harmonic approximation of the wells, the ground state is degenerate with a Gaussian wavefunction in each well. The

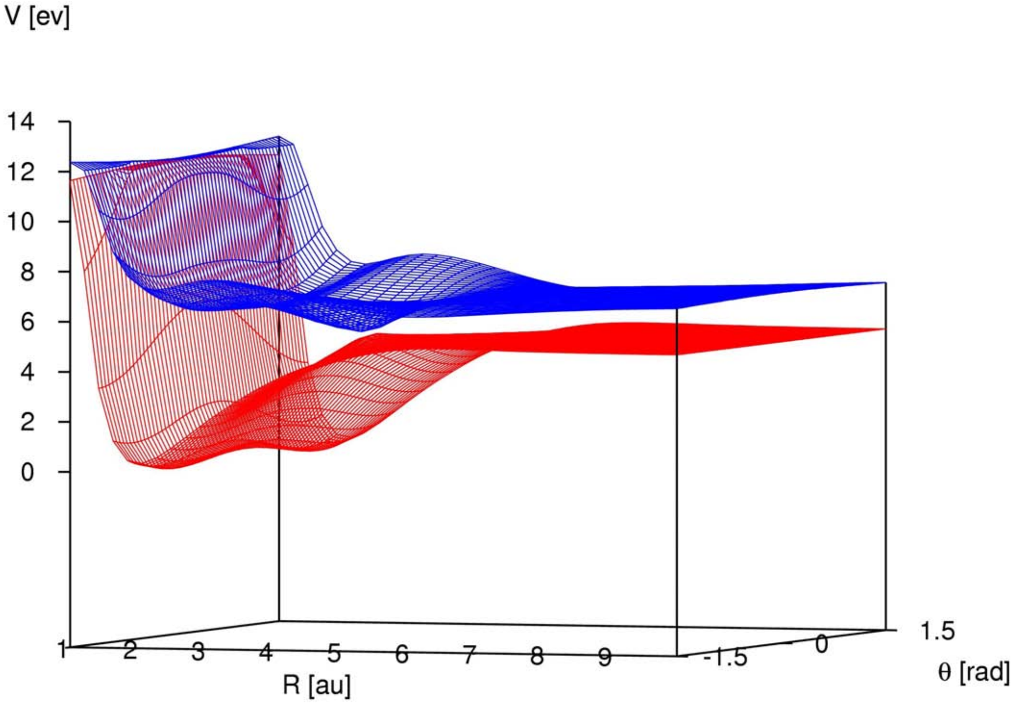

Fig. 4.6: Potential energy surfaces for the $\tilde{X}$ and $\tilde{A}$ states of NH_3 in R, the N-H dissociative bond distance, and θ, the N-NH_2(COM)-H angle.

real wavefunction of the ground state and the first excited state is $\psi_0 = \chi_l + \chi_r$ and $\psi_1 = \chi_l - \chi_r$.

Thus while ψ_0 and ψ_1 have density in both wells, the superposition $\psi_0 + \psi_1$ has density only in one well and provides a reasonable initial wavefunction as the two states are fairly equally populated at reasonable temperatures.

Three calculations were made using different initial positions for the wavepacket dynamics. Firstly the Gaussian wavepacket was relaxed on the ground state into one well: its initial position was $R_e = 2.0$ au and $\theta_e = 0.9$ rad. After vertical excitation to the excited state the wavepacket was propagated over several timescales from 100 fs to 4 ps with the wavepacket being output at 0.5 and 0.25 fs. Secondly, the wavepacket was relaxed into both wells of the ground state to find ψ_0 and propagated on the excited state for 100 and 200 fs. Finally the wavepacket was relaxed to find the eigenstate ψ_1

and this was propagated on the excited state for 100 fs.

4.5.2 2D Wavepacket Dynamics: Relaxation and Propagation from One Well of the Double Minimum

The molecular dynamics for propagation of the wavepacket from one well of the ground state to the excited state are shown in figures 4.7 and 4.8 with the PES shown as contour plots at the top. At $t = 0$ the wavepacket is complete in the excited $\tilde{A}$ state at $R = 2.0$ au and $\theta = 0.9$ rad. After 6 fs the wavepacket on the excited state has moved across the angle and is now at the planar geometry at $\theta = 0$ but we note that as it arrives at this point no dissociation occurs. We also observe that the ground state is now populated via the CI located at $R = 3.7$ au and $\theta = 0$. At 10.5 fs the wavepacket has reached the other side of the excited state and it is at this point, as it begins to move back that it starts to dissociate diagonally across the angle. On the lower state a portion of the wavepacket has evolved to the opposite well and is also dissociating much in the same manner. After 15 fs the wavepacket has split into two parts on the upper state, the larger portion evolving back across the angle and the other along R to dissociate. This can be seen more clearly at 18 fs.

At 23 fs, figure 4.8, the wavepacket has returned to its initial position on the excited state. It is this recurrence time that is responsible for the main progression in the calculated spectrum. At 28.5 fs we note that as the wavepacket approaches the minimum once again a portion of it dissociates diagonally. After the wavepacket has reached the other side of the surface it seems to spread across the angle and at 42 fs we see a partial recurrence which manifests as a low intensity secondary progression in the spectrum. On the ground state we see that dissociation continues to occur with a small portion trapped in the initial starting position throughout the propagation whilst the rest spreads out across the surface.

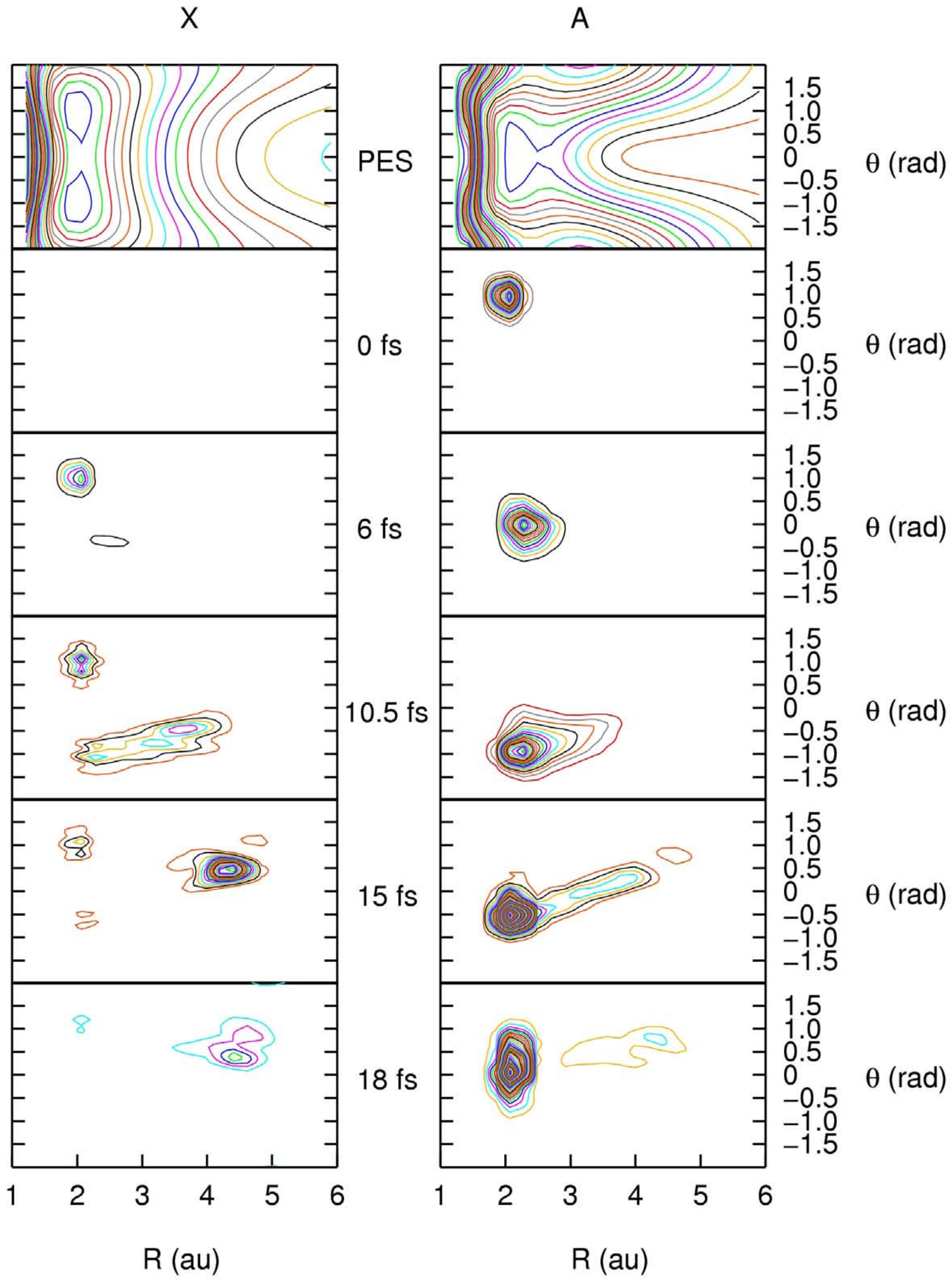

Fig. 4.7: Snapshots taken at 0, 6.0, 10.5, 15.0 and 18.0 fs of the molecular dynamics of NH_3 after excitation from one well of the ground state and propagation on the excited $\tilde{A}$ state. The potential energy surfaces are shown as contour plots at the top.

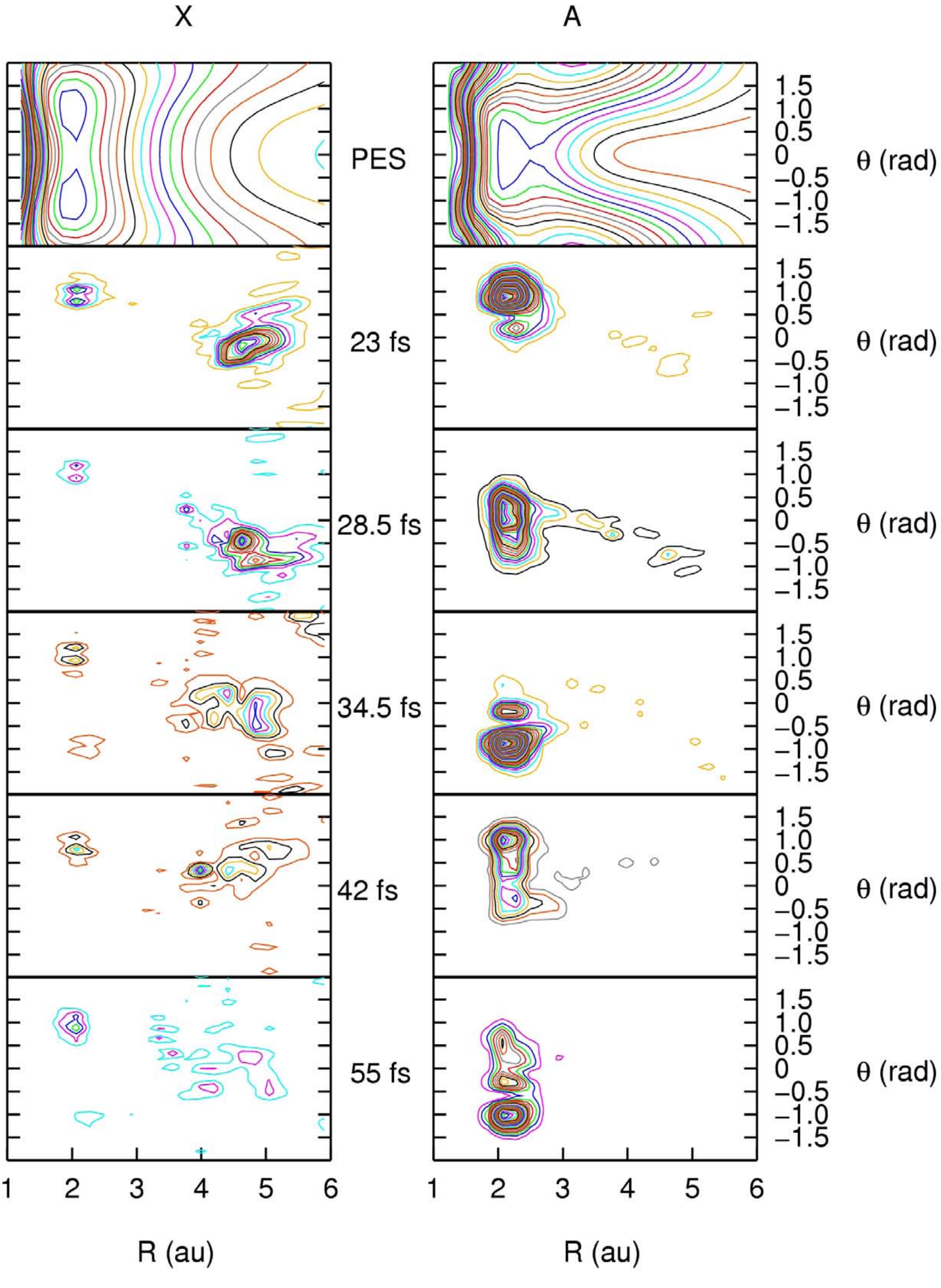

Fig. 4.8: Snapshots taken at 23.0, 28.5, 34.5 and 55.5 fs of the molecular dynamics of NH_3 after excitation from one well of the ground state and propagation on the excited $\tilde{A}$ state. The potential energy surfaces are shown as contour plots at the top.

4.5.3 2D Wavepacket Dynamics: Relaxation and Propagation from Two Wells of the Double Minimum

The dynamics in figures 4.9 and 4.10 were carried out after excitation to the excited state from ψ_0 which has density in both wells of the ground state. At 0 fs we see once again that the total wavepacket is excited to the upper state from both wells of the ground state and that after just 3 fs the lower state has also become populated via the CI.

On the upper state the wavepacket has moved across the angle and by 5 fs the two portions of the wavepacket are interfering with each other. Again we see that although the wavepacket has reached the angle of zero it does not dissociate the first time it gets there. Instead it moves away again and then begins to dissociate diagonally across the angle. At 10.5 fs the wavepacket has returned to its initial position and dissociation is occurring on both the ground and excited states. On the excited state a large portion of the wavepacket has returned to its initial position but with some density spread across the angle whilst it dissociates. On the ground state the wavepacket begins to dissociate from both wells as two separate parts. As it propagates along R the two dissociating parts join together until at 14.5 fs they form one portion. At 14.5 fs we see once again the dissociation on the excited state after the two portions have reached the planar angle.

On the excited state at 16.5 fs the wavepacket appears to be dividing into three parts and indeed as it evolves in time we see that after 33 fs there are three distinct portions, one in each of the two initial positions and one which remains at the planar angle. On the ground state we see continued dissociation with small parts remaining in the two wells throughout the propagation.

The dynamics starting from ψ_1 are similar to those from ψ_0 in the timescales. The difference is that the central density seen at 5 fs does not form, instead the outer two density regions bifurcate so that by 33 fs four regions are seen on S_1 rather than three.

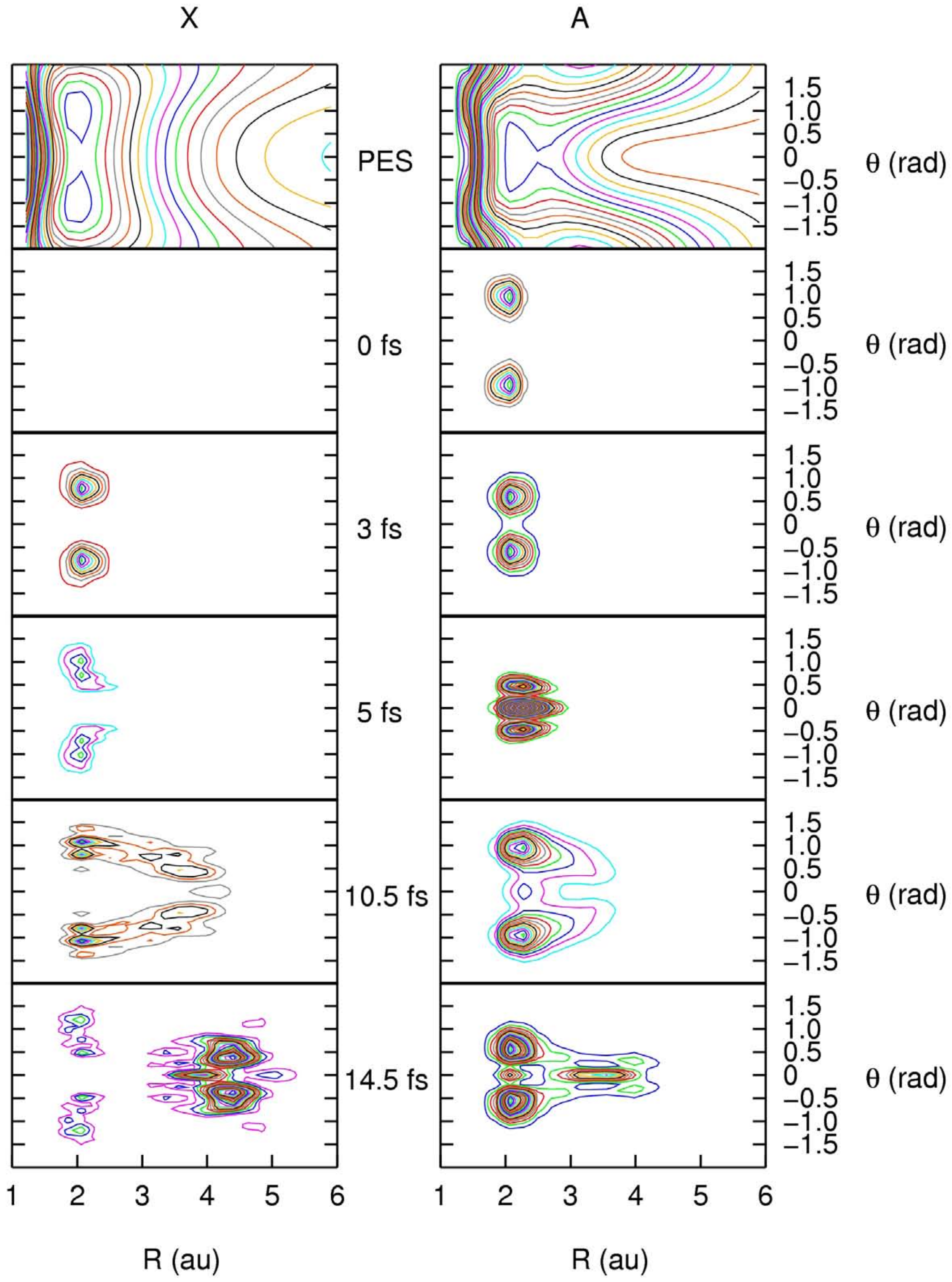

Fig. 4.9: Snapshots taken at 0, 3.0, 5.0, 10.5 and 14.5 fs of the molecular dynamics of NH_3 after excitation from both wells of the ground state and propagation on the excited $\tilde{A}$ state. The potential energy surfaces are shown as contour plots at the top.

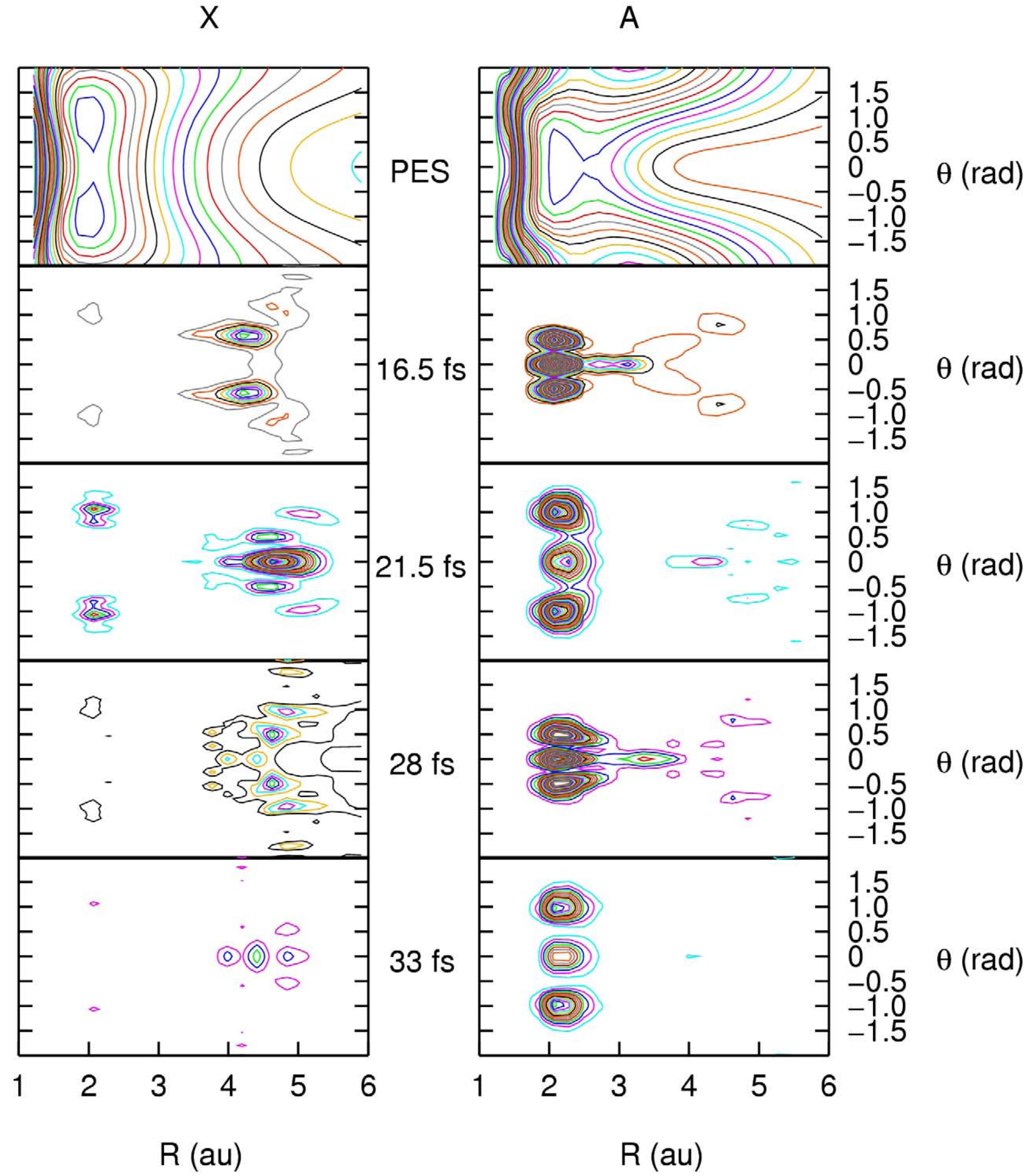

Fig. 4.10: Snapshots taken at 16.5, 21.5, 28.0 and 33.0 fs of the molecular dynamics of NH_3 after excitation from both wells of the ground state and propagation on the excited $\tilde{A}$ state. The potential energy surfaces are shown as contour plots at the top.

The dynamics shown in figures 4.7 and 4.8 is a result of the interference between the two parts of the superposition.

4.5.4 Absorption Spectrum Calculated from the 2D Wavepacket Dynamics

The spectra generated from the 2D dynamics are shown in figure 4.11. Spectrum (a) was generated from the dynamics of the wavepacket from one well, $\psi_0 + \psi_1$. The initial state of this wavepacket corresponds to the $\frac{1}{\sqrt{2}}(\psi_0 + \psi_1)$ vibrational state. We see a main progression with frequency ≈ 1200 cm^{-1} corresponding to the wavepacket recurrence time of 23 fs. This frequency is larger than the 878 cm^{-1} experimental value for the umbrella mode. The position of the maximum is found to be at ≈ 51200 cm^{-1} which is in good agreement with the experimental spectrum of Tannenbaum *et al* [68].

Spectrum (b) was generated from the propagation of the wavepacket out of two wells. This corresponds to the wavepacket being excited from the ψ_0 vibrational state and we see that in this spectrum we have some of the peaks from spectrum (a). The same can be seen for spectrum (c) in which the wavepacket was started from the ψ_1 state. We find from our results that the relaxation energies for the ψ_0 and ψ_1 states give a splitting of 13 cm^{-1}, somewhat bigger than the experimental tunneling splitting of 0.79 cm^{-1}.

It can be seen that the spectrum in (a) is a sum of the spectra in (b) and (c). The explanation for this is that due to symmetry, ψ_0 and ψ_1 can only be excited into every second vibrational level in S_1 resulting in missing lines.

4.6 Results for 6D Model

4.6.1 6D Potential Energy Surfaces

The 6D ground and excited state PES are shown in figure 4.12 plotted along the dissociation coordinate R and the angles ϕ, γ and θ. The plot of R and ϕ shows the double well potential and the CI at $R = 4$ au and $\phi = 3$ rad. The plot of R and γ

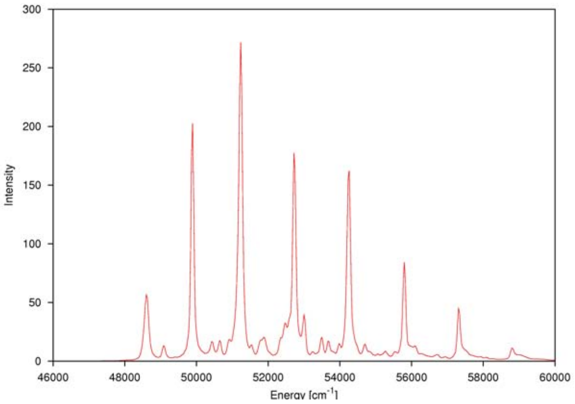

(a) Calculated absorption spectrum from 2D dynamics after excitation of a wavepacket from one well of the ground state.

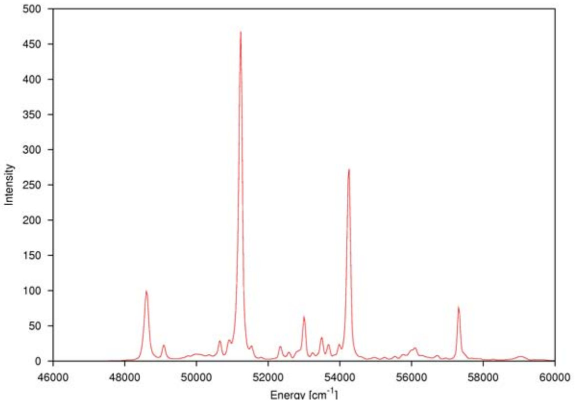

(b) Calculated absorption spectrum from 2D dynamics after excitation of a wavepacket from two wells of the ground state, ψ_0.

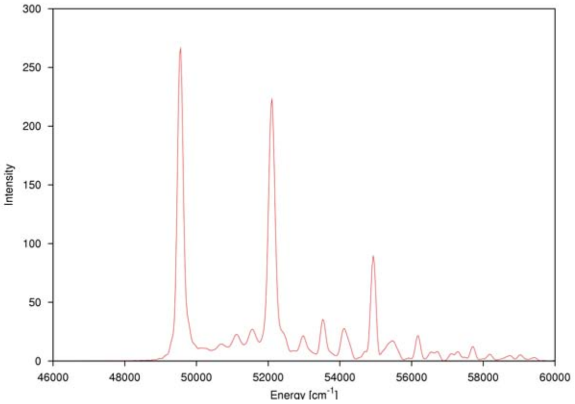

(c) Calculated absorption spectrum from 2D dynamics after excitation from the ψ_1 vibrational state.

Fig. 4.11: Calculated absorption spectra for NH_3 from the molecular dynamics of the propagation of a wavepacket on the excited $\tilde{A}$ state after excitation from the (a) $\psi_0 + \psi_1$, (b) ψ_0 and (c) ψ_1 vibrational states of the $\tilde{X}$ ground state.

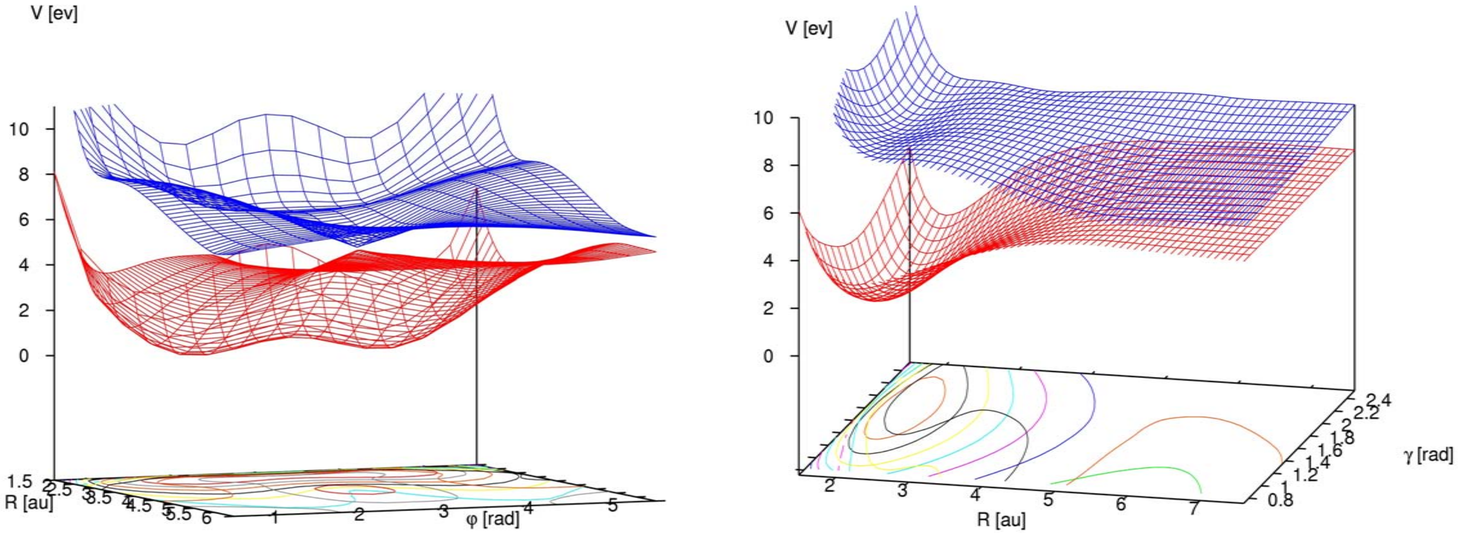

(a) Plot of R and ϕ

(b) Plot of R and γ

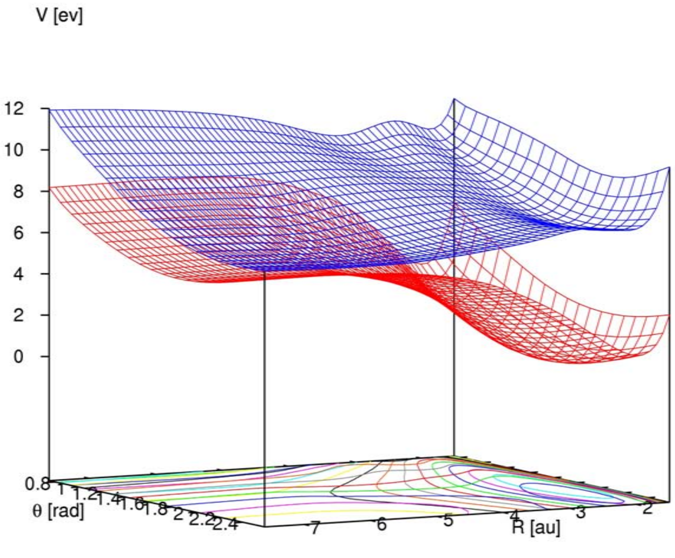

(c) Plot of R and θ

Fig. 4.12: NH_3 ground and first singlet excited states along R and ϕ, R and γ and R and θ for the 6D model.

shows that there is a well in the ground state and that the upper surface is fairly flat. Plot (c) along θ shows that as the distance R increases the upper surface slopes steeply down across the angle.

4.6.2 6D Dynamics

Snapshots of the wavepacket dynamics for the 6D model are shown in figures 4.13 and 4.14 with contour plots of the ground and excited states shown at the top plotted along R and ϕ. Comparing the contour plot of the excited state with the equivalent plot for the 2D model in figure 4.9 we see that the topology of the two surfaces differs. In the plot for the 6D model we see that the point at which the CI occurs is more well defined. By allowing the dissociating H atom to move both in and out of plane relative to the NH_2 group in the 6D model we see that this has had a significant effect on the topology of the excited state offering a higher level of accuracy compared with the 2D description where the dissociating H atom does not have the in plane motion.

At 0 fs the wavepacket resides in both the ground and excited states but with a much higher density on the upper state. After 6 fs a substantial amount has found its way onto the ground state and immediately it begins to extend along R. After 10 fs the wavepacket is propagating down R on both the upper and lower states and on the upper state the two portions of the wavepacket have moved inwards across the angle and are interfering with each other. In comparison to the 2D dynamics, in which the ground state wavepacket dissociated from its initial position and propagated diagonally across the angle, we see that here it dissociates at a fixed angle.

At 18 fs and after 26 fs pieces of the wavepacket have broken away from the main part on the ground state and are dissociating. We notice that on the upper state the wavepacket is still spread across the angle but that there are two main areas of density. Comparing this to the 2D dynamics where there were three distinct portions of wavepacket after 33 fs we see that the behaviour of the wavepacket is somewhat different in this respect. At 28 fs the wavepacket on the upper state has formed into

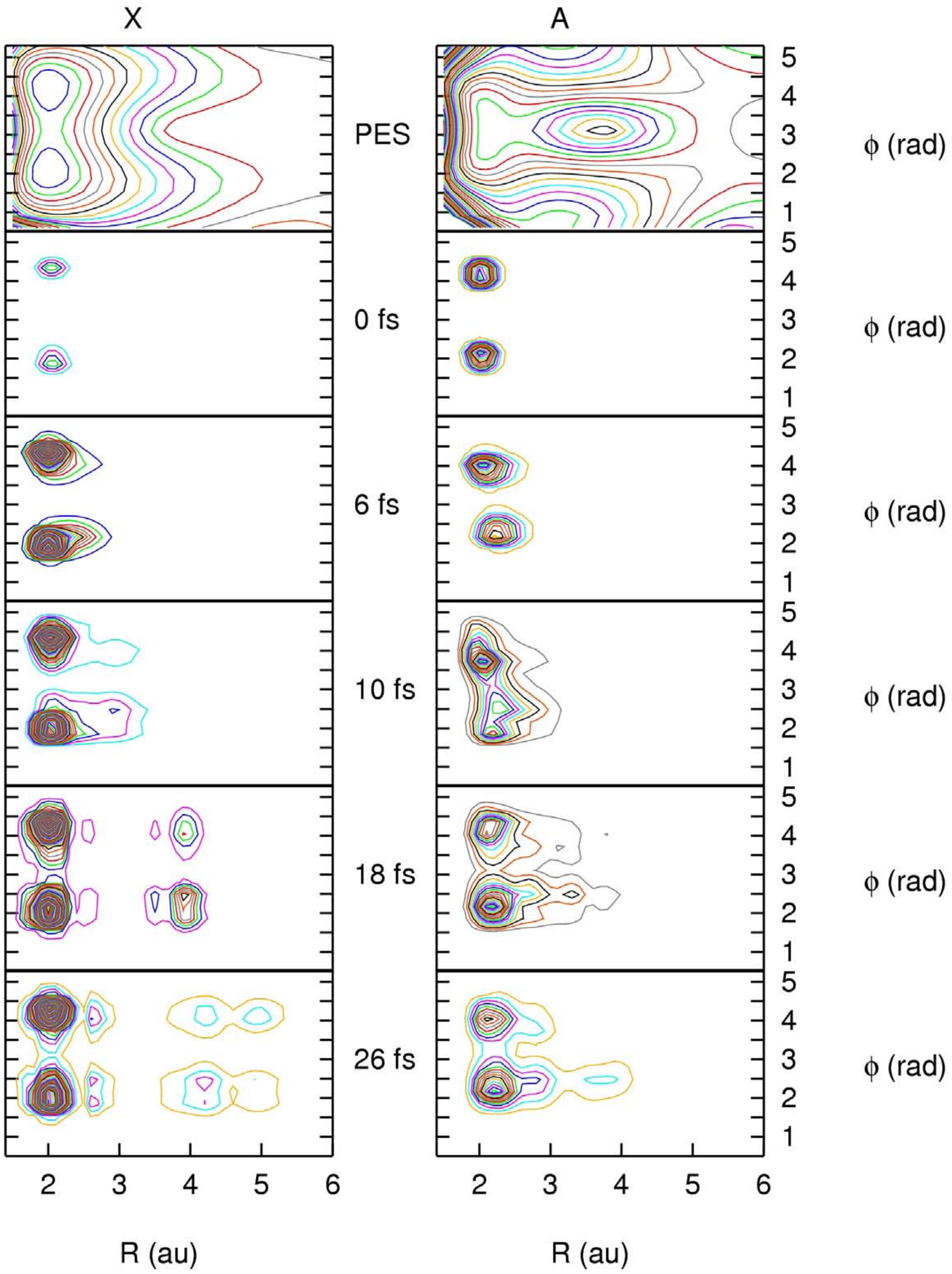

Fig. 4.13: Snapshots taken at 0, 6.0, 10.0, 18.0 and 22.0 fs of the molecular dynamics of NH_3 after excitation from both wells of the ground state and propagation on the excited $\tilde{A}$ state. The potential energy surfaces are shown as contour plots at the top.

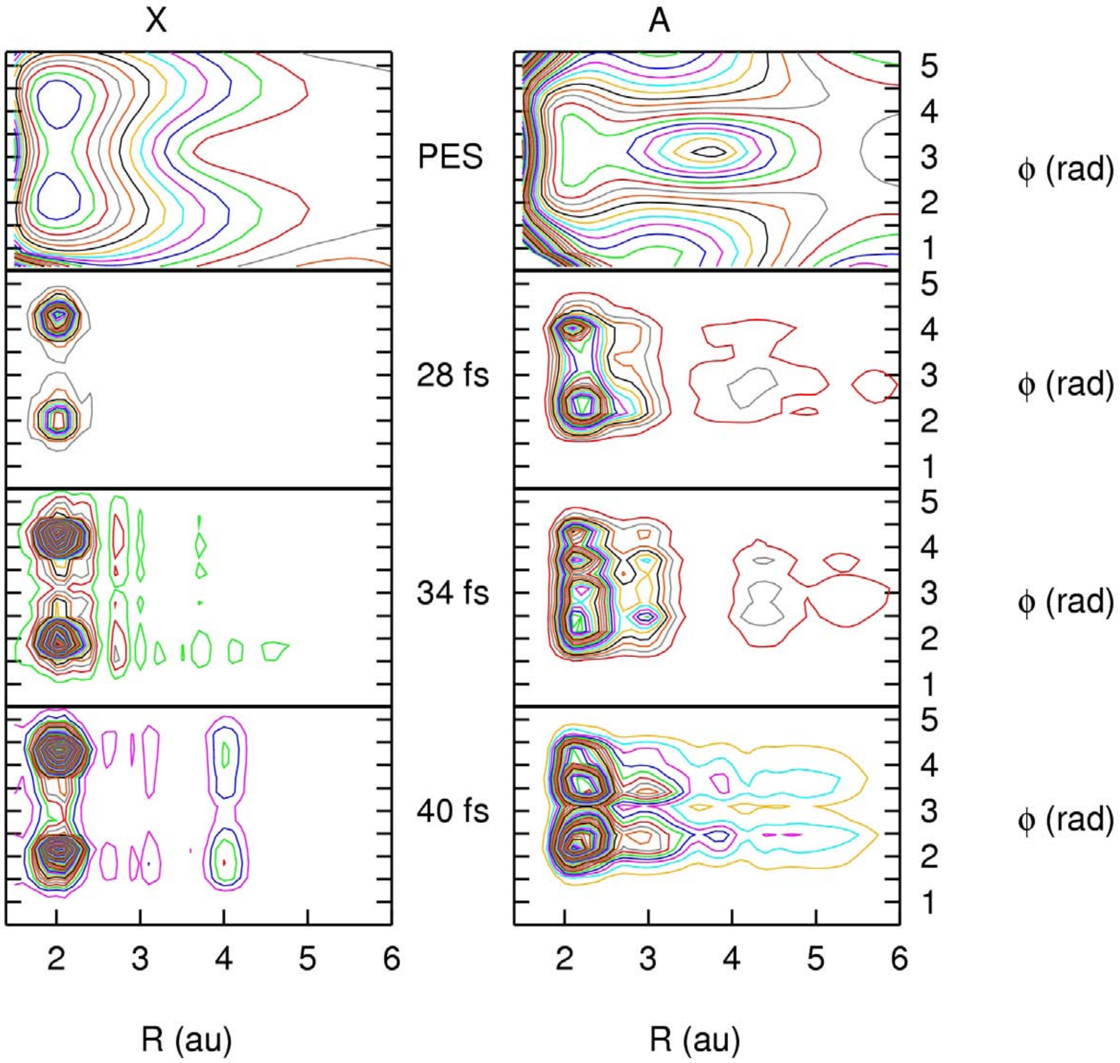

Fig. 4.14: Snapshots taken at 28.0, 34.0 and 40.0 fs of the molecular dynamics of NH_3 after excitation from both wells of the ground state and propagation on the excited $\tilde{A}$ state. The potential energy surfaces are shown as contour plots at the top.

one portion and is spread across the angle with small pieces dissociating from the main density. The ground state wavepacket has largely remained in its initial position.

4.6.3 Absorption Spectrum Calculated from the 6D Wavepacket Dynamics

The absorption spectrum generated from the 6D dynamics is shown in figure 4.15. The spectrum does not exhibit a simple main progression but rather appears to consist of several different frequencies with spacings of approximately 1000 cm^{-1}. This can be attributed to two factors, either the surfaces are not accurate enough or the fact that the dynamics calculation has not converged and needs a longer propagation time.

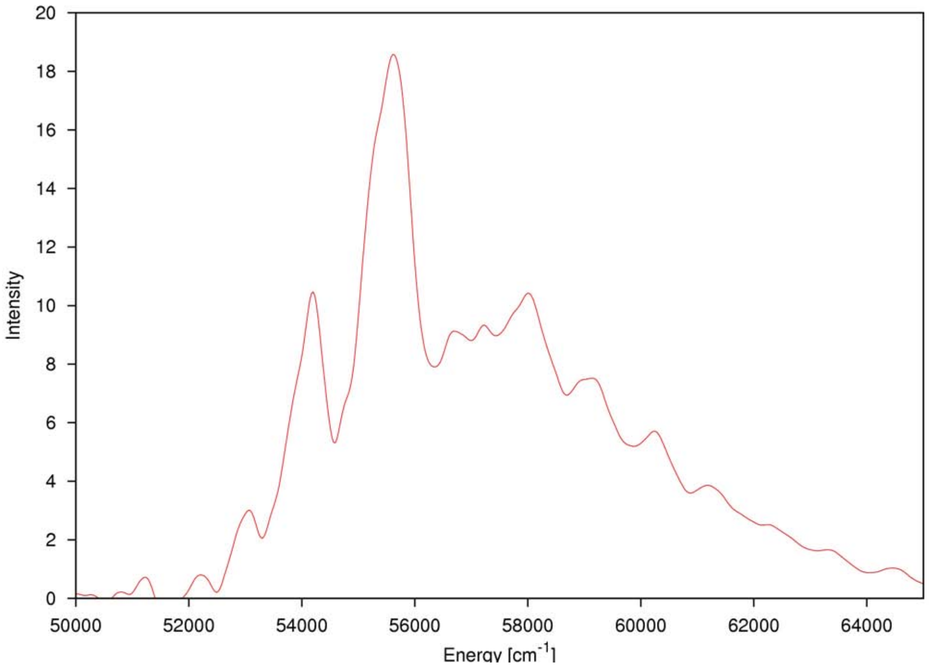

Fig. 4.15: Absorption spectrum calculated from the 6D wavepacket dynamics for NH_3.

4.7 Flux Analysis and Branching Ratio

The important quantity defining the photodissociation is the total amount of the system that dissociates, and the branching ratio that says how much of the system dissociates on S_1 and how much on S_0. These quantities can be obtained by analysing the flux into the dissociative channels.

The flux analysis was carried out using the MCTDH programs and is described in section 3.3.6. The total flux was calculated for the 2D calculations starting from ψ_0 and $\psi_0 + \psi_1$, and for the 6D dynamics. In each case we calculated the flux for the ground and excited states separately so that the branching ratios could be determined. A plot of the flux, W_{tt}, against time from the single well 2D propagation is shown in figure 4.16. This plot was taken from the flux analysis for the 2000 fs propagation with

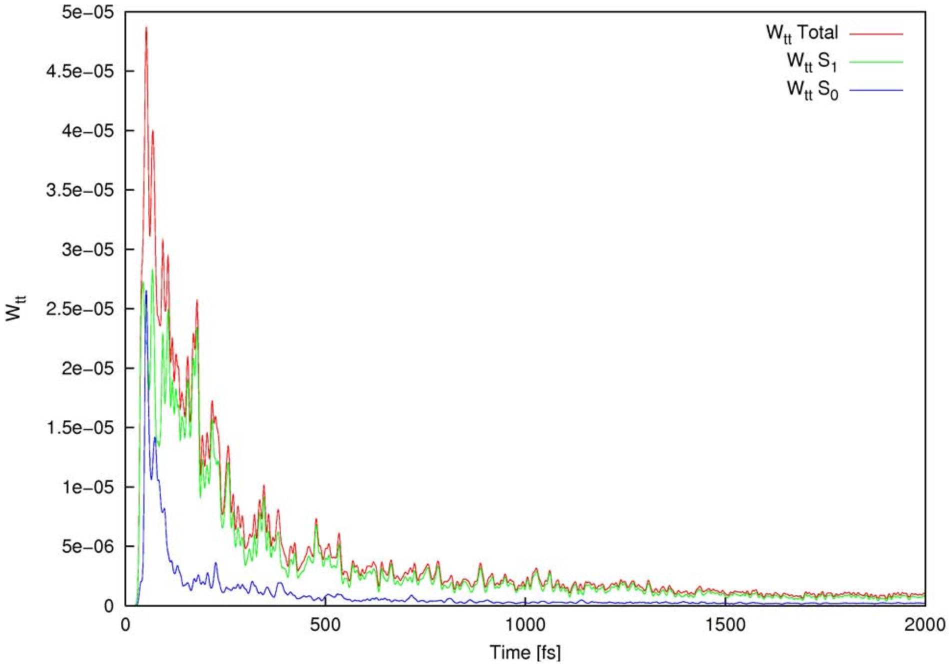

Fig. 4.16: Plot of the measured flux from the propagation of a wavepacket on the 2D NH_3 PES. The plot shows the total flux, W_{tt}, and the flux for the ground, $W_{tt}S_0$, and first excited, $W_{tt}S_1$, states.

a wavefunction output of 0.5 fs which means that the flux is calculated every 0.5 fs. Figure 4.16 shows the total flux and the flux for the two states as a function of time. We can see from the plot that after 1000 fs the process is effectively over and that after 500 fs that there is very little activity on the ground state.

The branching ratio was calculated by integrating W_{tt}, equation 3.76, for the two states and then taking the ratio of $\int W_{tt}S_1/\int W_{tt}S_0$. The results for the full flux analysis are shown in table 4.2. The data shows the total flux for each system and for the S_0 and S_1 states separately. The integration was done using Simpsons rule. Sensitivity to step size was checked by repeating the longest calculations with a 0.25 fs output time, which resulted in no significant difference in values.

Firstly we discuss the results for propagation from one well for the 2D system. The propagation was run for a maximum of 4000 fs to allow as much of the wavepacket as possible to dissociate. Here the branching ratio is 3.68:1 in favour of dissociation on the excited state. A good level of accuracy is obtained throughout the 2D calculations as $1 - |\langle\psi|\psi\rangle|^2$ is equal to $2 * \int W_{tt}$ up to 0.001. This is a measure of completeness as $|1 - \langle\psi|\psi\rangle|^2$ at time T tells us how much of the wavepacket has dissociated and the integral 2 x $\int W_{tt}$ is a measure of the amount of wavepacket that has gone into the CAP. If these differ then the wavepacket is still moving into the CAP.

By reducing the total propagation time to 2000 fs the branching ratio changes to 3.80:1, a marginal change but an indication that there is some slow moving portion of the wavepacket dissociating via the ground state after 2000 fs which reduces the branching ratio. At 1000 fs the data gives a ratio of 3.70:1 and we would consider this the minimum time for a propagation to give accurate results. After 200 fs the ratio is 3.05:1 which shows a significant difference compared with the longer propagation times, but still a reasonable value. At 100 fs however the ratio drops to 1.84:1 and if we look at the data for the flux on the ground state we see that the value at 100 fs is already half that of the flux at 1000 fs.

Table 4.2: The results for the flux analysis for the 2D and 6D dynamics carried out at various propagation times. The wavepacket was also propagated from one well and from two wells for the 2D model and from both wells for the 6D model. Data for the total flux and for the ground and excited states is shown as well as the branching ratios.

	Wavepacket propagated from one well 2D					Wavepacket propagated from both wells		
							2D	6D
t final (fs)	4000	2000	1000	200	100	200	100	100
wavepacket norm	0.43583703	0.51772490	0.61254610	0.81680179	0.90978443	0.76538224	0.88678508	0.44387788
$\int \mathbf{W_{tt}}$ **Total**	0.40502109	0.36597370	0.31238207	0.16633369	0.08597521	0.20699148	0.10662291	0.47024793
$\int \mathbf{W_{tt}S_0}$	0.08660752	0.07638121	0.06660456	0.04110515	0.03031075	0.03942422	0.02966697	0.10506603
$\int \mathbf{W_{tt}S_1}$	0.31841357	0.28959249	0.24577751	0.12522854	0.05566446	0.16756726	0.07695594	0.36518190
$\mathbf{1} - (\mathbf{norm})^{\mathbf{2}}$	0.81004608	0.73196093	0.62478728	0.33283484	0.17229229	0.41419003	0.21361222	0.80297243
$\mathbf{2} * \int \mathbf{W_{tt}}$	0.81004218	0.73194740	0.62476414	0.33266738	0.17195042	0.41398296	0.21324582	0.94049586
$\int W_{tt}S_1 / \int W_{tt}S_0$	3.68	3.80	3.70	3.05	1.84	4.25	2.59	3.48

Between 1000 and 2000 fs there is an increasing ratio in favour of dissociation on the excited state. Up to 4000 fs this ratio is decreasing. It is clear from the data for 100 fs that there has not been a significant amount of dissociation on the excited S_1 state: The total flux on S_1 is 0.056 compared with 0.246 for 1000 fs.

The results for the propagation from both wells in the 2D system has a branching ratio of 4.25:1 in favour of the excited state after 200 fs. Clearly there is more dissociation via the excited state when the wavepacket is excited from both wells of the ground state. We now discuss the 6D results in which propagation of the wavepacket was from both wells and for a time of 100 fs. We also carried out the same propagation time for the 2D system for a direct comparison. The first point to note is that much more of the system dissociates for the 6D model: after 100 fs the norm has dropped to 0.44 whereas in the 2D model it is still at 0.88 at this time. The branching ratio of 3.48 is however similar to the 2D results if we accept that the 6D photodissociation has nearly finished by this time, unlike the 2D model. If we compare the values for $\int W_{tt} S_1$ for the 2D and 6D results, 0.077 and 0.366, we see that there has been significantly more dissociation on the excited state in the 6D system than in the 2D.

Figure 4.17 shows plots of the flux for the ground and excited states as well as the total flux for the 2D and 6D systems for propagation from both wells. For the 6D model the flux down only one of the three equivalent channels is shown. These plots clearly show the difference in the branching ratios between the two systems. Looking at the 6D plot it can be seen that there is more dissociation on the S_1 state compared with the S_0 state giving rise to the 3.48:1 ratio whereas the 2D system only has a 2.59:1 ratio in favour of the excited state.

By 100 fs we see that in the 2D system the flux is still high for both states but in the 6D, the ground state flux is dropping rapidly off as if it has reached completion. The 6D plot is also quite highly structured with periods of high and low flux activity.

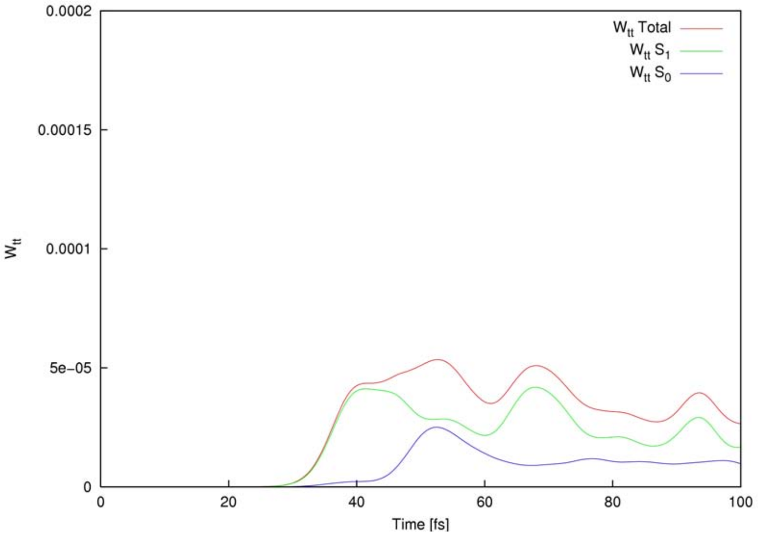

(a) Plot of the total flux and the ground and excited state flux for the 2D model.

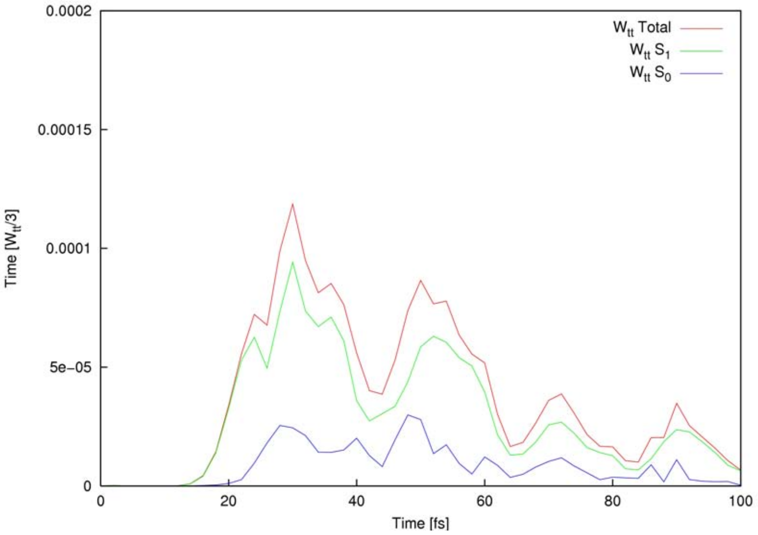

(b) Plot of the total flux and the ground and excited state flux for the 6D model.

Fig. 4.17: Plot of the measured flux from the propagation of a wavepacket on the 2D and 6D NH_3 PES. The plot shows the total flux, W$_{tt}$, and the flux for the ground, W$_{tt}S_0$, and first excited, W$_{tt}S_1$, states.

4.8 Conclusions

In this study we have investigated the photodissociation of NH_3 by using two different models. Much information was gained from the 2D model in terms of relaxation and propagation times in preparation for the more complex 6D calculations. For the 2D model we have shown that after relaxation onto the $\tilde{X}$ ground state and propagation on the $\tilde{A}$ excited state that dissociation takes place on both the lower and upper states via the CI. After carrying out a flux analysis we have calculated branching ratios which show that consistently more dissociation occurs on the excited state than on the ground state.

We have also shown how relaxation of the wavepacket into one or two of the ground state minima affects the branching ratio for the reaction and have concluded that the ratio is increased in favour of the excited state for the latter. Several propagation times were used for the excitation from one well and the results from the flux analysis show that from 100 fs to 2 ps the amount of dissociation on the excited state increases relative to that of the ground state but that after 4 ps we see a drop in the ratio. This extended timescale has revealed that there is some very slow dissociation that occurs on the ground state.

The 6D model surpasses any previous work carried out on this system in its ability to describe the whole molecule. In terms of the dynamics carried out we have propagated over the whole of the excited state surface and not just in the region of the well as Guo *et al* have done.

In comparison with the 2D surfaces a contour plot along R and ϕ shows that the CI is much more well defined in the 6D system due to the extra in plane angular DOF for R. The 6D dynamics have also shown that dissociation occurs on both the ground and excited states. A direct comparison of the 6D and 2D branching ratio shows that in the 6D system there is significantly more dissociation on the excited state and that dissociation occurs more rapidly.

Although the experimental absorption spectrum has not been reproduced in the 2D study we have shown that the spectrum generated from the dynamics of a wavepacket from one well consists of two sets of peaks due to excitation of the wavepacket from the ψ_0 and ψ_1 vibrational states.

The absorption spectrum generated from the 6D dynamics exhibits more than one frequency and again we have not reproduced the experimental spectrum. We attribute this to the non convergence of the dynamics calculations which can cause spurious frequencies to appear. Convergence would be achieved by using more SPFs but of course this extends the time taken for the calculations to run quite substantially and is a consideration for future work. Due to the computational size of the 6D system we have found the dynamics calculations both time consuming and complex in terms of the KE operator. These studies are in their infancy and much work is still to be done on this system in terms of finding convergence and in delving more deeply into the dynamics.

Chapter 5

Potential Surfaces and Dynamics of Nitrosyl Fluoride

5.1 Literature Review

In 1959 the near UV absorption spectrum of FNO was reported by Johnston and Bertin [79]. They observed a strong absorption band from 3.70 to 4.77 eV with a maximum at 3.99 eV and assigned this absorption to the $1^1A'' \leftarrow X^1A'$ transition. They found 3 fundamental vibrational frequencies for the electronic excited state at 1450, 343 and 1086 cm^{-1} and assigned the 1450 cm^{-1} frequency to the NO stretch and the 1086 cm^{-1} to the F-N mode. For comparison the fundamental frequency of NO is 1904 cm^{-1} and the ground state vibrational frequencies are 1844 and 766 cm^{-1} for NO and NF respectively.

Of the few theoretical studies that have been carried out on FNO, most of the work has been concentrated on the ground electronic state [80,81] whereas calculations on the excited states are limited [82–84]. The study carried out by Vasudevan and Grein in 1977 [83] looked at the ground and excited states using combined SCF and configuration interaction calculations. They calculated the energies for the singlet A$'$ and A$''$ states and the VEE. Their results showed good agreement with Johnston and Bertin with a value of 4.22 eV for excitation to the 1^1A$''$ state.

Of most significance to this study is the work carried out by Schinke *et al* [84] who presented a quantum mechanical wavepacket investigation of the $S_0 \rightarrow S_1$ absorption spectrum of FNO. A 2D potential surface for the S_1 (A″) state was produced and time-dependent quantum mechanical calculations were carried out on this surface. A Huzinaga (10s/6p) basis set was used for the Multi-Configuration Self Consistent Field (MCSCF) *ab initio* calculations. The active space included all single and double excitations of the four highest occupied and four lowest unoccupied orbitals of A′ symmetry, as well as the HOMO-LUMO pair of A″ symmetry.

The S_1 potential energy surface was calculated using Jacobi coordinates R and r, where R is the distance from F to the centre of mass of NO and r is the internuclear separation between N and O. R was varied between 2.6 and 6.0 au and r between 1.8 and 3.4 au. The Jacobi orientation angle was fixed at 128.37° throughout. For the dynamics the wavepacket was placed on the excited state at the equilibrium position $R_e = 3.376$ and $r_e = 2.142$ au. The time-dependant dynamics revealed a bifurcation in the wavepacket at the Franck Condon (FC) point with a rapidly dissociating portion due to periodic motion in the R direction and a portion that remained trapped in the shallow well at short F-NO bond distances. These dynamics are shown in figure 5.1, taken from [84]. The calculated absorption spectrum featured a broad background, a consequence of the direct dissociation, and a structured part with two progressions. The frequencies of these progressions were found to be 1030 and 460 cm^{-1}. They assigned the 1030 cm^{-1} frequency to the NO stretching motion within an extremely shallow well, contrary to Johnston and Bertin [79] who assigned this to the N-F mode. Schinke concluded that the 460 cm^{-1} frequency was related to the periodic motion of the wavepacket in the R direction.

Schinke also measured an experimental spectrum which showed good agreement with previous results with a maximum at 32 000 cm^{-1} (3.97 eV) which they assigned to the $1^1\text{A}'' \leftarrow \text{X}^1\text{A}'$ transition. The experimental absorption spectrum by Schinke *et al* is shown in figure 5.2. The main progression is assigned to the N-O stretch and the second progression to the F-NO stretch and the dissociation produces the broad

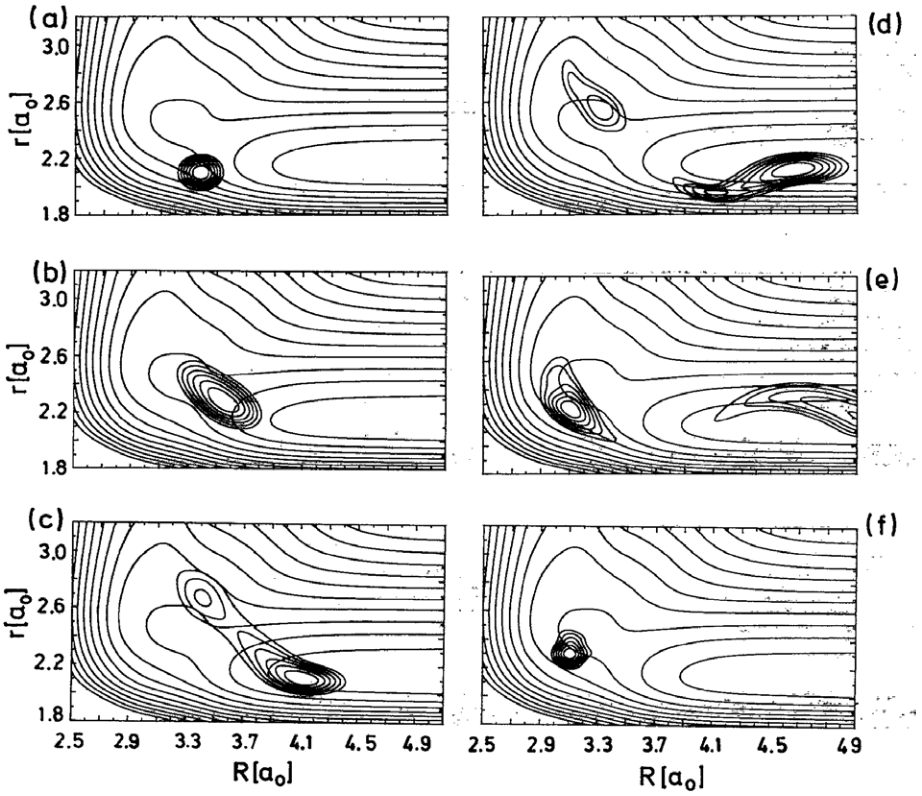

Fig. 5.1: Snapshots of the wavepacket on the first excited state of FNO for (a) 0, (b) 7.26, (c) 14.52, (d) 21.78, (e) 29.04 and (f) 36.30 fs taken from work by Schinke *et al* [84]

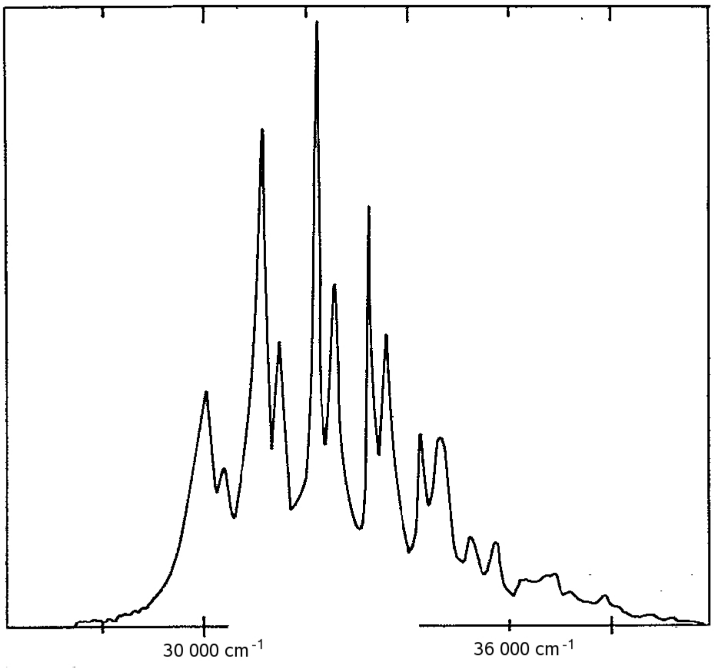

Fig. 5.2: Experimental absorption spectrum for the $S_0 \rightarrow S_1$ transition taken from Schinke *et al* [84].

background.

The fact that the study by Schinke *et al* was carried out with a fixed angle means that it does not give a complete picture of the FNO photodissociation mechanism.

By including the angle in this study we will investigate the effect that this extra DOF has on the dissociation process and in comparison with the previous work will carry out dynamics and produce an absorption spectrum.

5.2 Computational Details

5.2.1 Coordinates

Two coordinate systems were used in this study, binding and Jacobi, and are shown in figure 5.3. The binding coordinates, r_1, r_2 and θ, which denote the N-O and N-F bond distances and the FNO angle respectively were used for calculating the *ab initio* PES. Binding coordinates are representative of the actual bond lengths in the molecule and are therefore more suitable than Jacobi's for the purpose of generating the surfaces at fixed nuclear geometries. The Jacobi coordinates, r, R and γ, which denote the N-O bond distance, the distance of F from the COM of N-O and the angle between them

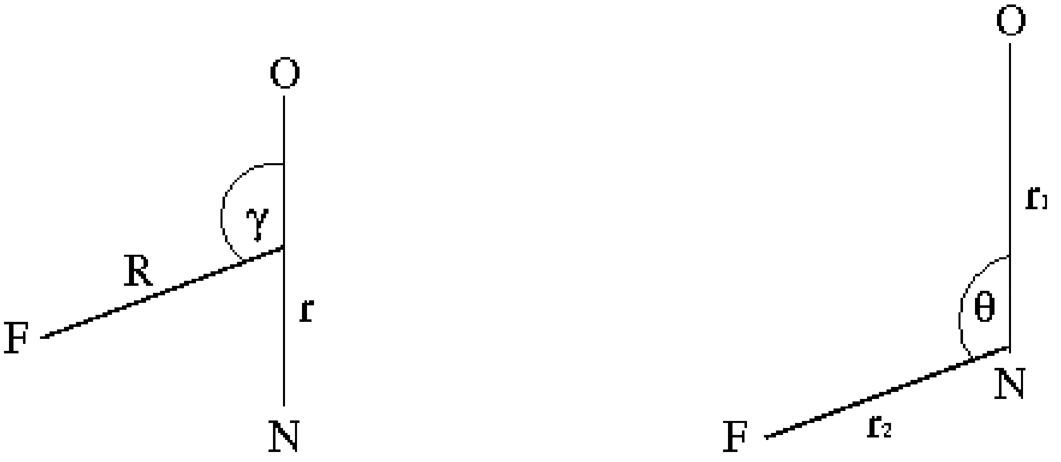

(a) Jacobi coordinates

(b) Binding coordinates

Fig. 5.3: The Jacobi coordinates used for the wavepacket dynamics of FNO. The N-O internuclear separation r, the distance R from the centre of mass of N-O to F and the angle γ and the binding coordinates used to calculate the PES for the ground and first 3 singlet excited states of FNO. The internuclear separations r_1 and r_2 and the angle θ.

respectively were used for all the dynamics calculations. The fact that the KE operator is less complex when written for Jacobi rather than binding coordinates is the rationale for changing coordinates for the dynamics.

The transformation from binding to Jacobi coordinates is carried out using the cosine rule and is shown in equation 5.1. For the purpose of the transformation the N-O distance is denoted r_3, and β is the NOF angle as shown in figure 5.4

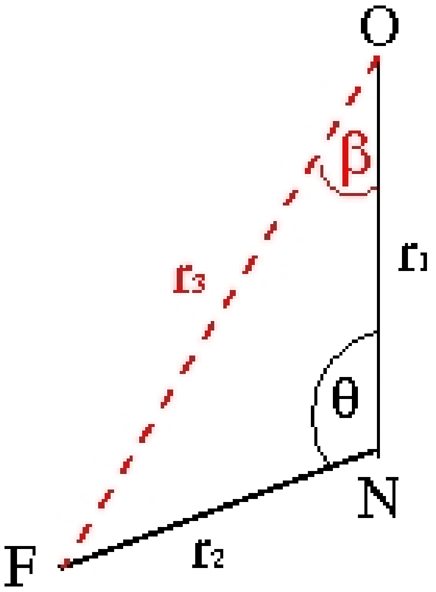

Fig. 5.4: FNO in binding coordinates showing the N-O distance, r_3, and the NOF angle, β which are used in the transformation to Jacobi coordinates R, r and γ.

$$\begin{aligned}
r &= r_1 \\
r_3 &= \sqrt{r_1^2 + r_2^2 - 2r_1r_2\cos(\theta)} \\
r_{O-COM} &= r_1\frac{M_N}{M_N + M_O} \\
r_2^2 &= r_3^2 + r_1^2 - 2r_1r_3\cos(\beta) \\
\cos(\beta) &= \frac{-r_2^2 + r_3^2 + r_1^2}{2r_1r_3}
\end{aligned}$$

$$\begin{aligned} R &= \sqrt{(r_1\frac{M_N}{M_N+M_O})^2 + r_3^2 - 2(r_1\frac{M_N}{M_N+M_O})r_3\cos(\beta)} \\ \cos(\gamma) &= \frac{-r_3^2 + (r_1\frac{M_N}{M_N+M_O})^2 + R^2}{2(r_1\frac{M_N}{M_N+M_O})R} \end{aligned} \tag{5.1}$$

5.2.2 Potential Energy Surfaces

All calculations were carried out using the Molpro 2006 [85] set of programs. The first part of this study was to generate 3D potential energy surfaces. We carried out these calculations for the ground and first three excited states. Extensive *ab initio* calculations were carried out and surfaces were generated at the CASSCF, MS-MR-CASPT2 and MRCI levels using a Huzinaga (10s/6p) basis set throughout. We chose this particular basis set so that we could make direct comparisons with the work by *Schinke et al.* The basis set does not contain polarisation functions and as a result does not recover much dynamic correlation. For the CASSCF a full valence active space was used to include the 2s and 2p orbitals on each atom with the 1s orbitals kept frozen. The wavefunction from this was taken as a reference for the MS-MR-CASPT2 and MRCI. For comparison the VEE, dissociation energy and state energy calculations were also carried out using CASPT2. The FNO molecule possesses C_s symmetry with the ground and second singlet excited states having A' symmetry and the first and third states having A'' symmetry. The electronic states were calculated using state averaged CASSCF with states of the same symmetry within the same calculation. To generate the full surfaces the geometry of the molecule was varied over three coordinates, the N-O bond separation, r_1, the N-F bond separation, r_2 and the FNO bond angle, θ. r_1 and r_2 were varied between 0.8 and 3.8 Å with a stepsize of 0.2Å and θ was varied between -1 and 176° with a stepsize of 6°. A spline fit method of interpolation was used on the *ab initio* data to produce the finished surfaces.

5.2.3 Wavepacket Dynamics

The dynamics were carried out using the MCTDH set of programs. The MS-MR-CASPT2 surfaces were used for the dynamics calculations as these offered the best results energetically. 2D and 3D dynamics were implemented to see the effect on the spectrum. For the dynamics the wavepacket was discretised on a grid in Jacobi coordinates R and r with $\mathrm{N}_R = 201$ between 1.0 and 5.5 au and $\mathrm{N}_r = 151$ between 1.0 and 7.6 au. Three sets of calculations were carried out. Firstly the wavepacket was propagated on the 3D excited state after relaxation on the ground state. Although the PES were calculated for θ from -1 to 176° the dynamics were carried out for θ over the important angles, 52 to 170°.

Secondly we fixed the angle at 2.24 rad and, as Schinke *et al* did, we placed the wavepacket at various positions on the excited state. Finally we repeated the same calculations on the 3D surfaces for comparison. All propagations were run for 200 fs and a CAP was placed on both R and r at 6.0 and 4.5 au respectively to prevent the wavepacket hitting the grid ends.

5.3 Results and Discussion

5.3.1 Energies and Molecular Geometry

The relative energies for the ground and excited states are shown in table 5.1 at each level of calculation and are compared with results from previous studies. MRCI yields the lowest energy for the ground state and all other energies are taken relative to this. The results show that MS-MR-CASPT2 yields the lowest energies for the 3 excited states. However the CASSCF results show significantly higher energies for each state, as much as 0.32 Hartree in the case of the excited states. Comparing the CASSCF with the CI we see that the CASSCF shows the lower energies of the two methods. Compared to the perturbative methods and the MRCI, the CASSCF does produce energies which are surprisingly poor considering a full valence active space was used.

The equilibrium molecular geometry calculated in this study is compared with previous results in table 5.2. The results shown for the CASSCF carried out in this study also represent the values found for the CASPT2 and MRCI methods.

5.3.2 Vertical Excitation Energies

Table 5.3 lists the VEE for the first three singlet excited states for this study and for configuration interaction calculations taken from Grein *et al* [83] and experimental data for excitation to the first excited state taken from Bertin *et al* [79]. The experimental value of 3.99 eV corresponds to the maximum of the absorption band found by Johnston and Bertin which they assigned to the $1^1\mathrm{A}'' \leftarrow X^1A'$ transition. The results from this study all yield lower values for this transition especially the CASSCF with a difference of 1eV.

An analysis of the effect of small changes in the molecular geometry shows how sensitive the VEE are to the bond lengths and bond angle. If the equilibrium geometry from a HF optimisation, table 5.2, is used in a full-valence CASSCF the VEE are 3.74, 6.06 and 6.72 eV for transitions to the $1^1\mathrm{A}''$, $2^1\mathrm{A}''$ and $2^1\mathrm{A}'$ respectively. These results are much closer to the experimental result of 3.99 eV. By taking the geometry used by Schinke *et al* also shown in table 5.2, and calculating the VEE energies in the same way we get 3.68, 5.66 and 6.20 eV. In this study we found the equilibrium bond angle to be 111° whereas the majority of previous studies have found it to be 110°. The same calculation was carried out using the bond lengths obtained in this study but with the bond angle now changed to 110 ° and this was found to have little effect on the outcome with results of 3.0, 4.43 and 4.77 eV.

5.3.3 Dissociation Energy

The dissociation energy for the F-NO bond, calculated at different levels of theory, is shown in table 5.4. Compared with the experimental value, the CASPT2 shows very good agreement but the MRCI and CASSCF underestimate the dissociation energy

Table 5.1: Relative energies (in Hartrees) for the ground and first 3 excited singlet states of FNO calculated in this study at the CASSCF, CASPT2, MS-MR-CASPT2 and MRCI levels and compared with results from CI, MR-CISD and Hartree Fock. Energies are taken relative to the MRCI ground state energy.

	CASSCF	CASPT2	MS-MR-CASPT2	MRCI	CI[a] [83]	MR-CISD[b] [84]	Hartree Fock[c] [81]	Hartree Fock[d] [82]
X^1A'	0.2822	0.0216	0.0216	0.0000	0.4109	0.0054	1.4572	0.7984
$1^1A''$	0.3185	0.1200	0.0928	0.1165	0.5659	0.1643		
$2^1A'$	0.3187	0.1122	0.0933	0.1786	0.6760			
$2^1A''$	0.3188	0.1123	0.0950	0.1704	0.6590			

[a] CI calculations carried out by Grein *et al* using a Whittens double zeta basis set with 19 molecular orbitals for excitations. The confiuration space consists of all single and double excitations with respect to a set of configurations chosen form trial CI calculations.

[b] The reference space for the MR-CISD calculations is made up of the HOMO-LUMO pair of each symmetry with the 3 1s orbitals frozen for the CI.

[c] This study was carried out at the Hartree Fock level using a Gaussian basis.

[d] This study was carried out at the Hartree Fock level using both a minimal and a small extended basis set of contracted Gaussian-type functions.

Table 5.2: Molecular geometries calculated in this study at the HF and CASSCF levels compared with results from CI, MCSCF, Hartree Fock and Experimental.

	HF	CASSCF	CI[a] [86]	MCSCF[b] [84]	Hartree Fock [81]	Hartree Fock [82]	Exp.[c] [87]
r_{NO}(Å)	1.14	1.20	1.14	1.13	1.24	1.14	1.13
r_{NF}(Å)	1.44	1.60	1.47	1.49	1.50	1.47	1.52
$F\hat{N}O$(°)	110	111	110	109.8	109	110	110

[a] Calculations were carried out at the SCF level with a 6-31G basis set.

[b] Calculations were carried out at the MCSCF level using a Huzinaga basis (10s/6p) for all atoms. The active space included the single and double excitations of the four highest occupied and four lowest unoccupied orbitals of A' symmetry and the HOMO-LUMO pair of A'' symmetry.

[c] Microwave data carried out on ^{15}NOF.

Table 5.3: Vertical excitation energies (in eV) for the first 3 singlet excited states calculated in this study at CASSCF, CASPT2, MS-MR-CASPT2 and MRCI levels compared with results from CI data and experimental data.

	CASSCF	CASPT2	MS-MR-CASPT2	MRCI	CI [83]	Exp. [79]
$1^1A''$	2.90	3.20	3.29	3.17	4.22	3.99
$2^1A''$	4.30	4.77	4.86	4.63	6.75	
$2^1A'$	4.63	4.86	4.98	4.86	7.21	

quite significantly, as much as 1.2 eV in the case of CASSCF. The poor performance of the CASSCF was a surprise as a full-valence active space was used which is usually sufficient for reasonable energetics. The failing of the MRCI method can be attributed to the fact that it takes the already inadequate CASSCF wavefunction as a reference and is not able to improve enough to give satisfactory results. The CASSCF wavefunction is also used as reference for the CASPT2 and MS-MR-CASPT2 calculations. The result for the MS-MR-CASPT2 dissociation energy is shown before and after the surfaces had been corrected for a large kink in the curve at large N-F bond distances, (a) and (b) in table 5.4.

Table 5.4: The dissociation energy of FNO (in eV), D(F-NO), calculated at the CASSCF, CASPT2, MS-MR-CASPT2 and MRCI levels compared with experimental results. The two results for MS-MR-CASPT2 refer to the dissociation energy before, (a), and after, (b), the surfaces were smoothed.

CASSCF	CASPT2	MS-MR-CASPT2	MRCI	Exp [88, 89]
1.12	2.39	2.50$^{(a)}$	1.57	2.38
		1.87$^{(b)}$		

5.3.4 Potential Energy Surfaces

1D Surface Cuts along the Dissociation Coordinate

The important features of a PES are the smoothness, the topology and the energetics which must be analysed for accuracy before the surface is used for the dynamics. Using the CASSCF, MS-MR-CASPT2 and MRCI methods and calculating four 3D PES one accumulates a large amount of data to scrutinise for its accuracy. By plotting 1D cuts along the dissociation coordinate, r_2, with θ held at the equilibrium binding angle 111° and r_1 at 1.2Å, it was possible to compare the different *ab initio* methods side by side.

Figure 5.5 shows cuts along the dissociation coordinate, r_2, at the CASSCF, CASPT2 and MRCI levels of calculation for the ground and lowest 3 singlet excited states. From these plots it becomes apparent that the MS-MR-CASPT2 method becomes unstable at large N-F bond distances with a sudden jump in energy at $r_2 = 3.0$Å producing curves that are not smooth. The MRCI curves are smooth but it appears that the ground state is curving sharply upwards in energy and that it wants to mix with some higher state that has not been included in the calculation. The CASSCF results show the smoothest curves but as we have discovered they are energetically incorrect. It can clearly be seen from this plot that the dissociation energy of the CASSCF is significantly under estimated.

The next step was to see if any excited states higher in energy were mixing in with these 4 states and to see if by including extra states the curves could be smoothed out. The same calculations along this cut were carried out for 6 states, 3 of A$'$ symmetry and 3 of A$''$ symmetry. These results are shown in figure 5.6. The addition of these extra states has failed to get rid of the kink in the MS-MR-CASPT2 curves but the MRCI is smooth now that there is the mixing in of these other states, with all six degenerate at dissociation. The CASSCF curves are still smooth and now the four lowest states are degenerate at dissociation with the two extra states higher in energy. Adding these extra states, however, does not alter the energetics of the curves significantly and the

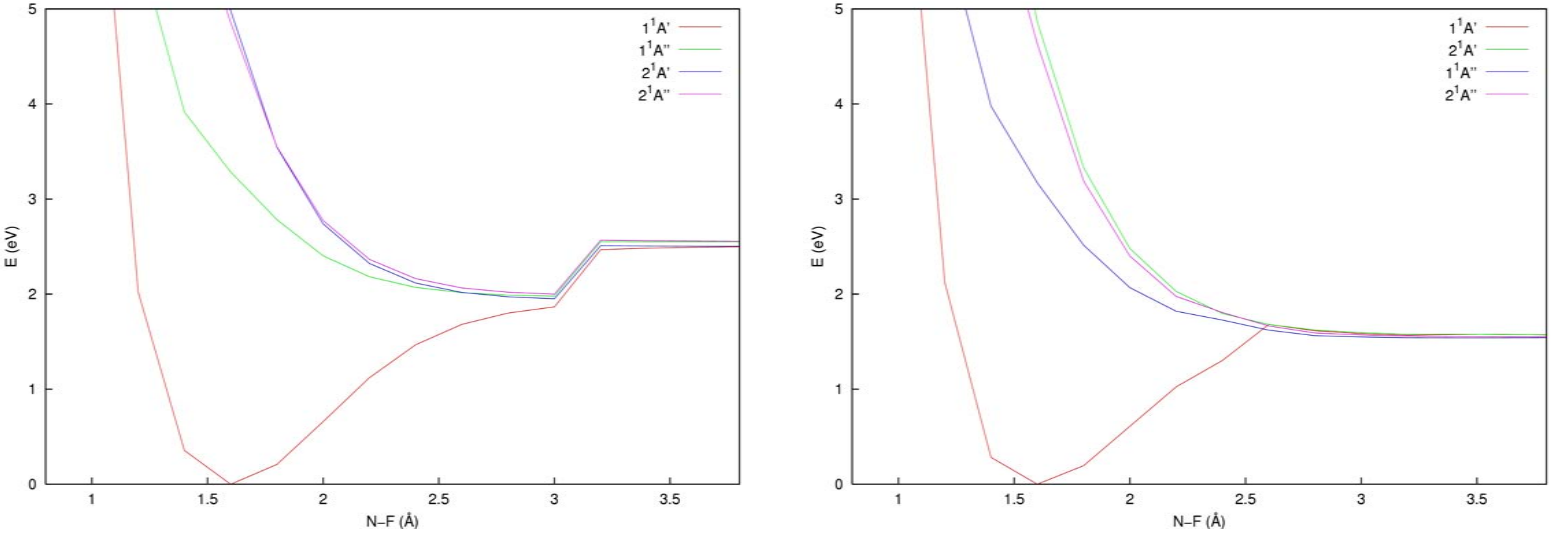

(a) MS-MR-CASPT2

(b) MRCI

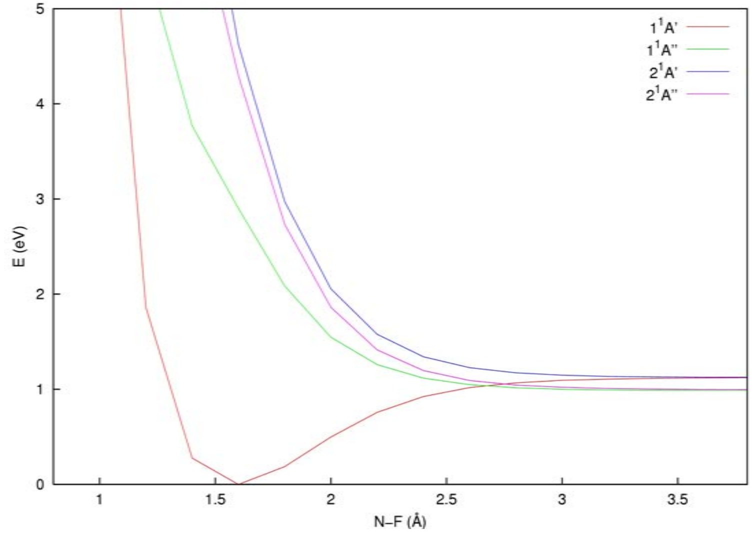

(c) CASSCF

Fig. 5.5: 1D Cut along the N-F bond of the first 4 singlet excited states calculated at the CASSCF, MRCI and CASPT2 levels, θ=111° and N-O = 1.2Å.

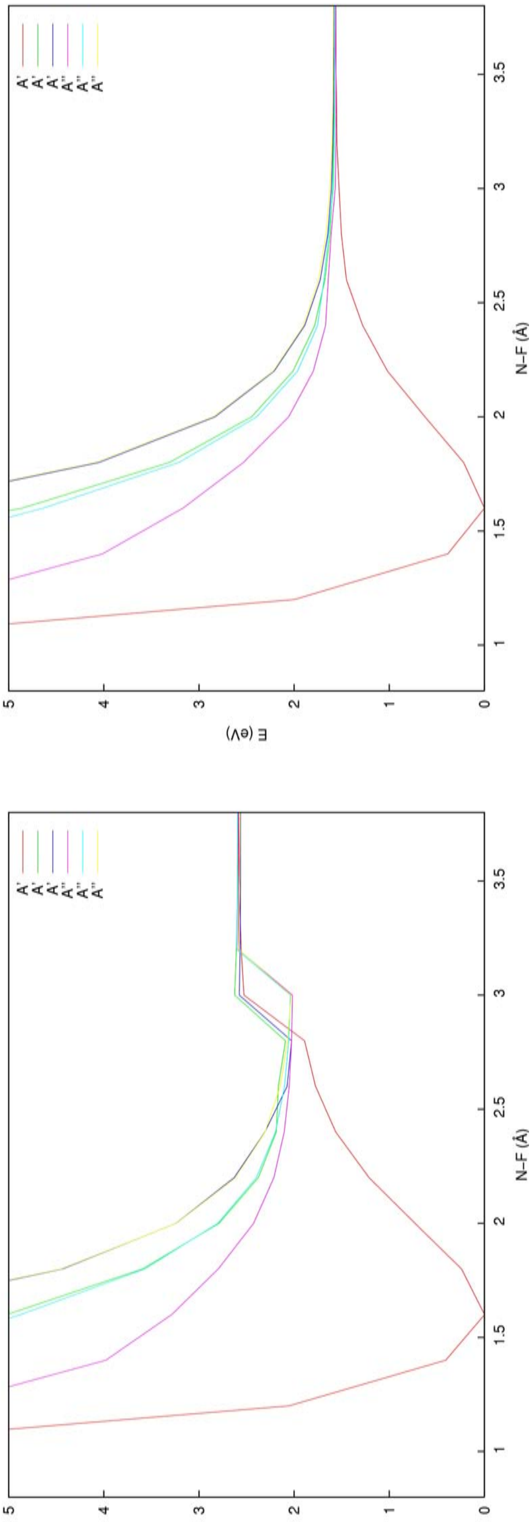

(a) MS-MR-CASPT2

(b) MRCI

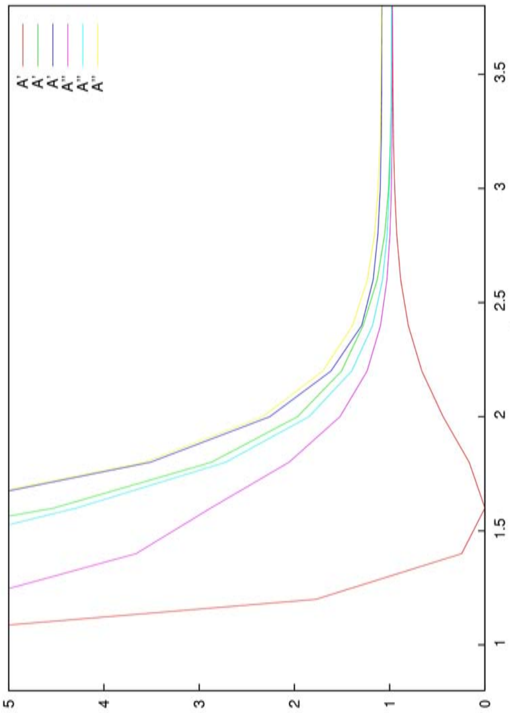

(c) CASSCF

Fig. 5.6: 1D Cut along the N-F bond of the first 6 singlet excited states calculated at the CASSCF, MRCI and CASPT2 levels, θ=111° and N-O = 1.2Å.

kink in the MS-MR-CASPT2 curves at extended NF bond lengths cannot be smoothed out by adding these extra states.

To be absolutely sure that there was no mixing in from any other states the same calculation was carried out at the CASSCF level but with 10 states of each symmetry giving a total of 20 states including the ground state. These results are shown in figure 5.7 and after the 6 lowest states it can be seen that there is a very large energy gap of about 6 eV before any other excited states appear, confirming that it can only be the mixing in of the 2 extra states to the lowest 4 which contribute to the smoothing out of the MRCI curves in figure 5.5 when only the lowest 4 were included. From these results it is clear that the *ab initio* PES have inaccuracies and cannot be used for the dynamics unless some adjustments are made to them.

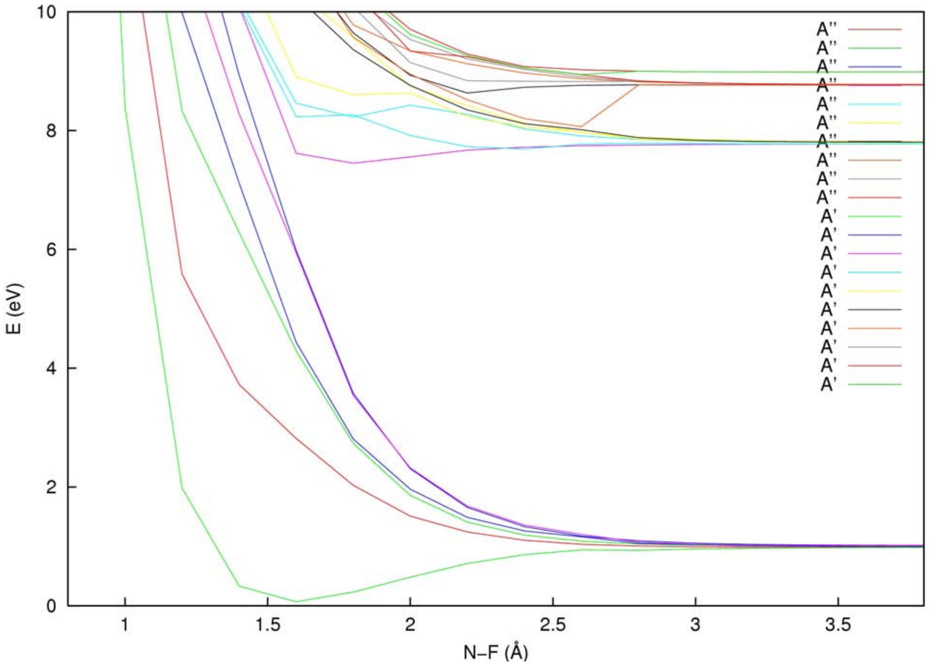

Fig. 5.7: 1D cut along the N-F bond of lowest 20 singlet excited states calculated at the CASSCF level, theta=111°.

CASSCF Adiabatic Potential Energy Surfaces

Contour plots of the ground and first 3 singlet excited states calculated at the CASSCF level are shown in figure 5.8 along NO and NF with θ held at the equilibrium value of

111°. Although energetically inaccurate these PES are smooth and illustrate clearly the features of two channels along NO and NF. Around the ground state minimum the contours show the very steep walls of the surface along the dissociative N-F channel. The S_0 state shows a very deep minimum at N-O = 2.1 au and N-F = 3.5 au whereas the

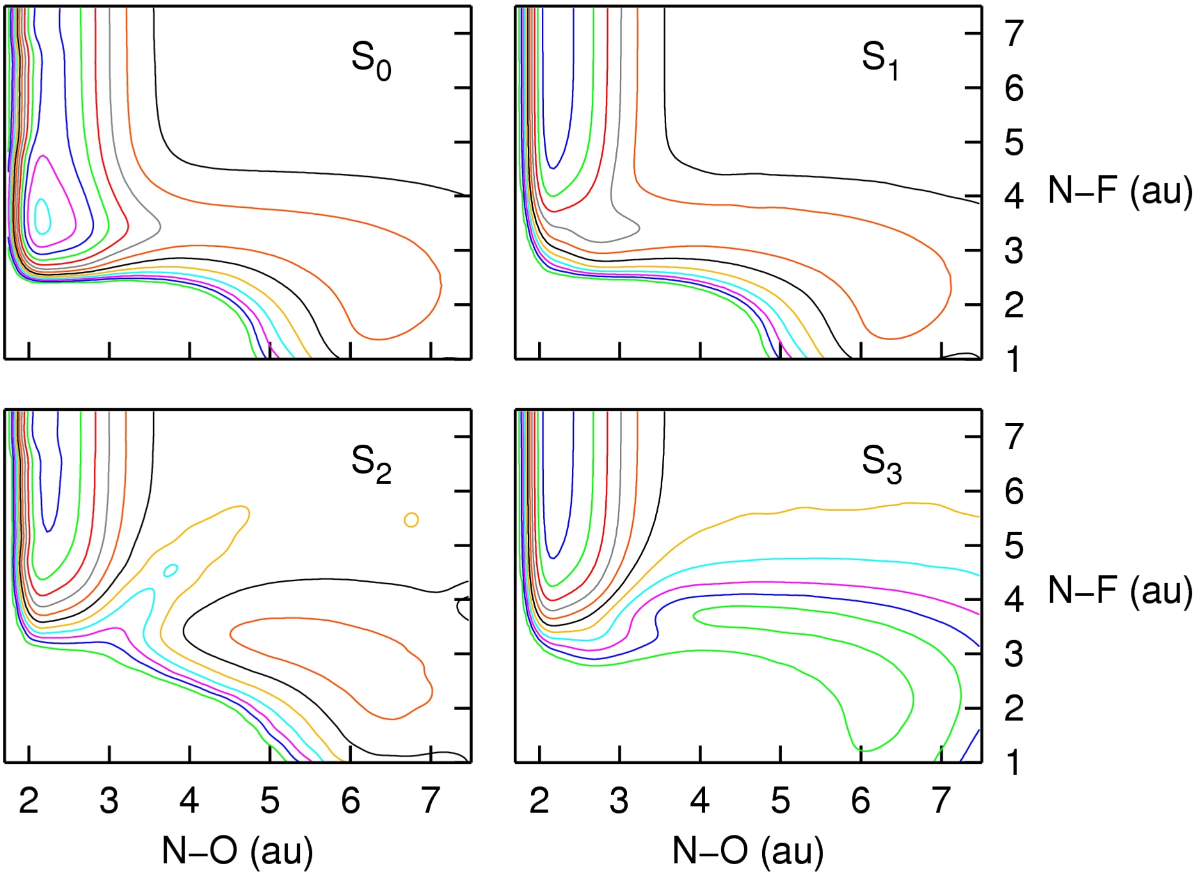

Fig. 5.8: Contour plots of the ground and first 3 singlet excited states of FNO calculated at the CASSCF level along NF and NO with θ fixed at the equilibrium value of 111°.

S_1 state has no minimum but exhibits an interesting shoulder along the NO channel. S_2 is of A' symmetry unlike the other surfaces which are A'' and we see that there is a break down the middle with the two channels being separated by a barrier.

5.3.5 Initial 3D Absorption Spectrum

Taking the MS-MR-CASPT2 *ab initio* surfaces, the kink along N-F was smoothed out and the 3D absorption spectrum was calculated. The adjustment of these surfaces was achieved by holding the angle at fixed values and plotting along r_1 and r_2 and adjusting the values for the potential energy by hand to produce smooth curves.

All dynamics are carried out in Jacobi coordinates R, r and γ. After relaxation of the wavepacket on the ground state and excitation to the excited S_1 state the initial position was $R = 3.64$ au, $r = 2.14$ au and $\gamma = 2.22$ rad. The absorption spectrum is shown in figure 5.9. The spectrum is extremely broad with very little fine structure.

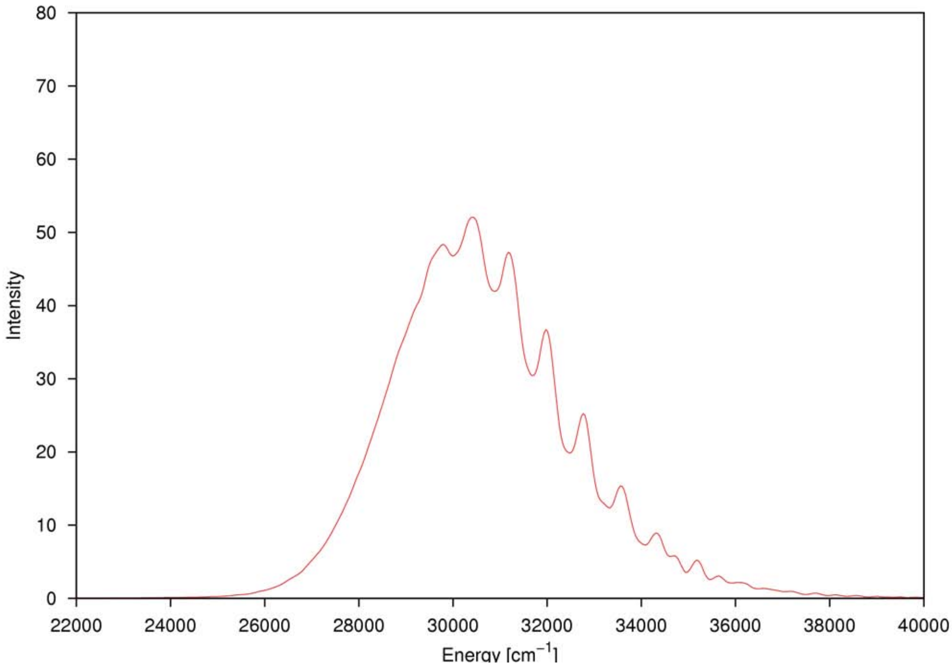

Fig. 5.9: 3D absorption spectrum for FNO after relaxation on the ground state and propagation to the MS-MR-CASPT2 $1^1A''$ excited state.

The broad background is attributed to a rapidly dissociating portion of the wavepacket down the N-F channel. The dynamics show that the wavepacket begins immediately to move along the dissociative channel and within 24 fs it has progressed far along the exit channel. The main progression that is mildly present in this spectrum is due to the N-O excitation. We observe nothing of the second progression from the periodic motion of the wavepacket as it progresses along the N-F channel. These results indicate that a very large portion of the wavepacket is dissociating along N-F with very little of it oscillating within the N-O channel and that dissociation is occurring at such a rapid rate that the periodic motion along N-F is lost. Although some of the features are present within this spectrum it is far from being representative of the experimental example and indicates clearly the limitations of using PES directly from the *ab initio* data.

5.3.6 2D MS-MR-CASPT2 Dynamics and Absorption Spectrum

After failing to reproduce the experimental spectrum by relaxing on the ground state and exciting to the upper state for propagation we now carry out dynamics on the S_1 surface with the angle held fixed at 2.24 rad and place the wavepacket on this surface at various starting positions. Here we look to the work by Schinke *et al* where the angle was also held fixed and the wavepacket was placed on the excited state rather than excited after relaxation. By eliminating the effect of the angular DOF and by having control over the initial position of the wavepacket we can explore the topology of the *ab initio* surfaces further.

A more detailed contour plot of the S_1 PES is shown in figure 5.10. The two channels along the dissociative coordinate, r_2, and the vibrational coordinate, r_1, are well defined with the topology along r_2 showing the narrow and steep sided channel. We also see the presence of the small well along the NF channel. In the study by Schinke he reports that a small portion of the wavepacket becomes trapped in this shallow minimum.

Shown on the surface are the four starting points, a, b, c and d, for the wavepacket. A very large number of calculations were carried out on this surface by placing the wavepacket at various positions and here we show the most interesting results. It should be noted that none of the starting positions shown here correspond to the

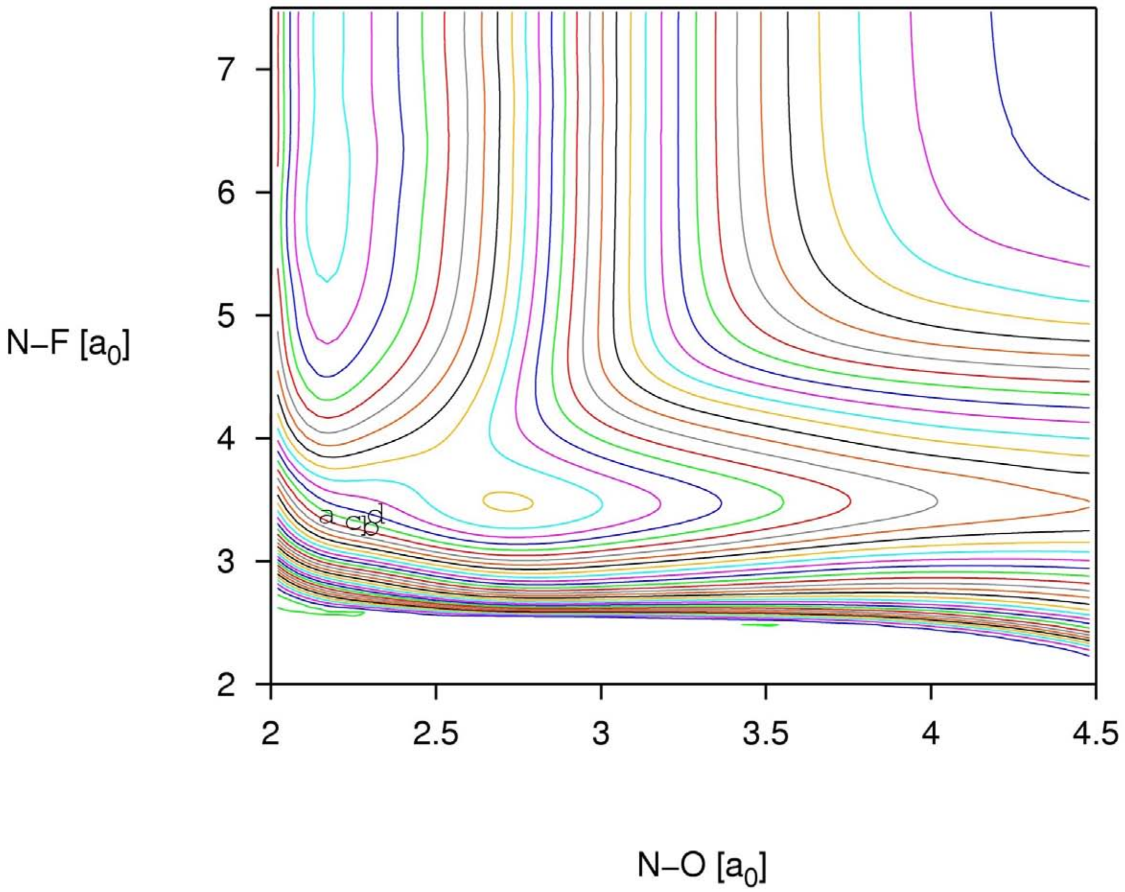

Fig. 5.10: MS-MR-CASPT2 $1^1A''$ excited state contour plot along R and r with γ held at the Jacobi angle of 2.24 rad. For the dynamics the wavepacket was placed on this surface at the initial positions a, b, c and d.

one for the relaxation calculation used in the previous calculation because it does not produce satisfactory results. The spectra generated from four of these propagations are shown in figure 5.11.

Spectrum ‘a’ exhibits a very broad background which is attributed to a large portion of the wavepacket dissociating very rapidly, 12 fs, along R. The starting point for this wavepacket at $R = 3.4$ and $r = 2.14$ au is directly in line with the R channel and up the steep part of the surface initiating fast propagation straight along R. A portion of the wavepacket does move along the N-O channel giving a small amount of fine structure and we notice the presence of the second progression, due to the periodic motion of the wavepacket along R, beginning to appear.

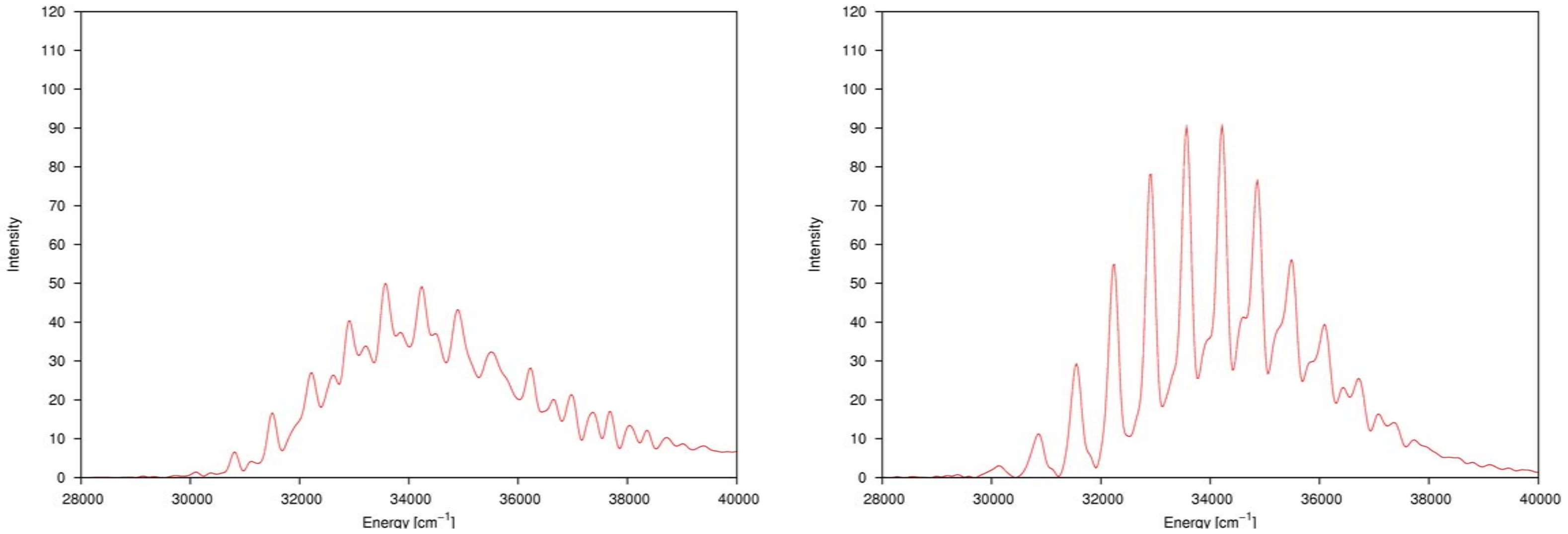

(a) R = 3.4, r = 2.14 au

(b) R = 3.3, r = 2.27 au

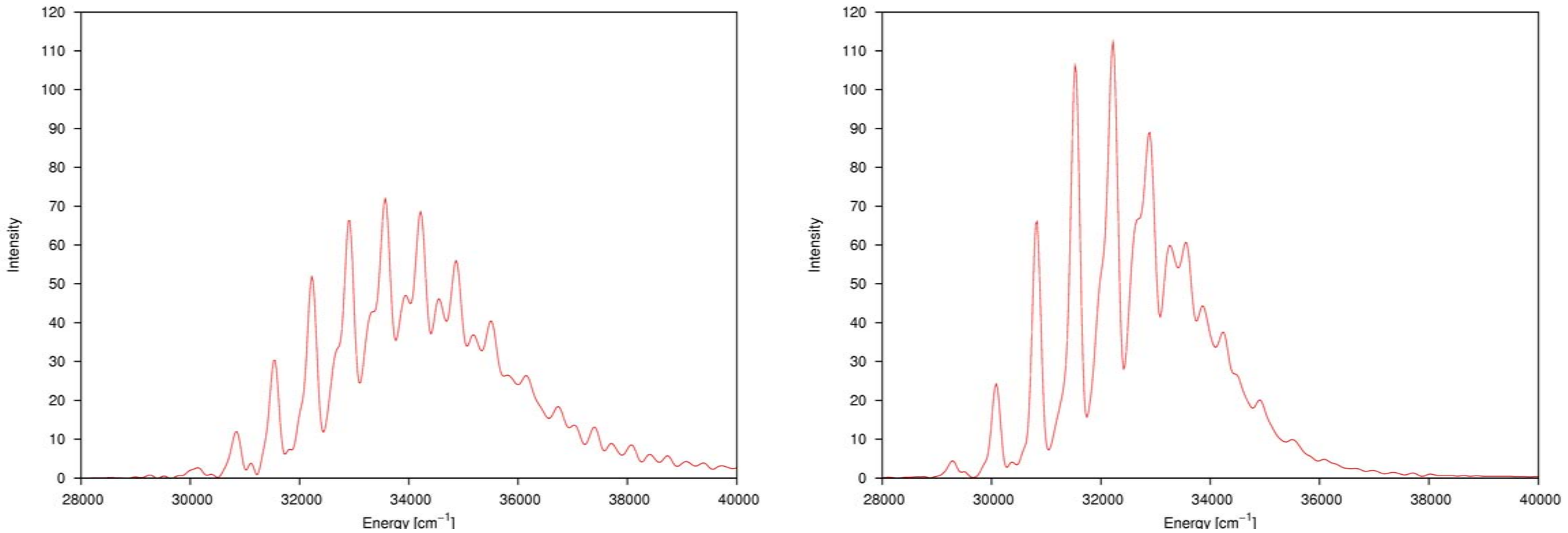

(c) R = 3.35, r_v = 2.22 au

(d) R = 3.4, r = 2.29 au

Fig. 5.11: 2D absorption spectra calculated by placing the initial wavepacket at various positions in R and r with γ held at the Jacobi angle of 2.24 rad.

The starting point for spectrum 'b' is displaced relative to 'a' along R by just 0.1 au to 3.3 and along r by 0.13 au to 2.27. This does not alter the gradient of the surface at R but moves the wavepacket further along r. The result of this adjustment is that significantly more of the wavepacket is propagated along r producing a spectrum with more structure due to the N-O vibration. We can also see the emergence of the second progression due to the N-F stretch but there is still not enough of this present.

At 'c' the wavepacket is given a starting position of $R = 3.35$ and $r = 2.22$ au. This positioning is in between that of 'a' and 'b' to try and achieve a less rapid dissociation along R and slightly less rapid propagation along r. The spectrum, 'c', shows that there is more of this oscillation that occurs along the N-F channel but that dissociation is still too rapid.

To try to induce slower dissociation, spectrum 'd' has a wavepacket that starts further into the r channel at $R = 3.4$ and $r = 2.29$ au. Spectrum 'd' now exhibits a large amount of structure due to the N-O vibration as a consequence of starting further along that channel and we lose some of the N-F progression.

It is from the initial position 'b' that the best spectrum is obtained in terms of the presence of the two progressions.

The correlation functions for the four spectra are shown in figure 5.12. All of the correlation functions show a rapid decay to zero (within 12 fs). For 'a' we see only small recurrences of the wavepacket, a clear indication that a large portion of the wavepacket dissociated along NF very rapidly, hence the broad background in the spectrum. For 'b', 'c' and 'd', starting further down the r channel has resulted in a smaller amount of the wavepacket dissociating and we see much larger recurrences. This is reflected in the spectra which have much more structure due to the NO excitation. We see a recurrence time of $\sim$ 50 fs which gives rise to the frequency of $\sim$ 650 cm^{-1} in the spectra due to the NO excitation. This is underestimated compared with the experimental value of 1045 cm^{-1}. A second period is present in the autocorrelation functions and this is

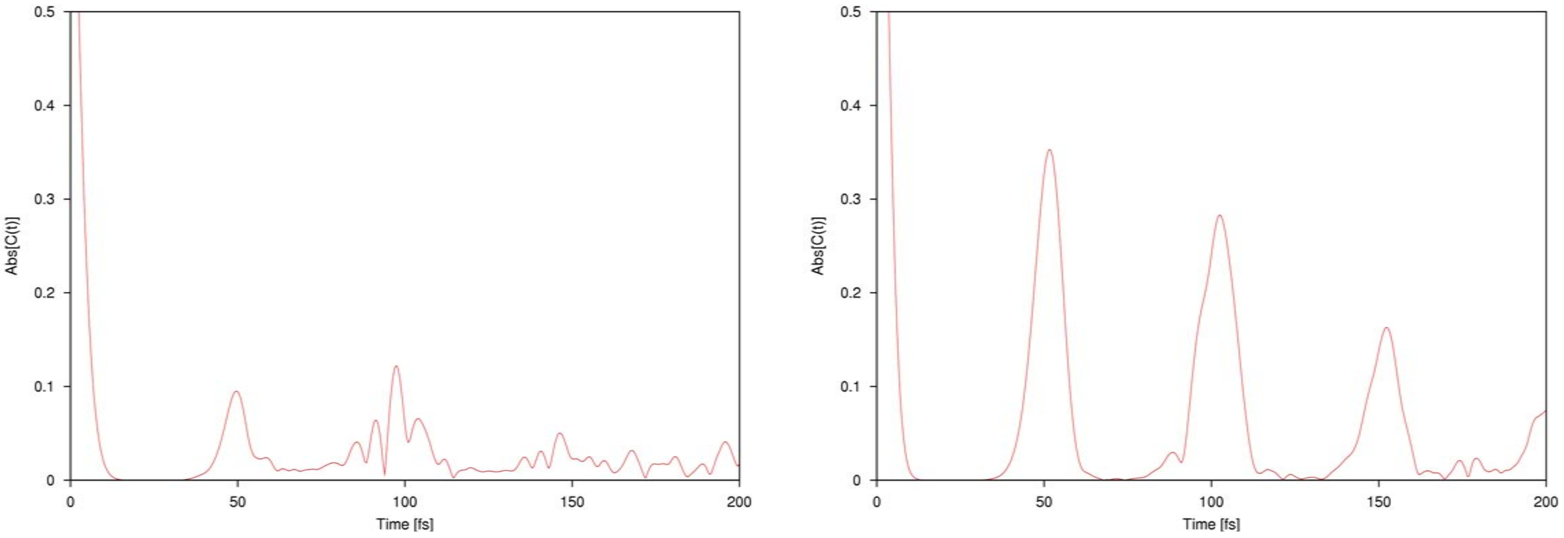

(a) R = 3.4, $r = 2.14$ au

(b) $R = 3.3$, $r = 2.27$ au

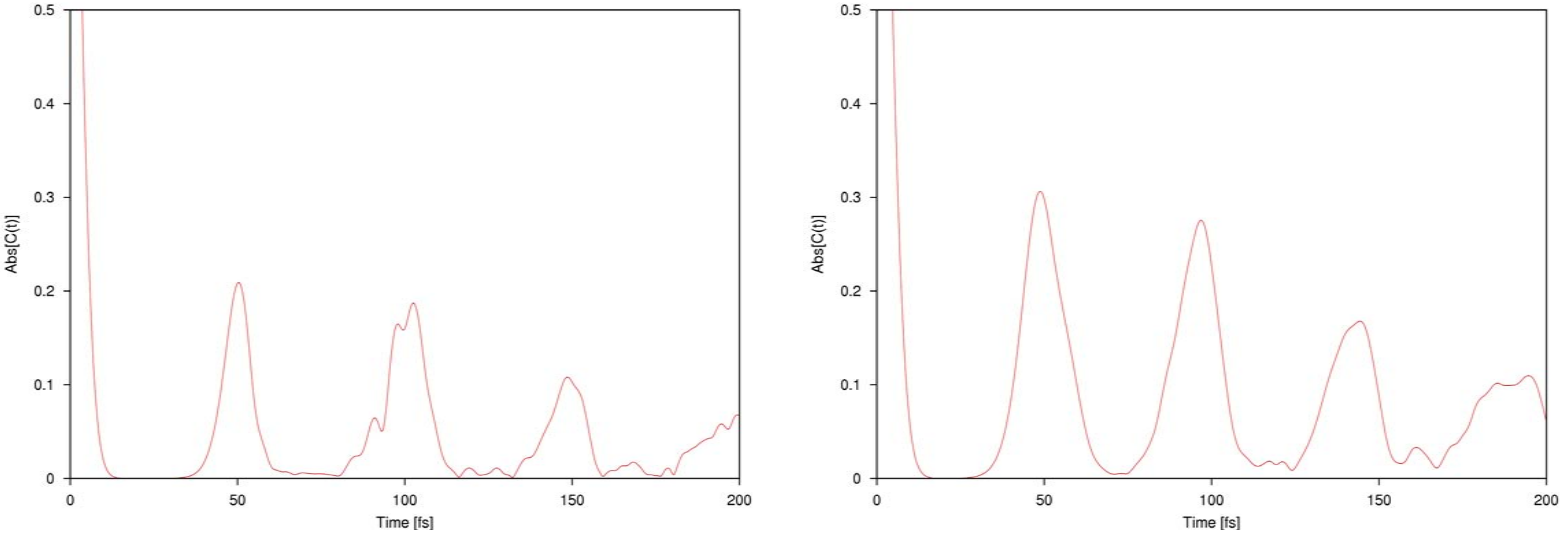

(c) $R = 3.35$, $r = 2.22$ au

(d) $R = 3.4$, $r = 2.29$ au

Fig. 5.12: Correlation functions for the 2D dynamics from propagation of a wavepacket from various initial positions in R and r with γ held at the Jacobi angle of 2.24 rad.

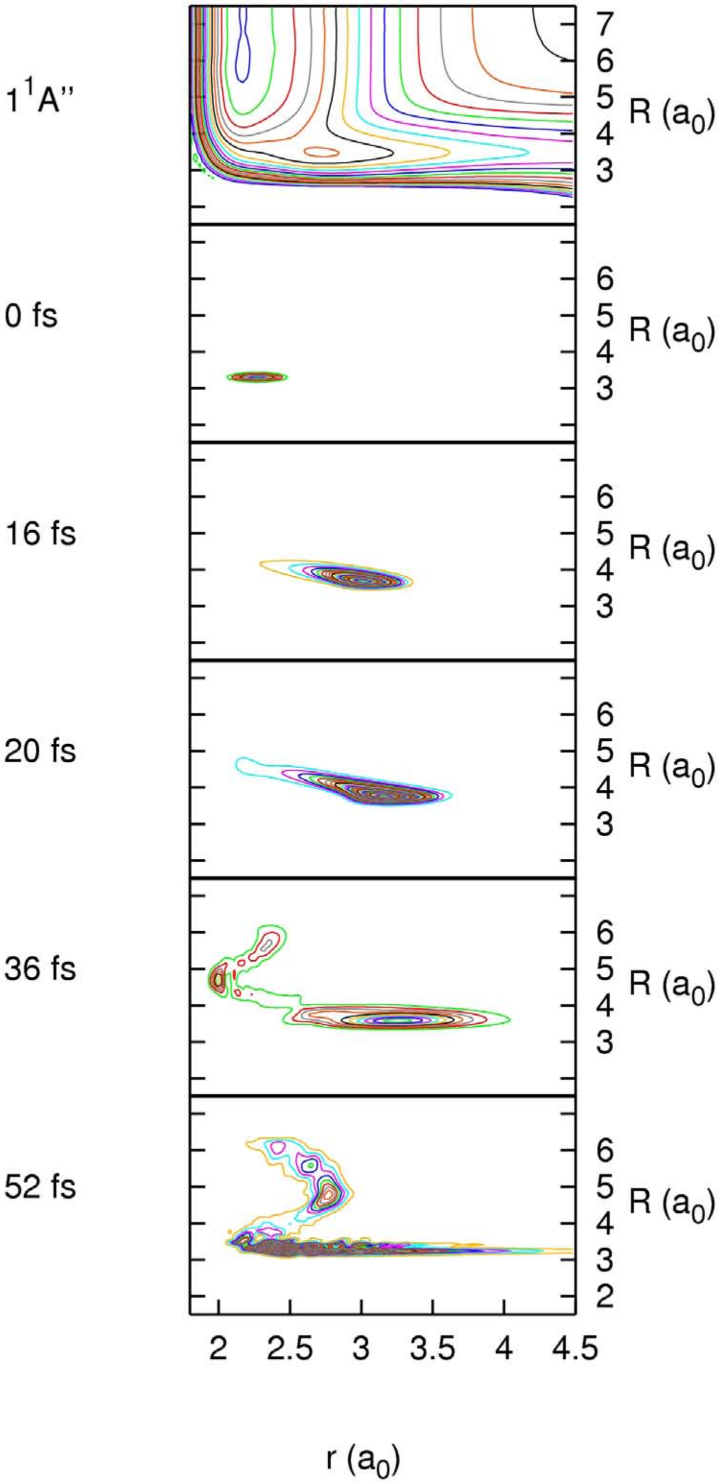

Fig. 5.13: Snapshots of the 2D wavepacket dynamics on the MS-MR-CASPT2 $1^1A''$ excited state at 0, 16, 20, 32 and 36 fs. The wavepacket was given an initial starting position of $R = 3.3$, $r = 2.27$ au with γ fixed at 2.24 rad.

related to the periodic motion of the wavepacket along the NF channel.

The wavepacket dynamics that produced spectrum (b) are shown in figure 5.13 with the PES shown at the top. The initial starting position is at $R = 3.3$, $r = 2.27$ au. After 16 fs it can be seen that the main part of the wavepacket is moving along the N-O channel and by 20 fs just a small part has begun to extend down the N-F channel. After 36 fs we see that from this initial starting point the bulk of the wavepacket is extending along the N-O channel giving rise to the main progression that can be seen in spectrum (b). There is a small portion propagating along the N-F channel and a periodic oscillation can be seen which gives rise to the second progression in the spectrum. The recurrence responsible for the main progression in the spectrum can be seen at 52 fs.

These results show just how sensitive the system is to a small change in the initial position of the wavepacket due to the steepness of the PES particularly along the dissociative N-F channel. It is, therefore, not surprising that by generating PES with *ab initio* methods where inaccuracies are common that the spectrum is highly affected. Even keeping the angle fixed and taking a 2D surface we are not able to reproduce the experimental spectrum with our MS-MR-CASPT2 surfaces.

5.3.7 3D MS-MR-CASPT2 Adiabatic Spectrum

Again we calculate the spectra but with the inclusion of the angular DOF, γ. The wavepacket has been placed on the excited state in the same way as for the 2D examples with the initial angle given as 2.24 rad, section 5.3.6. The 3D spectra are shown in figure 5.14. Comparing these spectra with the 2D ones the most obvious difference is the broader background that we see as a result of including the angle. There is also a notable loss of fine structure from the N-O excitation and the N-F progression has been lost completely. It is known that there is strong coupling between the motion in R and γ and so when the angular DOF is included these two motions cannot be treated separately. We find that after 200 fs of propagation, the Jacobi angle is reduced to 1.4

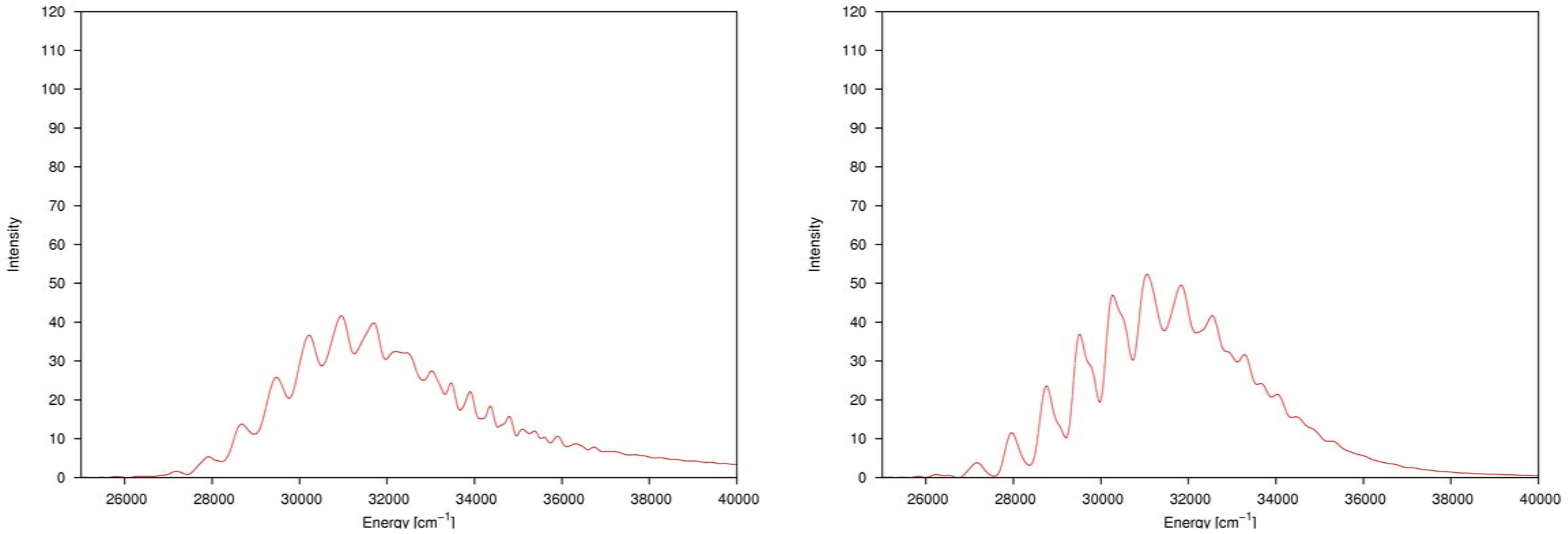

(a) R = 3.4, r = 2.14 au (b) R = 3.3, r = 2.27 au

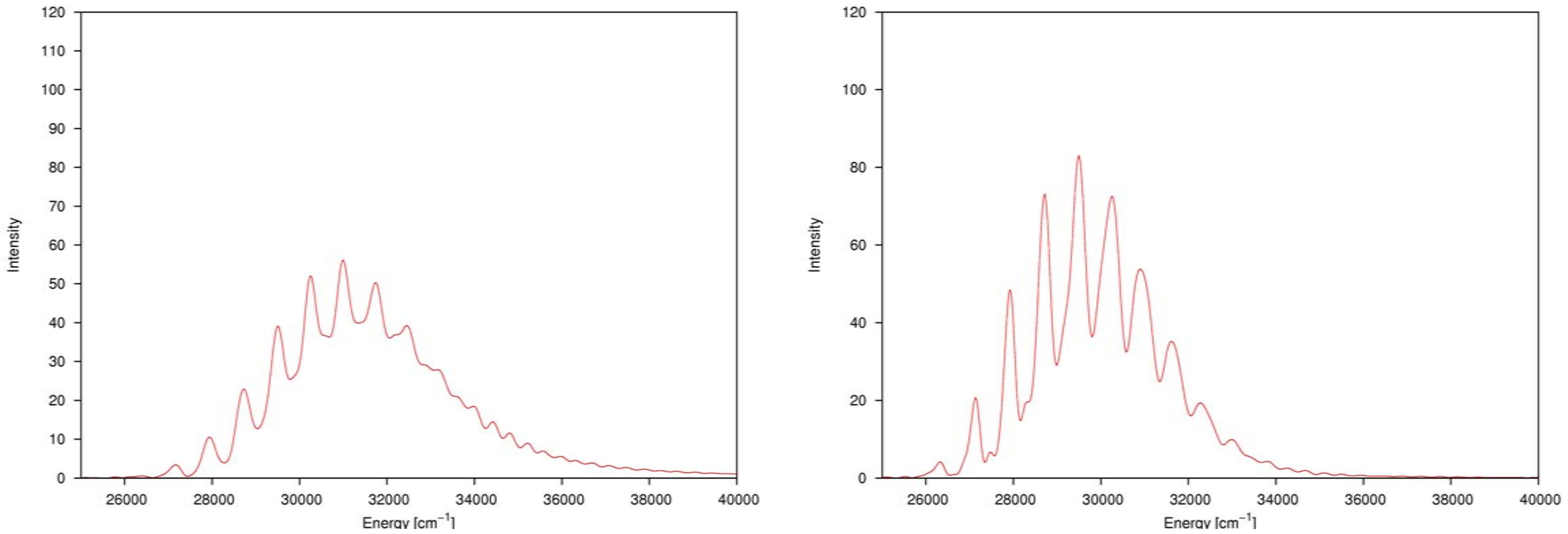

(c) R = 3.35, r = 2.22 au (d) R = 3.4, r = 2.29 au

Fig. 5.14: 3D absorption spectra calculated by placing the initial wavepacket at various positions in R and r with γ held at the Jacobi angle of 2.24 rad.

radians. We find that spectrum ‘d’ is now the better of the four whereas for the 2D dynamics, it was spectrum ‘b’. The effect of including the angle on spectrum ‘b’ has been a substantial loss of the progression due to the NO stretch but on ‘d’ we see that the effect has not been quite so dramatic and that this progression has been better maintained.

5.4 Conclusions

Using *ab initio* methods to generate PES has formed the major part of this study on the photodissociation of FNO. Such a thorough study of these surfaces has not been carried out before. Three different methods were used to calculate the surfaces and we have been able to assess each method in terms of its merits and its limitations in the context of this system. The CASSCF method where dynamic electron correlation is not accounted for has failed to yield satisfactory results in terms of the energetics but the surfaces are smooth and continuous all the way up to extended NO and NF bond distances. CASSCF underestimates the F-NO dissociation energy and the VEE for S_1 quite significantly considering that a full valence active space was used.

The MS-MR-CASPT2 and MRCI calculations yield better results for the VEE but again underestimate the dissociation energy. When plotting 2D cuts along N-F for the ground and lowest 3 excited states we found that the MR-CASPT2 method struggled at extended N-F bond distances and the surfaces showed a sharp jump in energy and that the MRCI ground state curve was curving sharply upwards in energy as if there was mixing from higher states. We found that allowing mixing from 2 extra states smoothed the MRCI curves but did not improve the MS-MR-CASPT2 curves.

The initial wavepacket propagations on the 3D surfaces, after relaxation on the ground state, showed rapid dissociation and as a result of this the spectrum was broad with little structure. We then removed the angular DOF by holding γ at a fixed value and then placed the wavepacket at various initial positions on the S_1 surface. This was then repeated with the inclusion of the angle.

In trying to generate the spectrum we found that the steep walls of the surfaces make the spectrum extremely sensitive to the starting position of the wavepacket. If the wavepacket is positioned along the dissociative channel it is liable to undergo rapid dissociation giving the spectrum an extremely broad background. If the wavepacket is positioned further along the vibrational N-O channel some fine structure is achieved from the N-O stretch but at the cost of the second progression from the oscillation along NF. We found that the inclusion of the angle increased the broad background of the spectrum and although we did replicate certain features of the spectrum we were unable to reproduce it exactly. We conclude that in the work by Schinke *et al*, where they were successful in reproducing the experimental spectrum, that this was achieved because they did not include the angular DOF thus their representation of the system was more simplified than the one in this study.

The main progression in the spectrum is due to a small portion of the wavepacket becoming trapped in a shallow well along the NO channel. A detailed analysis of the MS-MR-CASPT2 surfaces revealed that this well was present. We conclude that we have been successful in reproducing the topology of the S_1 excited state with a good level of accuracy and that this is manifest in the fine structure in our spectrum. However it is clear that the depth of this well in the S_1 state is not large enough to trap the wavepacket enough to reproduce the experimental spectrum.

We can conclude from these results that generating the surfaces for the dynamics is an extremely arduous task and we have illustrated the limitations and merits encountered with the different *ab initio* methods.

Chapter 6

Nitrosyl Fluoride Model Hamiltonian

6.1 Introduction

In the previous chapter extensive *ab initio* calculations were carried out to generate PES for the photodissociation dynamics of FNO. In carrying out wavepacket dynamics on these surfaces we failed to reproduce the experimental absorption spectrum with a high level of accuracy although we did reproduce some of the main features. The topology of the FNO $1^1A''$ state is of special interest in this case. It exhibits steep sides along the N-F channel and a shallow well in the N-O channel in which a small portion of the wavepacket becomes trapped and gives rise to the main progression in the spectrum. After using several different *ab initio* techniques to calculate the surfaces we find that the system is extremely sensitive to these methods. An accurate surface for FNO must exhibit the main features which give rise to the spectrum. The fact that these features are so subtle and so sensitive makes the FNO surfaces very difficult to generate with *ab initio* methods.

Although *ab initio* techniques make it possible to generate all regions of the PES, from equilibrium geometries to extended bond lengths, they do not always offer the required level of accuracy over the whole surface. This is especially the case when there is coupling between electronic states and they become close in energy or degenerate.

The next step in this study is to carry out a potential fit of the *ab initio* MS-MR-

CASPT2 data. The principle behind this technique is to choose a suitable function which has the characteristics of the PES and then to use a least squares method to fit the function to the data points. The function is then optimised by adjusting the parameters until the system shows agreement with known experimental data. Surface fitting is by no means a straight forward procedure but has been used with great success for small systems such as H + H_2 [90] and He + H_2^+ [91, 92]. For H + H_2 an accurate least squares fit was made to *ab initio* data from Liu and Siegbahn [93] calculated at the configuration interaction level and subsequent work using this surface has revealed much detailed information on this systems' dynamics.

Previous calculations in our study on FNO have involved excitation and propagation on the S_1 excited state only. What we will now develop is the theory that the S_1 state is coupled to one or more of the higher excited states of A$''$ symmetry. We will investigate how the coupling changes the topology of the S_1 surface and whether the shallow well, which plays such an important role in the dynamics, develops as a consequence of the coupling.

6.2 Selecting the Relevant Electronic States

Firstly we need to know which states, as well as the ground and $1^1A''$ excited state, will be included in the fit. Coupling occurs through states of the same symmetry so we focus our interest on the $^1A''$ states.

Using Molpro 2006 the lowest 18 singlet excited states, 9 each of A$'$ and A$''$ symmetry, were calculated in binding coordinates at the CASSCF level with a full valence active space. The potential energy curves were calculated along the two bonds, NO and NF, and the bond angle, θ, moving away from the equilibrium geometry $r_{NO} = 1.2$ au, $r_{NF} = 1.6$ au and $\theta = 111°$. Along the bonds, energies were calculated every 0.2 Å from 0.8 to 3.0 Å and for the angle every 6° from -1 to 176°. The 1D plots are shown in figure 6.1. The cut along θ, figure 6.1(a), was calculated for values up to 176° as

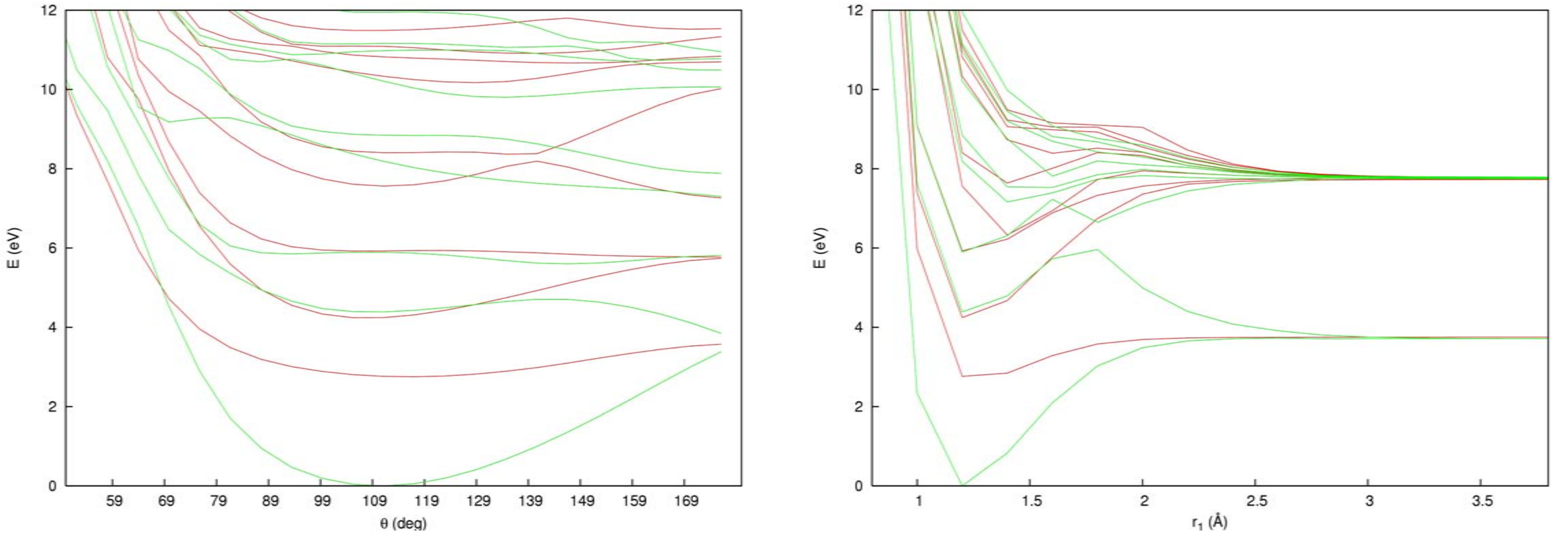

(a) θ

(b) NO

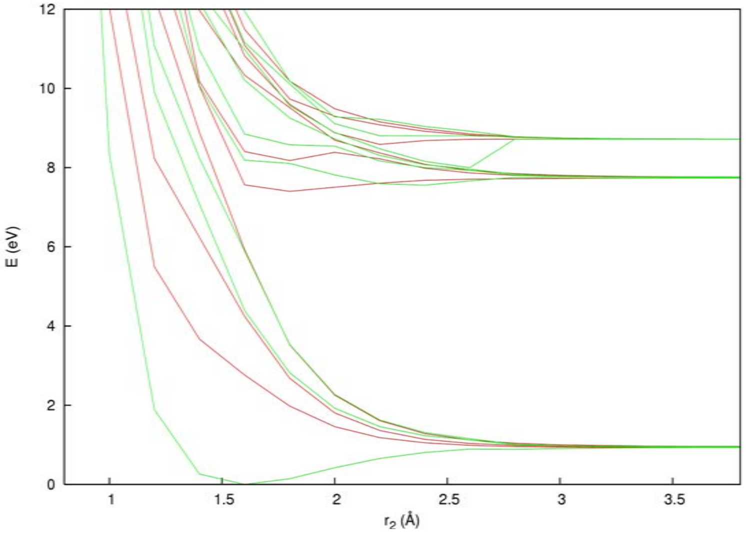

(c) NF

Fig. 6.1: 1D cuts along θ, NO and NF of the lowest 18 singlet excited states calculated at the CASSCF level. The states with A$'$ symmetry are shown in green and the A$''$ states in red.

no convergence could be found at 180°. Looking at figures 6.1(b) and 6.1(c) along NO and NF we see that the $4^1A''$ state comes sharply downwards in energy which indicates there could be some mixing in of this state with the lower ones.

The 1D plots of all 18 states give a picture of the density of states and where coupling may be present between the states. From these plots it is clear that to describe the first excited state we need to consider coupling between the lowest 4 excited states of A″ symmetry. The non-adiabatic coupling between the ground state and the four lowest states of A″ symmetry has been calculated using Molpro 2006 and is shown in table 6.1. The results show that the coupling between the excited A″ states occurs through the in plane vibrational modes which all have A′ symmetry and that coupling between states with different symmetry occurs through the out of plane rotational motion. These results show that coupling exists between all of these states but that the coupling is weak for the $3^1A''$ state. Of most significance for the adiabatic S_1 state is the strong coupling between the $4^1A''$ and $1^1A''$ states. The states we are interested in, therefore, are the first, second and fourth $^1A''$ states. The VEE for these states are shown in table 6.2.

Table 6.1: Non-adiabatic coupling strengths between the lowest four excited states of A″ symmetry and between the ground state with the $1^1A''$ state. Values are in hartree/bohr.

Electronic states	dE/dx	dE/dy	dE/dz
$1^1A'$ and $1^1A''$		0.9696	
$1^1A''$ and $2^1A''$	0.3236		0.4000
$1^1A''$ and $3^1A''$	0.0572		0.0360
$2^1A''$ and $3^1A''$	0.0153		0.0143
$1^1A''$ and $4^1A''$	0.3740		1.0256
$2^1A''$ and $4^1A''$	0.9666		0.8545
$3^1A''$ and $4^1A''$	0.0666		0.0129

In the following we will set up three Hamiltonian models. One for the ground state, one for the S_1 surface as an uncoupled state and one for the S_1 surface as part of a

Table 6.2: Energies (in eV) of the first, second and fourth singlet excited states of A″ symmetry. The CASSCF and MS-MR-CASPT2 results are taken from this study.

State	CASSCF[a]	MS-MR-CASPT2[b]	Exp. [79]
$1^1A''$	2.90	3.29	3.99
$2^1A''$	4.30	4.86	
$4^1A''$	7.80	7.60	

[a] Full valence SA-CAS with a Huzinaga (10s/6p) basis set.
[b] The full valence CAS space was used as a reference for the MS-MR-CASPT2 calculations.

coupled manifold of 3 states - the $1^1A''$, $2^1A''$ and $4^1A''$.

6.3 The FNO Vibronic Coupling Model Hamiltonian

The vibronic coupling model described in section 2.6, has been set up for FNO. The model with coupled states includes three electronic states and the Hamiltonian is represented as a 3 x 3 matrix, **H**. The on-diagonal matrix elements are the diabatic PES and the off-diagonal elements are the couplings between the three states. To recap in the diabatic basis the Hamiltonian is written as the sum of a zero order Hamiltonian and a set of coupling matrices, **W**

$$\mathbf{H} = \mathbf{H}_0 + \mathbf{W}^{(0)} + \mathbf{W}^{(1)} + \cdots \tag{6.1}$$

where $\mathbf{H}_0 = T + \mathbf{V}_0$. The zero-order PES is written

$$V_0 = \sum_{i=1}^{3} v_i \tag{6.2}$$

where v_i are the analytical functions which are fitted to the *ab initio* data along the 3 modes, the NO and NF bonds and the bending angle θ. For the ground state, v_i are all Morse functions which take the form

$$v_i = D_i(\exp(-\alpha(x_i - x_{i0})) - 1)^2 + E_{i0} \tag{6.3}$$

where D_i is the dissociation energy (depth parameter), $x_i - x_{i0}$ is the displacement from the equilibrium bond distance, α_i is a constant which controls the width of the potential and E_{i0} is an energy shift parameter.

For the uncoupled fit of the $1^1A''$ excited state, Morse functions were used for the NO and θ modes and for NF an exponential function was used. This takes the form

$$V_{NF} = E_0(\exp(-A(x - x_0)) - 1) \tag{6.4}$$

where $x - x_0$ is the displacement from the equilibrium bond distance, A is a steepness parameter and E_0 again providing an energy shift.

The fit which includes all three excited states and the coupling between them is represented by a 3 x 3 matrix. The zero-order potentials are now

$$\begin{aligned} V_0^1 &= \sum_i v_i^{(1)} \\ V_0^2 &= \sum_i v_i^{(2)} \\ V_0^3 &= \sum_i v_i^{(3)} \end{aligned} \tag{6.5}$$

where i indicates the mode. v_i for the $1^1A''$ state are all Morse functions. For the $2^1A''$ and $4^1A''$ states the NO and angular modes are Morse functions but the NF mode is represented by an exponential function. The reason for these choices will become apparent later.

The matrix $\mathbf{W}^{(0)}$ is usually diagonal and contains the VEE of the diabatic states. For the coupled-state model it is also required to add to this term $\mathbf{W}_{13}^{(0)}$. It should be noted that matrix subscripts 1, 2 and 3 refer to the $1^1A''$, $2^1A''$ and $4^1A''$ diabatic states respectively.

The higher order diabatic matrices for the ground state and uncoupled S_1 model contain only coupling terms between modes. All diagonal terms (including a single mode) are contained in V_0. A fourth-order polynomial was used for these. Thus

$$\begin{aligned}
W &= \sum_{i<j} \gamma_{ij} q_i q_j \\
&+ \frac{1}{6}\sum_{i<j} \gamma_{iij} q_i^2 q_j + \frac{1}{6}\sum_{i>j} \gamma_{iij} q_i^2 q_j + \sum_{i<j<k} \gamma_{ijk} q_i q_j q_k \\
&+ \frac{1}{4}\sum_{i<j} \gamma_{iijj} q_i^2 q_j^2 + \frac{1}{6}\sum_{i<j} \gamma_{iiij} q_i^3 q_j + \frac{1}{6}\sum_{i>j} \gamma_{iiij} q_i^3 q_j + \sum_{i<j<k} \gamma_{iijk} q_i^2 q_j q_k \\
&+ \sum_{k<i<j} \gamma_{iijk} q_i^2 q_j q_k + \sum_{j<i<k} \gamma_{iijk} q_i^2 q_j q_k + \sum_{i<j<k<l} \gamma_{ijkl} q_i q_j q_k q_l \qquad (6.6)
\end{aligned}$$

where $q_i = x_i - x_{i0}$ for each mode.

The same scheme was used to describe the coupled three state model diabatic surfaces, ie. on the on-diagonal elements

$$W_{\alpha\alpha} = \sum \gamma_{ij}^{(\alpha)} q_i q_j \cdots \qquad (6.7)$$

The off-diagonal elements of this matrix provide the non-adiabatic coupling. These were simply taken to include all second-order and selected third-order terms

$$W_{\alpha\beta} = \sum_{i<j} \mu_{ij}^{(\alpha\beta)} q_i q_j + \cdots \frac{1}{6}\sum_{i<j} \mu_{iij}^{(\alpha\beta)} q_i^2 q_j + \frac{1}{6}\sum_{i>j} \mu_{iij}^{(\alpha\beta)} q_i^2 q_j + \frac{1}{6}\sum_{i} \mu_{iii}^{(\alpha\beta)} q_i^3 \qquad (6.8)$$

6.4 The Kinetic Energy Operator

The potentials have been fitted using binding coordinates as these are simpler to describe in terms of bonding (Morse) functions. After fitting the surfaces we must carry out the dynamics in the same coordinate system. The KE operator in binding coordinates is attributed to Carney *et al* [94] who in turn attribute it to Hagstrom and Lai [95] and when J=0 is written for FNO

$$\begin{aligned}
T = &- \frac{\hbar^2}{2}\left(\frac{1}{\mu_1}\frac{\partial^2}{\partial r_1^2} + \frac{1}{\mu_2}\frac{\partial^2}{\partial r_2^2}\right) - \frac{\hbar^2}{M_N}\cos\theta\frac{\partial^2}{\partial r_1 \partial r_2} \\
&- \frac{\hbar^2}{2}\left(\frac{1}{\mu_1 r_1^2} + \frac{1}{\mu_2 r_2^2} - 2\cos\theta\frac{1}{m_N r_1 r_2}\right)\left(\frac{\partial^2}{\partial\theta^2} + \cot\theta\frac{\partial}{\partial\theta}\right)
\end{aligned}$$

$$
\begin{aligned}
&+ \frac{\hbar^2}{m_N}\left(\frac{1}{r_2}\frac{\partial}{\partial r_1} + \frac{1}{r_1}\frac{\partial}{\partial r_2} - \frac{1}{r_1 r_2}\right)\sin\theta\frac{\partial}{\partial\theta} \\
&+ \frac{\hbar^2}{m_N}\left(\frac{1}{r_2}\frac{\partial}{\partial r_1} + \frac{1}{r_1}\frac{\partial}{\partial r_2} - \frac{1}{r_1 r_2}\right)\cos\theta. \qquad (6.9)
\end{aligned}
$$

where r_1 and r_2 are the NO and NF bond lengths respectively and θ is the bond angle. m_N is the mass of the central atom in the triatomic which in this case is N and

$$
\begin{aligned}
\frac{1}{\mu_1} &= \frac{1}{m_N} + \frac{1}{m_O} \\
\frac{1}{\mu_2} &= \frac{1}{m_N} + \frac{1}{m_F} \qquad (6.10)
\end{aligned}
$$

where m_O and m_F are the masses of the atoms at the ends of bonds 1 and 2 respectively, in this case O and F.

The complicated form of this operator compared to that in Jacobi coordinates, equation 4.1, shows why the latter are preferred in simulations.

6.5 Wavepacket Dynamics and Calculating the Absorption Spectrum

Wavepacket dynamics were carried out on both the uncoupled $1^1A''$ surface and on the coupled surfaces. The wavepacket was propagated on a grid in NO, NF and θ with N_{NF} and N_{NO} = 101 grid points between -1 and 5 au and N_θ = 51 between -1 and 1 rad. The equilibrium geometry is at (0,0,0). A FFT DVR was used for NO and NF and a Leg DVR for θ. A CAP was placed along NF and NO at 3.5 au to prevent reflection of the wavepacket at the grid edges. Firstly the wavepacket was propagated on both the coupled surfaces and the uncoupled $1^1A''$ surface without the adjustment of any parameters. We then corrected the surfaces for the dissociation energy, 2.38 eV, and for the first excited state VEE of 3.99 eV and repeated the same dynamics calculations.

For the coupled surfaces the wavepacket was relaxed onto the ground state and then was excited into the strongly coupled first and fourth excited states. We also carried out an excitation into the second excited state.

Spectra were generated for all of these calculations.

6.6 Results and Discussion

6.7 Potential Fits

The fitting for the 4 states was carried out using a program called VCHAM which is part of the MCTDH package. Analytical functions are fitted to the *ab initio* data using a least squares fit method

$$F = \sum_i (V_i^{calc} - V_i^{mod})^2 \tag{6.11}$$

where V_i^{calc} and V_i^{mod} are the adiabatic potential energies calculated by *ab initio* and by the model at point i. The V_i^{mod} values are thus the eigenvalues of the adiabatic model Hamiltonian.

After fitting the ground state, a fit was carried out for the $1^1A''$ state only and then a full fit was done to include all three excited states and the coupling between them.

6.7.1 The Ground State Fit

The fitting for the 1D cuts along θ, NO and NF for the $1^1A'$ state are shown in figure 6.2 with the points being the *ab initio* data and the red curve, the fit. Also shown is the fit along the diagonal of NO and NF. For the 1D cuts the fit is very good in all regions, but it must be noted that for the diagonal cut, the fit is not so good out at extended NO and NF bond lengths. This is, however, not a problem for the dynamics as this region of the surface will not be encountered by the wavepacket. A contour plot of the ground state fitted surface along N-O and N-F is shown in figure 6.3. The NO and NF channels are smooth with well defined features. It can be seen that the minimum is not at (0,0), but close to it. This is due to the problem of fitting a Morse curve. The parameters for the functions are in table 6.3.

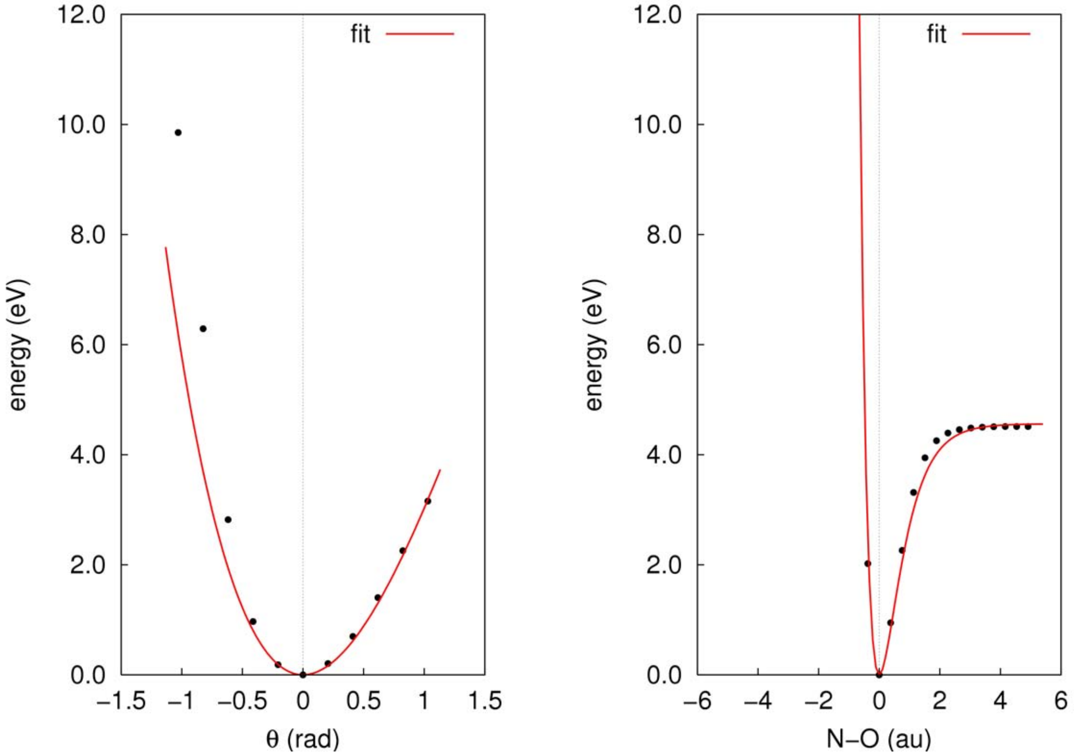

(a) Fit along θ

(b) Fit along NO

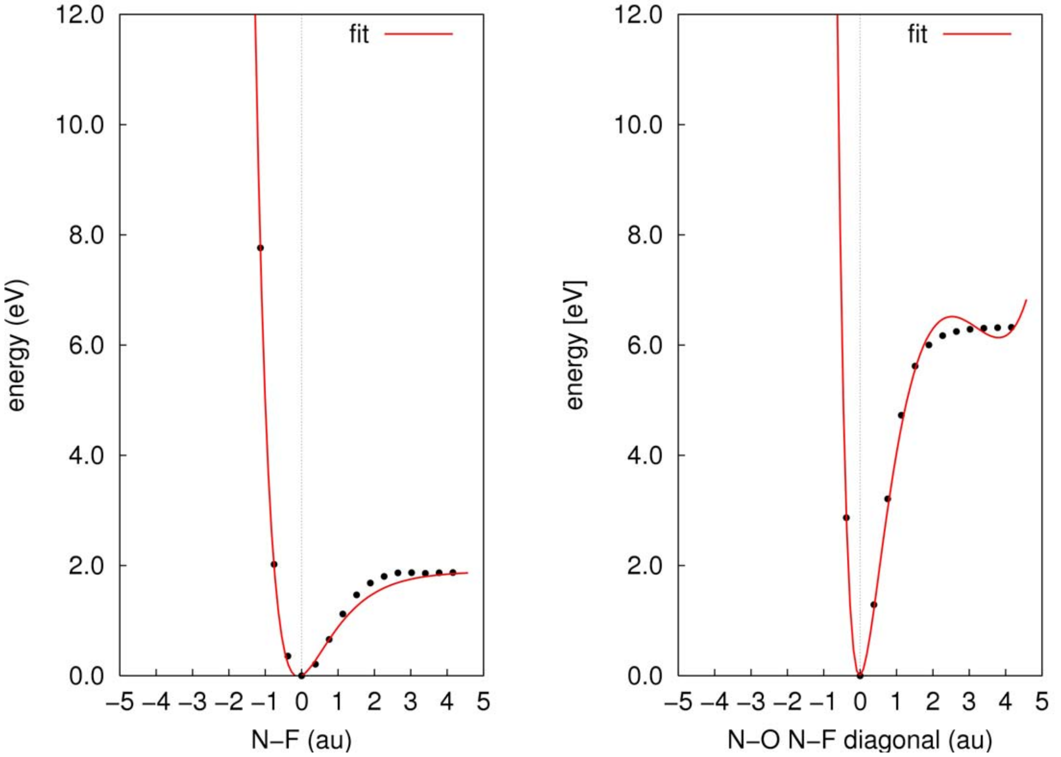

(c) Fit along NF

(d) Fit along NO NF diagonal

Fig. 6.2: Ground state potential fit along the 1D cuts θ, N-O and N-F and along the diagonal of NO and NF. The points are *ab initio* energies calculated at the MS-MR-CASPT2/Huzinaga level.

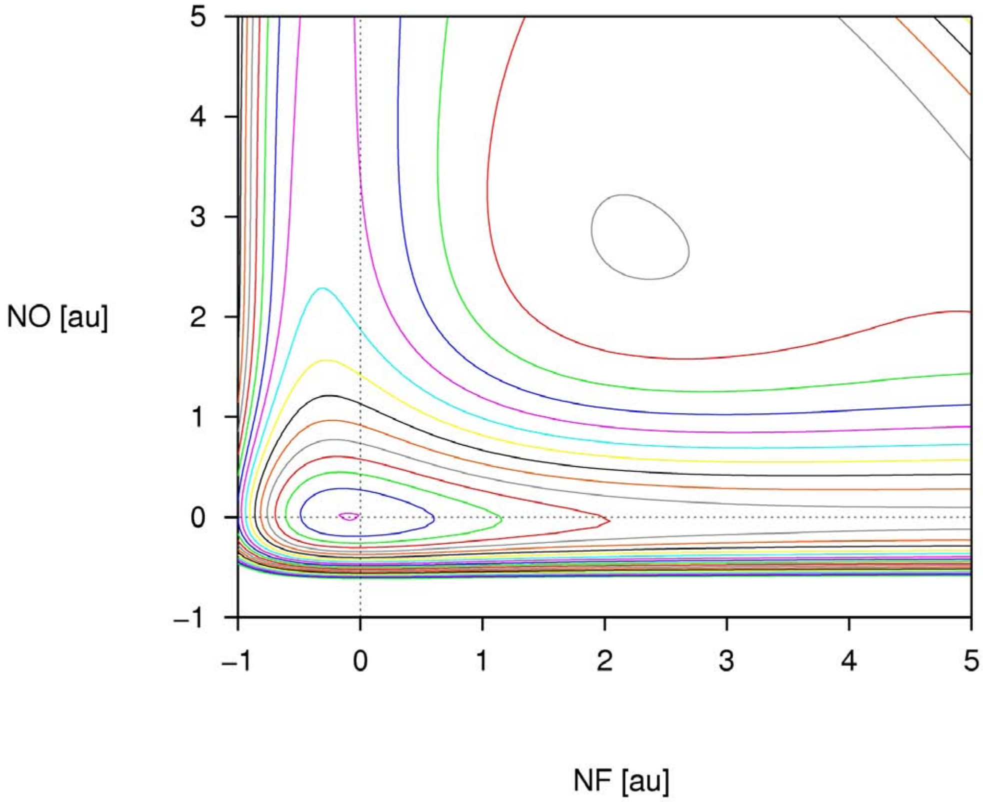

Fig. 6.3: Contour plot of the fitted ground state of FNO along r_2 and r_1 with θ fixed at the equilibrium value of 111°.

6.7.2 The Uncoupled Excited State Fit

The fitted function for the uncoupled $1^1A''$ excited state is shown in figure 6.4. Morse functions were used for the fits along NO and θ. The angular DOF is harmonic in nature and the fit is very good in all regions. The anharmonicity of the NO DOF is also well represented by the Morse function and again a good fit over the whole cut has been achieved. Note the lack of smoothness in the *ab initio* points around NO = 4 au. This is due to the presence of higher states affecting the *ab initio* calculations. One of the advantages of using analytic functions is that such regions are smoothed. The NF DOF is a repulsive curve and has been fitted with an exponential function. There is a discrepancy in the fitting for the NO NF diagonal but once again it occurs in a region of the cut which is not important for the wavepacket dynamics.

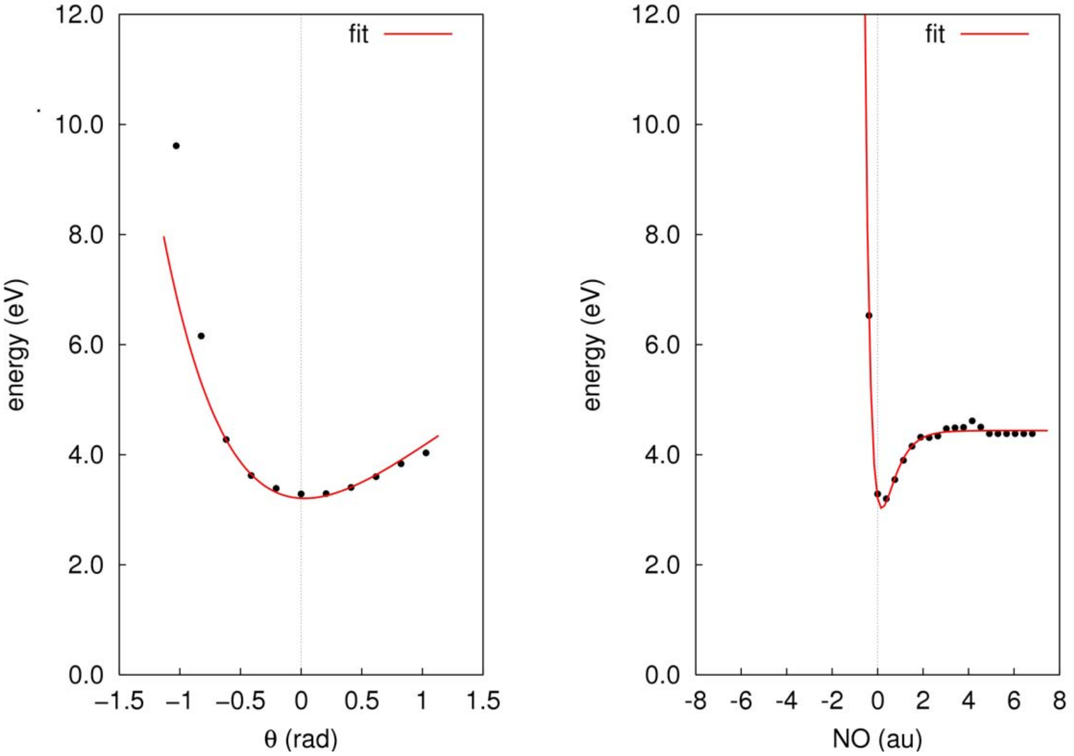

(a) Fit along θ (b) Fit along NO

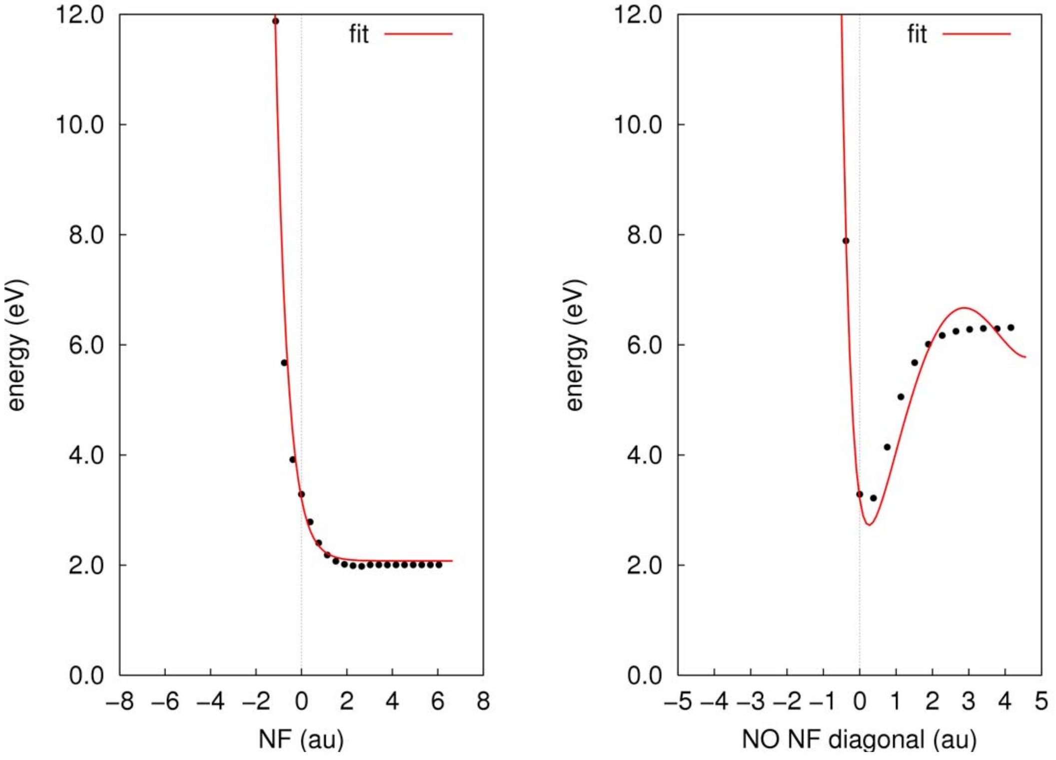

(c) Fit along NF (d) Fit along NO NF diagonal

Fig. 6.4: Excited state potential fit along the 1D cuts θ, N-O and N-F and along the diagonal of NO and NF. The points are *ab initio* energies calculated at the MS-MR-CASPT2/Huzinaga level.

The parameters for the uncoupled potential function are in table 6.4.

6.7.3 The Coupled Excited State Fit

The fitted function for all three excited states is shown in figure 6.5. The cuts are now a lot more complicated and as a results we see that for the fit along θ, the $1^1A''$ is a good fit but the higher state fits are less accurate. Once again we see that where NO = 4 au that the *ab initio* data is not smooth. At longer NO bond lengths, the fit exhibits a curling up or down. Along the NF cut the two lowest states are almost degenerate out at extended bond lengths.

The least accurate fit is along the NO NF diagonal. Firstly the *ab initio* data is not smooth and the fit is not good after 2 au. On the upper state the fit is good for the minimum but at 2 au there is no correlation between the analytic function and the *ab initio* data at all.

The important point to take from this fit is that it is good in the regions of interest. Adding higher order terms to the fit would improve the accuracy in the outer regions.

The parameters for the coupled potential functions for the excited states are in tables 6.5, 6.6 and 6.7 and the coupling between the states in tables 6.8, 6.9 and 6.10.

A plot of the fitted adiabatic and diabatic states is shown in figure 6.6. The basic idea behind the diabatic model is shown by looking at the potential surface cuts along NF in figure 6.6 and figure 6.5 (c). The adiabatic states in figure 6.6 (a) are formed by the diabatic states in figure 6.6 (b) which are strongly coupled by the parameters E_{13}. Thus the lower adiabatic state is a mixture of bound and unbound character. That this is the case is supported by the *ab initio* data, figure 6.5 (c), that shows exactly the kink in the lower curve in figure 6.6 (a).

The contour plots in figure 6.7 are of the $1^1A''$ excited state along NO and NF. Plot (a) shows the fit for the uncoupled surface and (b) includes the coupling from the higher excited states. The most obvious difference between the two surfaces is how the topology of surface (b) has changed along the NF channel due to the effect of the

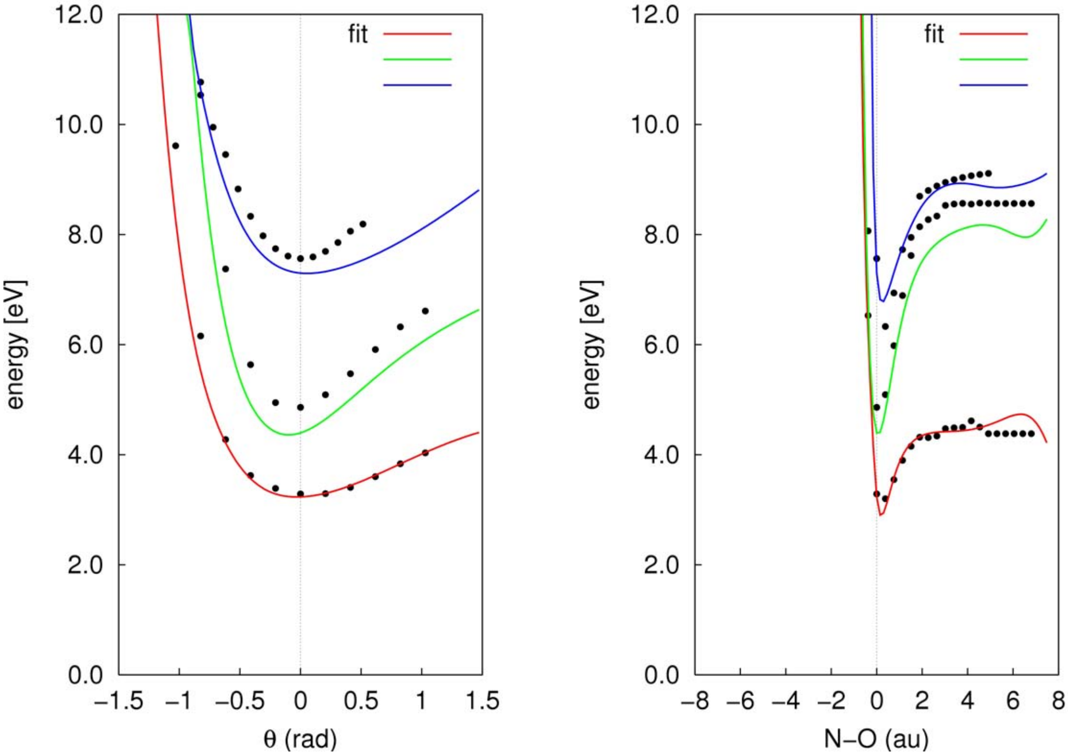

(a) Fit along θ

(b) Fit along NO

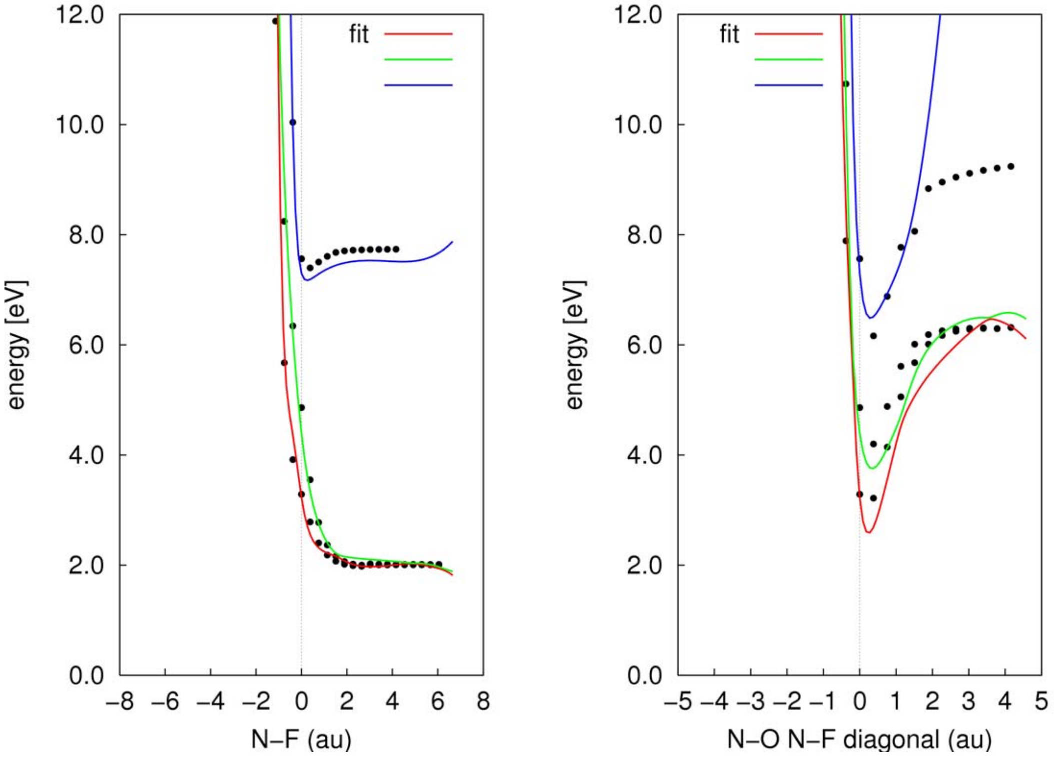

(c) Fit along NF

(d) Fit along NO NF diagonal

Fig. 6.5: Excited state potential fit along the 1D cuts θ, N-O and N-F and along the diagonal of NO and NF. The points are *ab initio* energies calculated at the MS-MR-CASPT2/Huzinaga level.

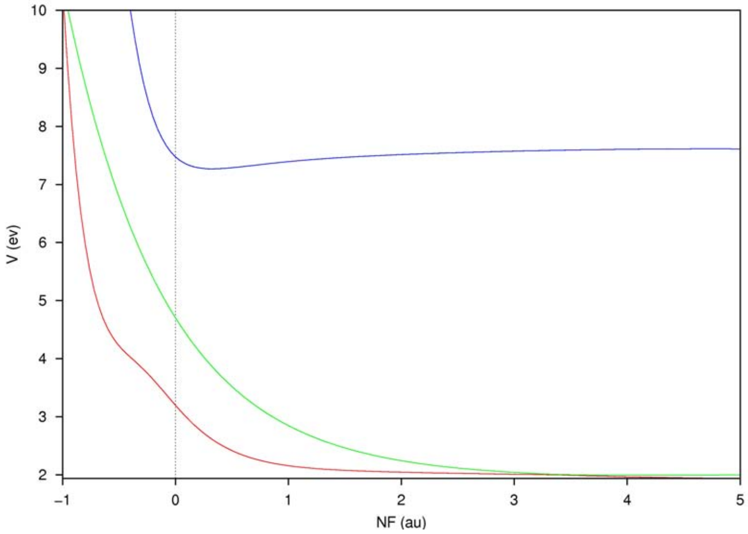

(a) 1D cut along NF of the fitted adiabatic excited states.

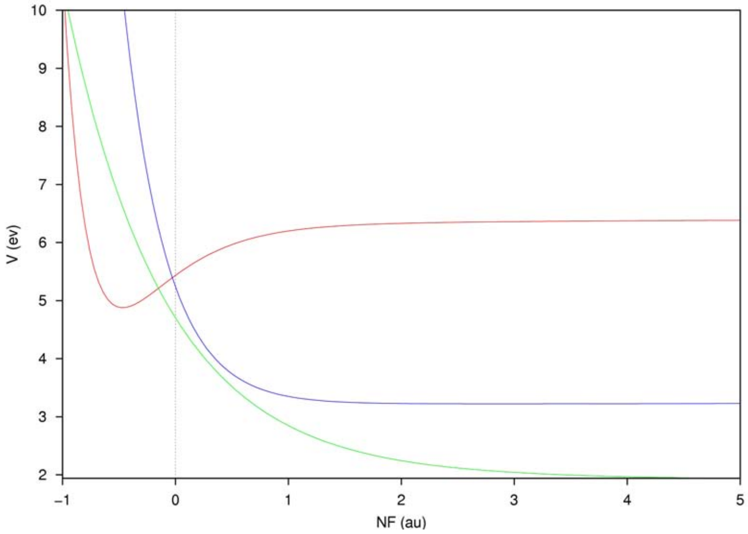

(b) 1D cut along NF of the fitted diabatic excited states.

Fig. 6.6: 1D cuts along NF for the adiabatic and diabatic excited $^1A''$ states.

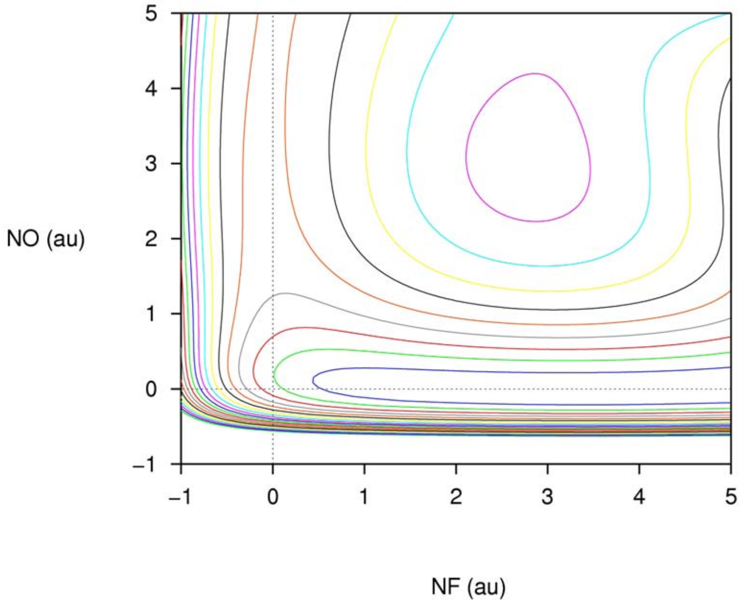

(a) Contour plot of the fitted $1^1A''$ state of FNO along NO and NF with θ fixed at the equilibrium value of 111°. No coupling from the higher excited states is included in this fit.

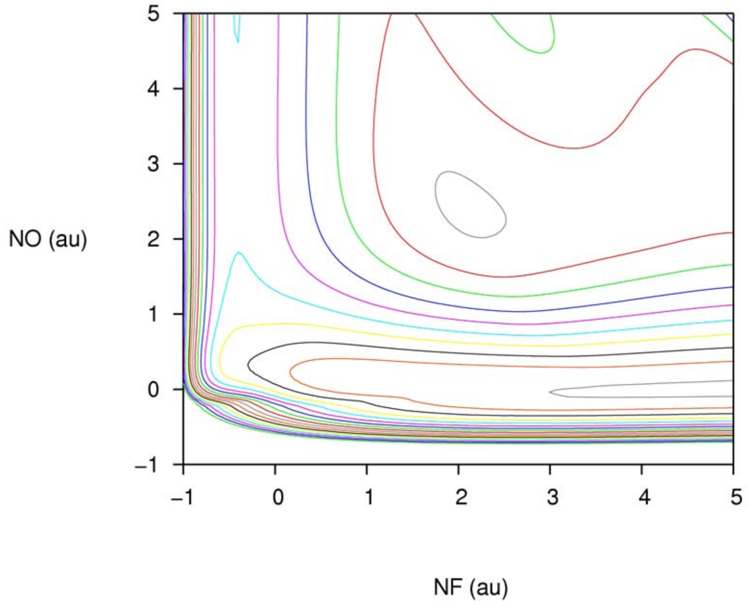

(b) Contour plot of the fitted $1^1A''$ excited state along NO and NF with θ fixed at the equilibrium value of 111°. Coupling from the higher excited states is included in this fit.

Fig. 6.7: Contour plot of the fitted $1^1A''$ state of FNO along NO and NF with θ fixed at the equilibrium value of 111°. Plot (a) does not include any coupling and plot (b) includes coupling from the $2^1A''$ and $4^1A''$ excited states.

coupling. There is a kink in plot (b) as a result. Looking at the same surface from the *ab initio* data in the previous chapter, section 5.3.6, figure 5.10 we see that the shoulder in the NO channel is similar to the coupled surface here.

6.8 The Parameters

The diabatic potential parameters are listed here in the following tables. All values are in au and relate to equations 6.6 and 6.8.

Table 6.3: Diabatic potential parameters for the $1^1A'$ ground state.

$1^1A'$	Second Order		Third Order		Fourth Order	
	γ_{12}	0.3954	γ_{112}	-0.2223	γ_{1122}	0.3617
	γ_{13}	0.5701	γ_{113}	-0.4143	γ_{1133}	0.3859
	γ_{23}	0.8379	γ_{221}	-3.5737	γ_{2233}	0.0522
			γ_{223}	-0.4986		
			γ_{331}	-0.9173	γ_{1112}	0.2331
			γ_{332}	-0.3996	γ_{1113}	0.2044
					γ_{2223}	0.0789
			γ_{123}	-0.2891	γ_{2221}	0.0463
					γ_{3331}	0.1412
					γ_{3332}	0.1190
					γ_{1123}	0.3564
					γ_{3312}	0.0299
					γ_{2213}	0.0337

Table 6.4: Diabatic potential parameters for the uncoupled $1^1A''$ excited state.

$1^1A''$					
Second Order		Third Order		Fourth Order	
γ_{12}	0.7220	γ_{112}	-0.5590	γ_{1122}	0.1881
γ_{13}	0.1531	γ_{113}	-0.2436	γ_{1133}	0.0417
γ_{23}	1.8198	γ_{221}	-1.3277	γ_{2233}	0.0864
		γ_{223}	-0.5818		
		γ_{331}	-0.7705	γ_{1112}	0.2420
		γ_{332}	-0.7994	γ_{1113}	0.3300
				γ_{2223}	0.1402
		γ_{123}	-0.1039	γ_{2221}	0.1724
				γ_{3331}	0.1468
				γ_{3332}	0.0185
				γ_{1123}	0.0445
				γ_{3312}	0.0038
				γ_{2213}	0.0183

Table 6.5: Diabatic potential parameters for the coupled $1^1A''$ excited state.

$1^1A''$					
Second Order		Third Order		Fourth Order	
γ_{12}	0.9695	γ_{112}	-0.7749	γ_{1122}	0.3957
γ_{13}	1.2817	γ_{113}	0.1100	γ_{1133}	0.6115
γ_{23}	0.3877	γ_{221}	-2.9104	γ_{2233}	-0.0272
		γ_{223}	0.2713		
		γ_{331}	-2.9303	γ_{1112}	4.1883
		γ_{332}	-0.2350	γ_{1113}	3.3937
				γ_{2223}	0.0732
		γ_{123}	-0.8930	γ_{2221}	0.1018
				γ_{3331}	-0.4534
				γ_{3332}	-0.1166
				γ_{1123}	-0.0826
				γ_{3312}	-0.0578
				γ_{2213}	-0.1286

Table 6.6: Diabatic potential parameters for the coupled $2^1A''$ excited state.

$2^1A''$	Second Order		Third Order		Fourth Order	
	γ_{12}	-0.0101	γ_{112}	0.0045	γ_{1122}	0.7832
	γ_{13}	-0.1691	γ_{113}	-0.3149	γ_{1133}	0.2392
	γ_{23}	1.7568	γ_{221}	-4.8095	γ_{2233}	0.1057
			γ_{223}	-1.1066		
			γ_{331}	-2.6322	γ_{1112}	2.5780
			γ_{332}	-0.5873	γ_{1113}	1.7670
					γ_{2223}	0.0511
			γ_{123}	-0.3061	γ_{2221}	-0.0024
					γ_{3331}	0.4996
					γ_{3332}	0.2723
					γ_{1123}	0.6065
					γ_{3312}	-0.0071
					γ_{2213}	0.0790

Table 6.7: Diabatic potential parameters for the coupled $4^1A''$ excited state.

$4^1A''$	Second Order		Third Order		Fourth Order	
	γ_{12}	1.6135	γ_{112}	-0.5499	γ_{1122}	0.2834
	γ_{13}	0.6081	γ_{113}	0.5407	γ_{1133}	0.2812
	γ_{23}	1.7169	γ_{221}	-2.9214	γ_{2233}	0.0709
			γ_{223}	-0.9570		
			γ_{331}	-2.8848	γ_{1112}	2.6144
			γ_{332}	-0.8172	γ_{1113}	1.7992
					γ_{2223}	0.1932
			γ_{123}	-1.1369	γ_{2221}	0.0689
					γ_{3331}	-0.4766
					γ_{3332}	0.2847
					γ_{1123}	0.2806
					γ_{3312}	0.1414
					γ_{2213}	0.0690

Table 6.8: Coupling constants for the coupled $1^1A''$ and $2^1A''$ excited states.

$1^1A''$-$2^1A''$					
First Order		Second Order		Third Order	
μ_1	0.0093	μ_{11}	0.0016	μ_{112}	-0.3847
μ_2	0.5459	μ_{12}	1.2524	μ_{113}	0.7571
μ_3	0.0236	μ_{22}	-0.1336	μ_{221}	-1.6073
		μ_{31}	-2.0721	μ_{222}	-0.0026
		μ_{32}	-0.1156	μ_{223}	-0.0586
		μ_{33}	-0.0089	μ_{331}	2.2282
				μ_{332}	0.0022
				μ_{333}	0.0018

Table 6.9: Coupling constants for the coupled $1^1A''$ and $4^1A''$ excited states.

$1^1A''$-$4^1A''$					
First Order		Second Order		Third Order	
μ_1	-0.0224	μ_{11}	0.2360	μ_{112}	-0.0696
μ_2	-0.4576	μ_{12}	-0.0993	μ_{113}	-0.2314
μ_3	0.0665	μ_{22}	0.1628	μ_{221}	-0.3114
		μ_{31}	0.7233	μ_{222}	-0.0210
		μ_{32}	-0.4439	μ_{223}	0.0651
		μ_{33}	0.0040	μ_{331}	0.1955
				μ_{332}	0.1052
				μ_{333}	-0.0082

Table 6.10: Coupling constants for the coupled $2^1A''$ and $4^1A''$ excited states.

$2^1A''$-$4^1A''$

First Order		Second Order		Third Order	
μ_1	0.0095	μ_{11}	0.0121	μ_{111}	0.0024
μ_2	-0.1187	μ_{12}	1.3393	μ_{112}	-0.5477
μ_3	0.0111	μ_{22}	0.0018	μ_{113}	0.6025
		μ_{31}	-1.2497	μ_{221}	-0.7984
		μ_{32}	0.3062	μ_{222}	0.0039
		μ_{33}	-0.0047	μ_{223}	-0.1312
				μ_{331}	0.5650
				μ_{332}	-0.0149
				μ_{333}	0.0015

Table 6.11 lists the parameters for the Morse and exponential functions. The values (in au) relate to equations 6.3 and 6.4 for the Morse and exponential functions.

Table 6.11: The parameters for the Morse and exponential functions are listed in this table. V_i where $i = 1, 3$ denotes the electronic state and M_i where $i = 1, 3$ denotes the mode. Mode 1 is the angular DOF, mode 2 and mode 3 are the NO and NF bonds respectively.

$1^1A'$ Ground State Parameters

		Morse Function Parameters				Exponential Function Parameters	
	Function	D_i	α_i	x_i	E_{i0}	E_0	A
V_1M_1	Morse	39.5233	0.3239	0.0000	0.0000		
V_1M_2	Morse	4.5600	1.4727	0.0000	0.0000		
V_1M_3	Morse	1.9093	1.0603	-0.0928	-0.0168		

$1^1A''$ Uncoupled Excited State Parameters

		Morse Function Parameters				Exponential Function Parameters	
	Function	D_i	α_i	x_i	E_{i0}	E_0	A
V_1M_1	Morse	5.0534	0.5835	0.0292	-0.0015		
V_1M_2	Morse	1.4115	1.6915	0.1811	-0.1814		
V_1M_3	Exponential					1.1318	1.8687

1,2 and $4^1A''$ Coupled Excited State Parameters

		Morse Function Parameters				Exponential Function Parameters	
	Function	D_i	α_i	x_i	E_{i0}	E_0	A
V_1M_1	Morse	0.7306	1.7268	-0.1922	-0.0583		
V_1M_2	Morse	0.9912	2.1858	0.3430	-1.2356		
V_1M_3	Morse	1.4451	2.0637	-0.4672	-1.5532		
V_2M_1	Morse	3.9237	1.1254	-0.0648	-0.0194		
V_2M_2	Morse	4.1755	1.1764	0.0536	-0.0177		
V_2M_3	Exponential					2.7881	1.1234
V_3M_1	Morse	7.3327	0.5561	0.1253	-0.0382		
V_3M_2	Morse	2.8917	1.3201	0.1865	-0.2252		
V_3M_3	Exponential					2.0598	2.6587

6.9 Absorption Spectra from the Fitted States

6.9.1 The Uncoupled State

The spectrum shown in figure 6.8 was obtained by initial relaxation on S_0 followed by propagation on S_1 for 100 fs. It is clear from this spectrum that the wavepacket has undergone direct dissociation down the NF channel. There is no structure present in the spectrum at all. Just fitting to the *ab initio* data for this surface does not produce the topological features which give rise to the structured part of the spectrum. We then took the wavepacket and gave it a specific initial position on the same surface.

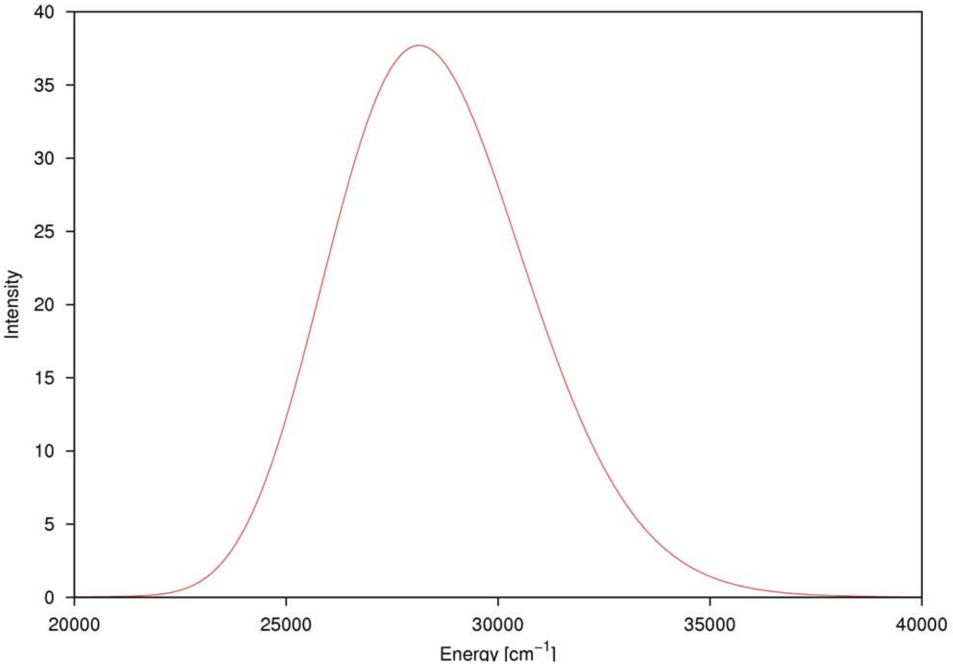

Fig. 6.8: Absorption spectrum generated from the wavepacket dynamics on the uncoupled $1^1A''$ surface after relaxation.

Many calculations were carried out at this stage and we found that the best spectrum was obtained when the wavepacket was displaced along the NO channel by 1.3 au. This spectrum is shown in figure 6.9. There is now some structure present in the spectrum and it exhibits two main frequencies. The dynamics show that the wavepacket

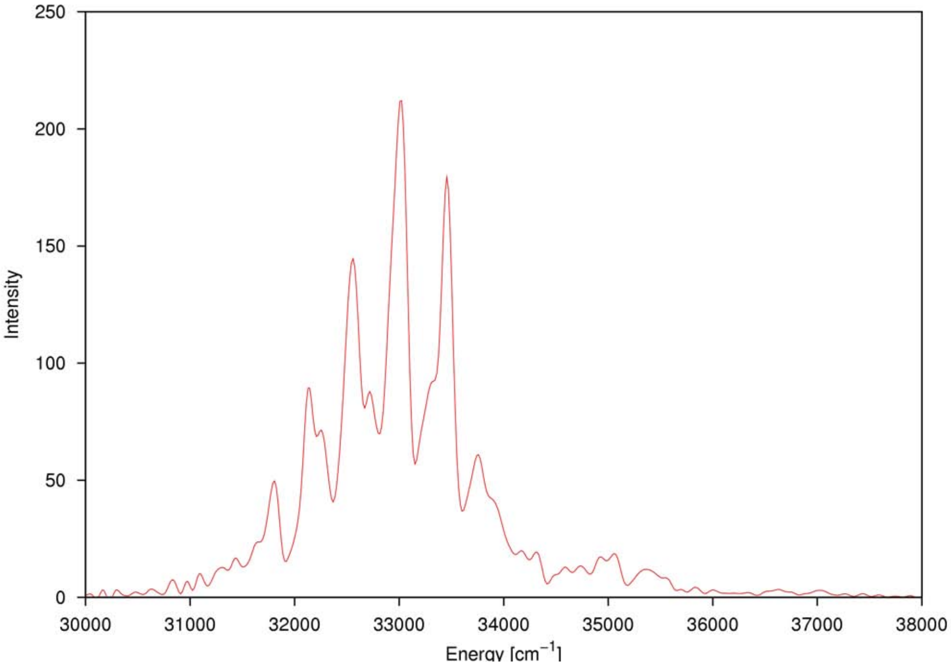

Fig. 6.9: Absorption spectrum generated from the wavepacket dynamics on the uncoupled $1^1A''$ surface. The wavepacket was initially placed on the surface at the equilibrium positions for NF and θ and displaced down the NO channel by 1.3 au.

dissociates and that there is no propagation along the NO channel at all. The structure present in the spectrum is due to the motion of the NO bond as the wavepacket moves along the NF channel.

6.9.2 The Coupled States

The spectrum in figure 6.10 was generated from the dynamics carried out on the coupled excited states. After relaxation the wavepacket was excited equally to the $1^1A''$ and $4^1A''$ excited states. The spectrum is highly structured and the dynamics show propagation along both channels with a distinct bifurcation in the wavepacket at 25 fs. The placement of the spectrum, 22000 cm^{-1}, is far lower than the experimental value of 32500 cm^{-1} and it is clear from this that the VEE for the S_1 surface needs to be corrected. This spectrum is a sum of excitations to the first and fourth excited states.

The spectrum in figure 6.11 is the result of excitation into the $2^1A''$ state.

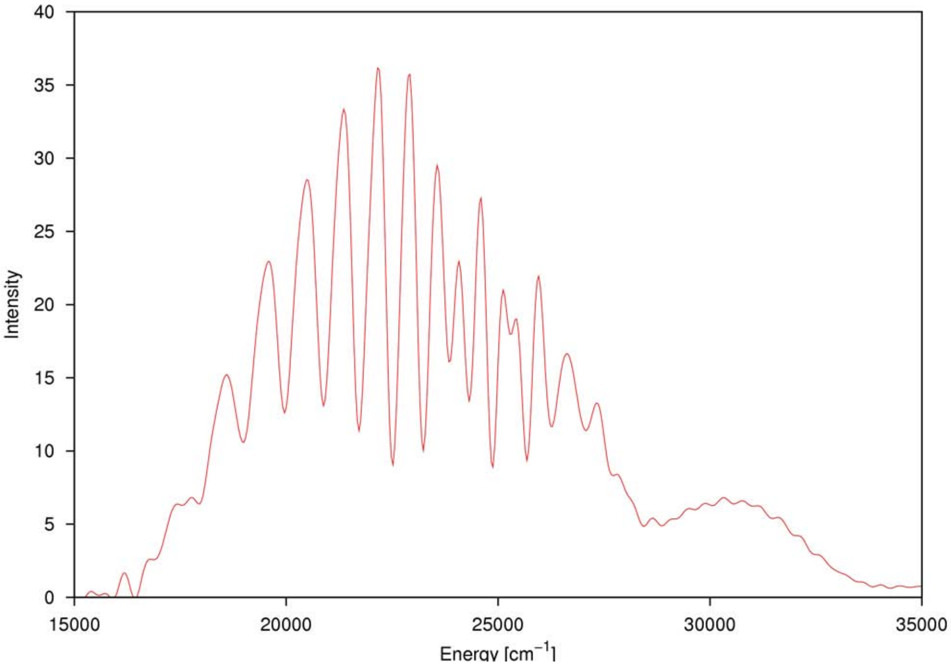

Fig. 6.10: Absorption spectrum generated from the wavepacket dynamics on the $1^1A''$ and $4^1A''$ coupled excited states after relaxation on S_0.

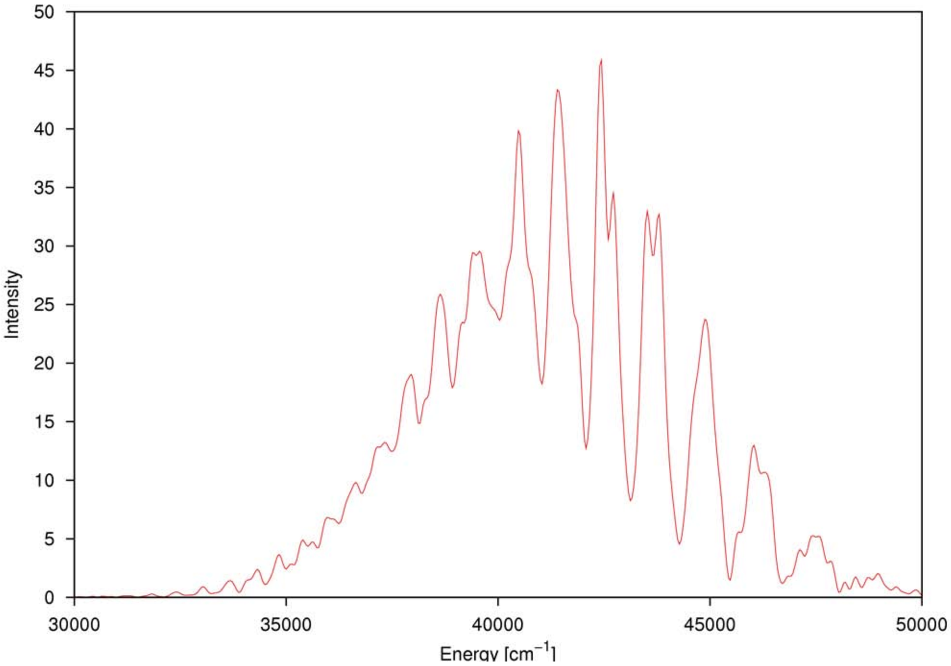

Fig. 6.11: Absorption spectrum generated from the wavepacket dynamics on the 3 coupled excited states of $^1A''$ symmetry after excitation to the $2^1A''$ state following relaxation on S_0.

6.10 Absorption Spectra from the Corrected Fitted States

None of the spectra generated so far have reproduced the experimental spectrum. The next step to try and achieve this is to alter the parameters for the analytic functions to correct for the VEE and the dissociation energy in the surfaces.

6.10.1 The Uncoupled State

The $1^1A''$ state which was fitted without coupling was corrected for the VEE and for the dissociation energy. This involved changing the parameters E_1 and E_{13} to change the VEE and dissociation energy respectively. After relaxation on the ground state and propagation of the wavepacket on this state we found that direct dissociation occurred once again and that correcting the surface did not change the overall topology of the surface. The shallow well which gives rise to the main progression in the spectrum is still not present in the uncoupled surface to trap any part of the wavepacket and hence we find that the spectrum was featureless.

6.10.2 The Coupled States

For the coupled model major changes in the surface topology between $1^1A''$ and $4^1A''$ occur by changing the coupling, E_{13}. 1D cuts along NF are plotted in figure 6.12 for the three coupled excited states with values of 0.5, 0.9 and 1.2 for this parameter (fitted value ~ 2.0).

It can be seen that an increasing value of E_{13} raises the VEE and accentuates the minimum. The $1^1A''$ state has been corrected for VEE and dissociation energy. Several calculations were carried out at this stage and it was found that the effect of changing the parameters just slightly produces quite dramatic effects in the resulting absorption spectra. The most noticeable effect that altering this parameter has is on the small well in the $1^1A''$ state. Plot (a) which has been adjusted to 0.5 au has a much deeper well

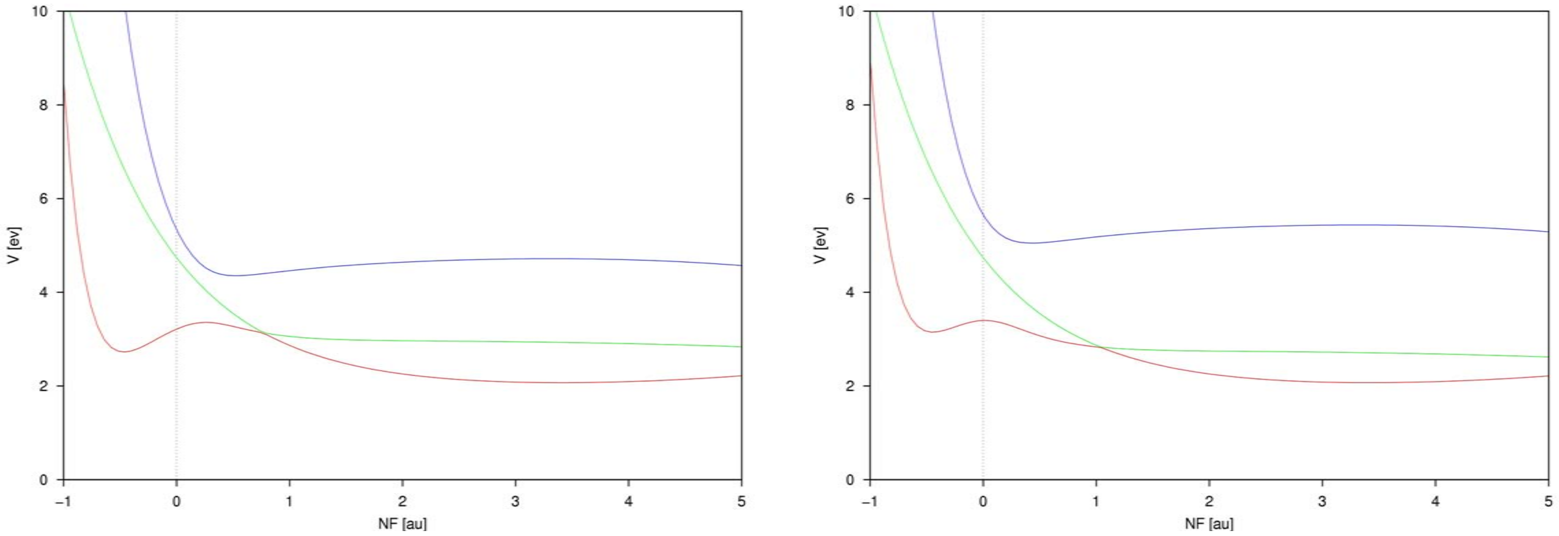

(a) $E_{13} = 0.5$ au

(b) $E_{13} = 0.9$ au

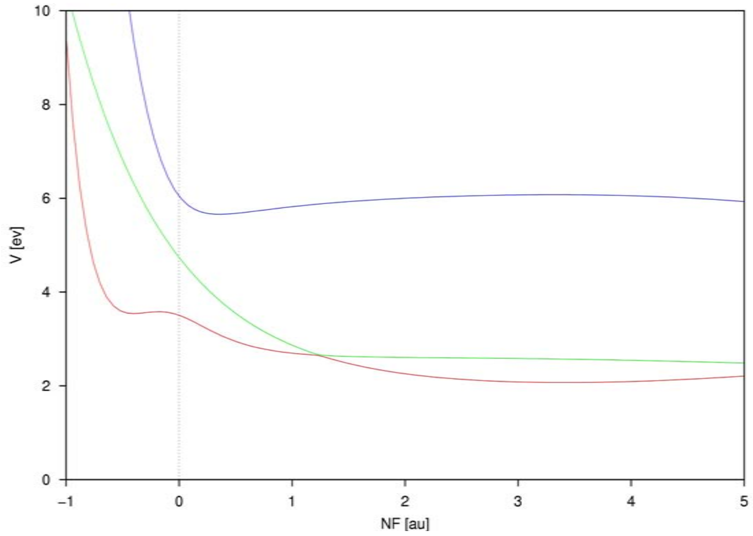

(c) $E_{13} = 1.2$ au

Fig. 6.12: 1D Cut along the N-F bond of the three excited states. The states have been altered by changing the coupling strength, E_{13}, between the $1^1A''$ and $4^1A''$ diabatic states.

than the other two plots. By increasing the amount of adjustment, the well becomes less pronounced.

A contour plot along NO and NF of the $1^1A''$ state with $E_{13} = 0.9$ au is shown in figure 6.13. The kink along NF has become more pronounced, see figure 6.7 (b) for the fitted surface without correction.

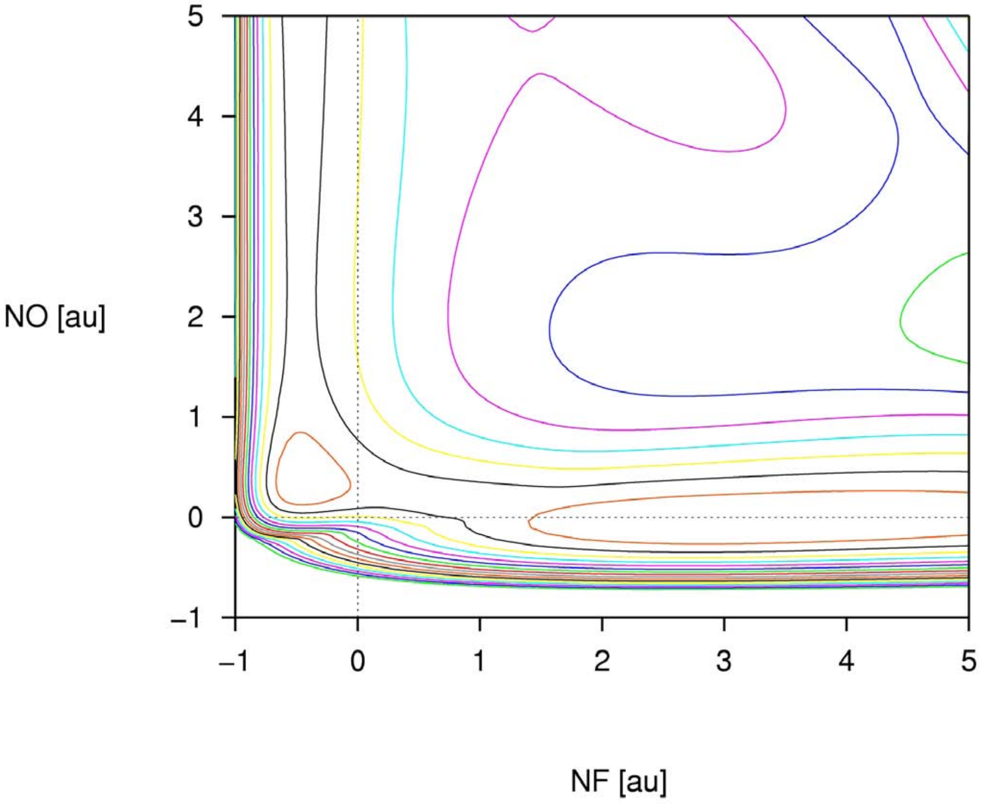

Fig. 6.13: Contour plot along NO and NF of the corrected coupled $1^1A''$ excited state. The value of E_{13} is set to 0.9 au.

The spectra which result from propagation on these surfaces are shown in figure 6.14. From the dynamics (not shown) we see that where the well is most deep, plot (a), there is a bifurcation of the wavepacket into three parts. A small portion of the wavepacket becomes trapped in the well giving rise to the highly structured part of the spectrum. A large part propagates straight down the NO channel and a small

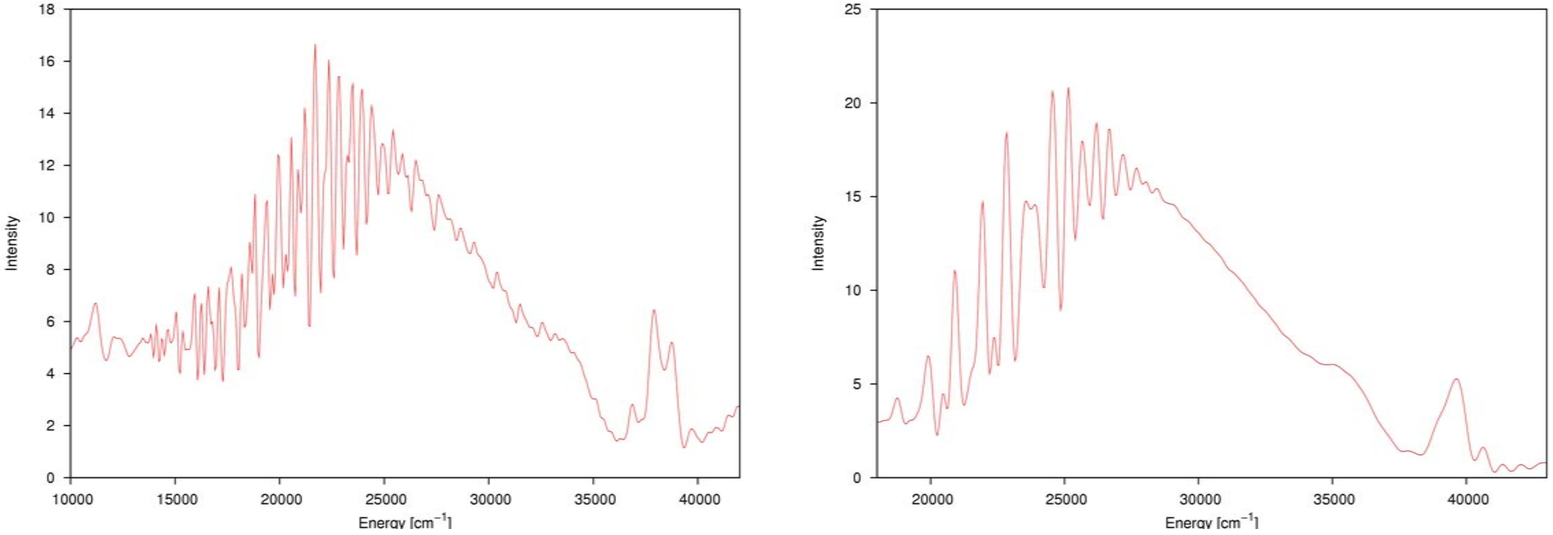

(a) Corrected dissociation energy by 0.5 au

(b) Corrected dissociation energy by 0.9 au

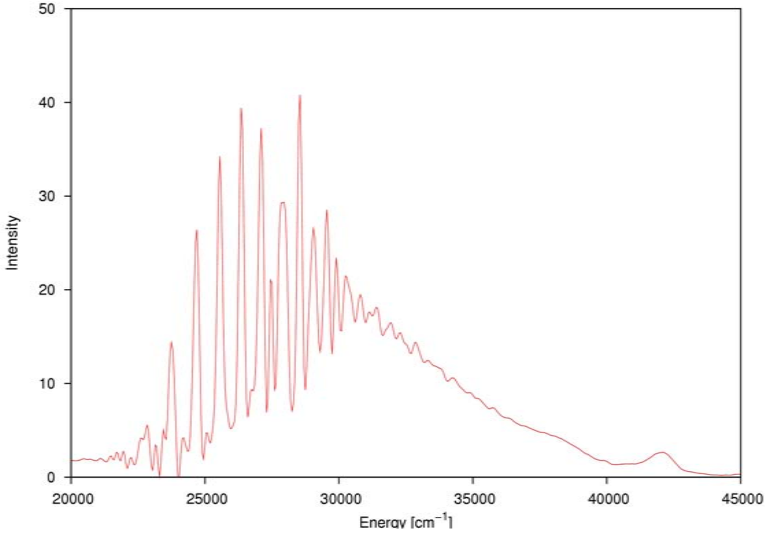

(c) Corrected dissociation energy by 1.2 au

Fig. 6.14: Absorption spectra for the corrected coupled excited states. The excitation energy has been corrected for by changing the coupling strength, E_{13}, between the $1^1A''$ and $4^1A''$ diabatic states and three different values are used to show the effect this has on the spectrum. Plot (a) has an adjusted value of 1.2, (b) of 0.5 and (c) of 0.9 au.

part dissociates along NF. There are several frequencies present in the spectra due to the wavepacket trapped in the well and also to the motion of the NO bond as the wavepacket moves down the NF channel.

In plot (b), where the well is slightly less pronounced, we see less of the structure due to the trapping of the wavepacket within the well. The dynamics show a similar pattern to (a) with a threeway bifurcation but this time there is less of the wavepacket becoming trapped in the well.

Spectrum (c) is representative of what would be expected of the now much shallower well that we see in figure 6.12 (c).

6.11 Conclusions

In this study we have successfully carried out a potential fit with the MS-MR-CASPT2 *ab initio* data from the previous chapter. A good fit was obtained in the important regions of the surface where the wavepacket was propagated. To improve the accuracy of the fit at extended NO and NF bond lengths, higher order terms would need to be included.

The coupling between the excited states has not been investigated in previous work. We have shown that the $1^1A''$ excited state is strongly coupled to the $2^1A''$ and $4^1A''$ excited states and that as a consequence of this, the S_1 surface develops a shallow well along the NO channel. It is this well which gives rise to the main progression in the spectrum. By fitting the uncoupled $1^1A''$ excited state we have shown that this well is not present unless coupling is included in the fit.

Absorption spectra have been generated from the wavepacket dynamics on the coupled and uncoupled surfaces. The wavepacket propagation on the uncoupled surface underwent rapid direct dissociation and produced a featureless spectrum as a result. Even after the surface was corrected for the VEE, no change was present in the spectrum. This indicates how vital the coupling is to the topology of the surfaces and hence the outcome of the absorption spectrum.

The spectrum from the coupled surfaces showed high levels of structure due to the presence of the shallow well. The excitation energy was corrected for by adjusting the coupling strength between the $1^1A''$ and $4^1A''$ states. The well in the $1^1A''$ state became more or less pronounced by adjusting this parameter and the change in topology induced a threeway bifurcation in the wavepacket. The majority of the wavepacket propagated down the NO channel with small portions becoming trapped in the well and dissociating along NF. The resulting spectra were highly structured and exhibited more than one frequency.

Although we were unable to reproduce the experimental spectrum we have shown the importance of the excited state coupling and have again illustrated how sensitive this system is due to the subtle features present in the surfaces. We have shown that by changing one parameter, E_{13}, that the resulting spectra are greatly affected due to the coupling strength between the first and fourth A'' states.

Chapter 7

The Ultrafast Photodissociation of Chromium Hexacarbonyl

7.1 Literature Review

It is known that $Cr(CO)_6$ eliminates a carbon monoxide ligand on photoexcitation [96, 97] to produce the coordinatively unsaturated $Cr(CO)_5$ complex and the photodissociation of metal hexacarbonyls, $M(CO)_6$ where M is Cr, Mo or W, has been investigated on a femtosecond timescale using pump-probe techniques [98]. The total times for dissociation were found by Fuß *et al* to be 110, 165 and 195 fs respectively. These studies together with theoretical studies of $Cr(CO)_6$ [99] show that the mechanism by which the initial ligand is lost does not proceed via a single straight forward dissociation step but that a rather more complex sequence of events is involved. At low temperature and in liquid solution UV photolysis results in the loss of only one of the CO ligands to form the pentacarbonyl intermediate in its excited S_1 state where upon it undergoes relaxation to the S_0 ground state. However, in the gas phase $Cr(CO)_5$ undergoes sequential stripping of the 5 remaining CO ligands to leave the bare metal atom [100].

The first assignment of the electronic spectrum of $Cr(CO)_6$ was published in 1963 and then again in 1968 by Beach and Gray [101, 102] and it was thought that the photodissociation process involved a simple bond breaking step via a d-d ligand field (LF) excited state leading to the formation of $Cr(CO)_5$ in its S_0 ground state. An experimental absorption spectrum is shown in figure 7.1 taken from [103] as Beach and Gray did not publish their measured spectrum. It has since been determined by experiment [104] and by theoretical studies [105,106] that, although the LF excitation is indeed the dissociative state which ultimately leads to the formation of $Cr(CO)_5$, the metal-to-ligand charge transfer (MLCT) states play a role in the mechanism. The MLCT states are not themselves dissociative but are the states populated by UV transitions and that it is via crossings of these states that the molecule finds its way to dissociation on the LF state. On formation $Cr(CO)_5$ is found to be in its S_1 state where it undergoes relaxation to the ground state via a Jahn-Teller (JT) conical intersection [99].

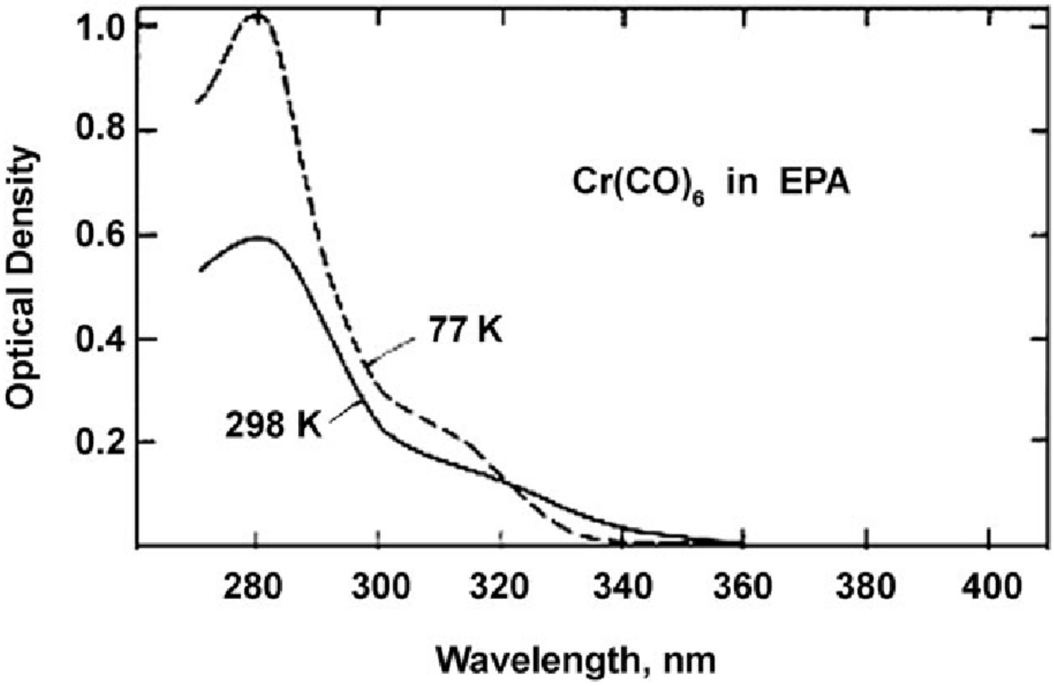

Fig. 7.1: Experimental absorption spectrum for $Cr(CO)_6$ taken from [103].

Chemical processes are usually described by the adiabatic approach using the BO approximation as a means of simplifying the quantum mechanical treatment of molecular structures by separating the electronic and nuclear motions. The dissociation of

$Cr(CO)_6$, however, cannot be dealt with in this way as there are interactions between the electronic and nuclear motions which cannot be ignored.

The electronic spectrum of $Cr(CO)_6$ reported by Beach and Gray was measured both in solution and in the vapour phase and was found to be dominated by two intense bands at 4.4 and 5.5 eV. These two bands were identified as the only two orbitally and spin allowed MLCT excitations with the electronic transitions $^1A_{1g}(2t_{2g}^6) \rightarrow$ $^1T_{1u}(2t_{2g}^5, 9t_1u^1)$ and $^1A_{1g}(2t_{2g}^6) \rightarrow {}^1T_{1u}(2t_{2g}^5, 2t_2u^1)$.

In addition to this, two weak bands were observed on the low energy side of the first charge transfer (CT) band at 3.6 and 3.9 eV and were assigned as vibrational components of the orbitally forbidden but spin allowed LF transitions $^1A_{1g}(2t_{2g}^6) \rightarrow^1 T_{1g}(2t_{2g}^5$ $, 6e_g^1)$. Another weak shoulder was observed between the two CT bands at 4.8 eV and was attributed to the LF excitation $^1A_{1g}(2t_{2g}^6) \rightarrow^1 T_{2g}(2t_{2g}^5, 6e_g^1)$. It was long believed [107] that on photo excitation the LF states were low enough in energy to be directly populated and that dissociation would proceed via a single bond breaking step. There was little reason to revise this assignment as irradiation to the low energy-shoulder did indeed lead to photodissociation as would be expected if this were the dissociative LF state.

This assignment was widely accepted until 1996 when it was reassigned by Pierloot *et al* [105] who calculated the spectrum using multiconfigurational perturbation theory based on a complete active space wave function (the CASSCF/CASPT2 approach). The orbital active space was chosen to include all the valence orbitals required for a good description of bonding in the complex. An earlier study on the bonding properties of $Cr(CO)_6$ [52] showed that a 10-orbital active space, including the bonding and antibonding combinations of the metal 3d and CO valence orbitals, would include the major electronic features of the molecule. In $Cr(CO)_6$ the Cr 3d orbitals form the $2t_{2g}$ and $6e_g$ shells, and the $^1A_{1g}$ ground state corresponds to the $2t_{2g}^6$ configuration. The complete active space (CAS), therefore, consists of the (2,3) t_{2g} and (5,6) e_g shells including 10 valence electrons. A qualitative picture of the MO's is shown in figure 7.2 and is taken from [99]. As much as a good description of the ground state is crucial, so

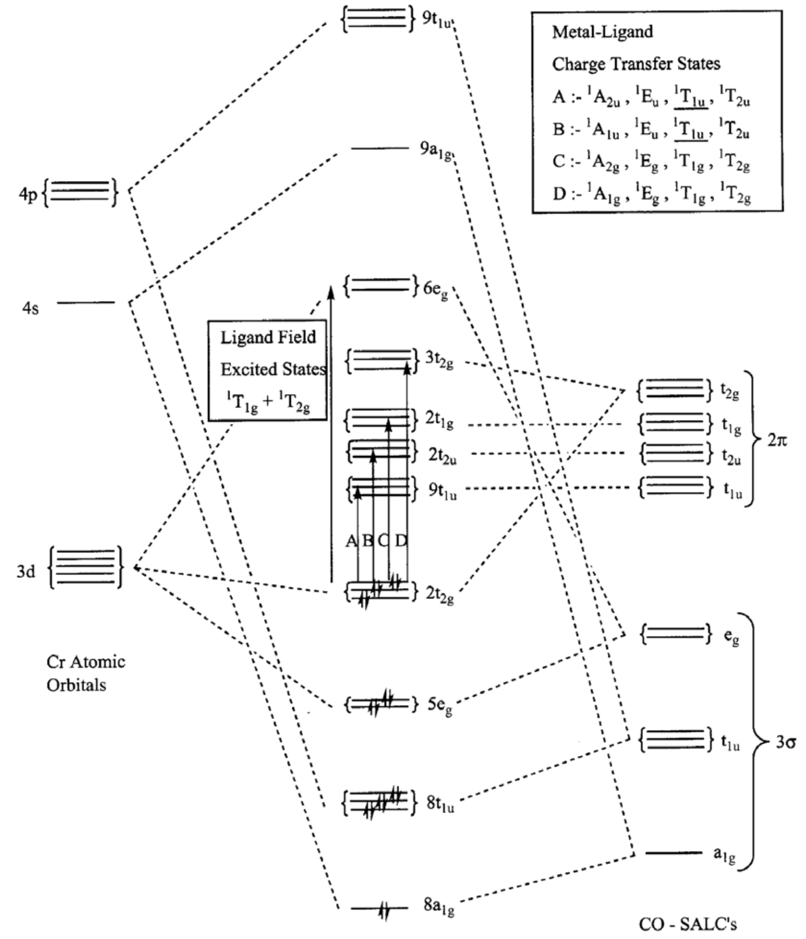

Fig. 7.2: Qualitative MO diagram for $Cr(CO)_6$ showing the bonding between the metal d-orbitals and the CO symmetry adapted linear combinations of atomic orbitals taken from [99].

the MLCT excited states are equally important if a full description of the dissociation mechanism is to be achieved. For $Cr(CO)_6$ the MLCT excitations from the metal 3d orbitals into the vacant orbitals of the ligands would mean including 12 CO $2\pi^*$ orbitals residing in the $2t_{1g}$, $3t_{2g}$, $9t_{1u}$ and $2t_{2u}$ shells. Only the $3t_{2g}$ was already included in the basic 10-orbital active space and adding the 3 other shells would have resulted in an active space with as many as 19 orbitals, which was too large to be handled by the present CASSCF/CASPT2 version.

Pierloot *et al* used an alternative method to overcome this problem. They used different active spaces according to which excited state they wanted to investigate. The $2\mathrm{t}_{2\mathrm{g}} \rightarrow 6\mathrm{e}_{\mathrm{g}}$ LF excited states of gerade symmetry were included in an active space of 13 orbitals built from the basic 10 plus the $2\mathrm{t}_{1\mathrm{g}}$ shell. The MLCT states of ungerade symmetry used the basic 10 plus the $9\mathrm{t}_{1\mathrm{u}}$ and the $2\mathrm{t}_{2\mathrm{u}}$ shells but, as this resulted in an unmanageable 16 orbitals, both shells were added separately. The results were in agreement with the bands found in the Beach and Grey spectrum. There were two intense bands found at 4.4 and 5.4 eV, which were assigned to the two orbitally and spin allowed ${}^{1}\mathrm{A}_{1\mathrm{g}}(2\mathrm{t}_{2\mathrm{g}}^{6}) \rightarrow^{1} \mathrm{T}_{1\mathrm{u}}(9\mathrm{t}_{1\mathrm{u}}^{1})$ MLCT excitations. The weak shoulder found in between them at 4.8 eV was attributed to the ${}^{1}\mathrm{A}_{1\mathrm{g}}(2\mathrm{t}_{2\mathrm{g}}^{6}) \rightarrow^{1} \mathrm{T}_{2\mathrm{g}}(2\mathrm{t}_{2\mathrm{g}}^{5}, 6\mathrm{e}_{\mathrm{g}}^{1})$, however, the two weak shoulders at 3.6 and 3.9 eV on the low energy side of the first CT band were assigned as spin-forbidden but orbitally allowed ${}^{1}\mathrm{A}_{1\mathrm{g}} \rightarrow^{3} \mathrm{T}_{1\mathrm{u}}(2\mathrm{t}_{2\mathrm{g}} \rightarrow 9\mathrm{t}_{1\mathrm{u}}, 2\mathrm{t}_{2\mathrm{u}})$ CT transitions and not LF excitations as reported by Beach and Gray. It was concluded by Pierloot *et al* that the LF states lie at much higher energies than the CT states.

A theoretical study by Baerands *et al* in 1997 [106], reporting on the photodissociation of $\mathrm{Cr(CO)}_6$ as well as the spectrum, agreed with the assignment reported by Pierloot *et al* and showed that the lowest states in the spectrum did indeed have CT character. A low energy excitation (4.0 eV) was carried out based upon the calculated potential energy surface along the Cr-CO dissociation coordinate. From these results it was concluded that the LF states were too high in energy to be directly populated by irradiation at 4.0 eV raising the question as to how the molecule finds its way to dissociation from initial excitation to the non dissociative CT state. Both Baerands and Pierloot suggested that a crossing of states might be the answer.

Using pump-probe spectroscopy Fuß *et al* [98,104] inferred that the dissociation did proceed via a crossing of states. After initial excitation to the MLCT ${}^{1}\mathrm{T}_{1\mathrm{u}}$ state they found that the molecule underwent relaxation to another MLCT state where it then crossed to the dissociative LF state. The initial excitation to the CT state was found to take place within 30 fs and the transition to the LF state, to produce $Cr(CO)_5$ in its S_1 state, within 20 fs. The relaxation of $Cr(CO)_5$ was found to occur within 40 fs giving a total time of within 100 fs for the loss of the CO ligand.

Several time-resolved spectroscopic investigations [108, 109] had been carried out and the fact that the dissociation occurred at the femtosecond timescale suggested that the process may go via a conical intersection accounting for its ultrafast timescale. Fuß *et al* also found that the process from excitation to dissociation and relaxation to the ground state took 110 fs substantiating evidence that the surfaces cross with a conical intersection provided by the JT effect.

A theoretical study by Robb *et al* [99] agreed with the assignments. The study was made with particular emphasis on the product of dissociation, $Cr(CO)_5$, and the mechanism by which it relaxes to its ground state. The calculations were carried out using a CASSCF wavefunction with an active space consisting of the 4 lowest lying Cr 3d orbitals and their antibonding counterparts plus 6 valence electrons. The fifth d orbital is not required in the active space to describe the ground and lowest excited states of $Cr(CO)_5$.

It was found that, after excitation to the MLCT $^1T_{1u}$ state, $Cr(CO)_6$ dissociated on the lowest lying LF state to its S_1 state via a crossing. $Cr(CO)_5$ was then found to decay to its ground state via a JT conical intersection at a trigonal bipyramid geometry. Recently a study complementary to that of Fuß *et al* was carried out by Bartlett *et al* [110] and calculations at the equation-of-motion coupled cluster singles and doubles (EOM-CCSD) level were used. They calculated potential energy curves along the totally symmetric Cr-CO vibration mode and along the single Cr-CO bond elongation. They found that at a Cr-CO bond distance of 1.92Å, an avoided crossing was created between the $^1T_{1g}$ metal centred (MC) and $^1T_{1u}$ MLCT states. In a multi-dimensional picture this could be a CI. This feature is what facilitates the fast population of the dissociative $^1T_{1g}$ state once the initial excitation has populated the $^1T_{1u}$ state. In this study we aim to carry out further CASSCF calculations using some of the same active spaces used by Pierloot *et al* but also to use a larger active space than has been implemented in any previous work. The new calculations will mean that all of the electronic states involved in the dissociation are included in one calculation providing a more complete picture of the process than has been achieved before.

7.2 Bonding and Electronic States

In order to understand the photodissociation of the molecule a full appreciation of the bonding between the metal centre and the ligands is necessary. $Cr(CO)_6$ is an octahedral complex with 6 d-electrons located at the metal centre. The CO ligands lie symmetrically along the x-, y- and z-axes of a cartesian coordinate system. The ligand orbitals are generated by taking 6 σ-orbitals and then combining them to make 6 ligand group orbitals labelled e_g, t_{1u} and a_{1g} according to symmetry. Each ligand has 2 π orbitals available for bonding which are split into 4 triply degenerate sets of ligand group orbitals labelled by symmetry as t_{1g}, t_{1u}, t_{2g} and t_{2u}. The d_{z^2} and the $d_{x^2-y^2}$ metal orbitals point directly at the ligands and, along with the metal 4s and 4p orbitals, they form bonding and antibonding molecular orbitals with the 6 σ-orbitals of the ligands. The two molecular orbitals derived from the d_{z^2} and $d_{x^2-y^2}$ are degenerate and are denoted $5e_g$ and $6e_g^*$. The d_{xy}, d_{yz} and d_{xz} orbitals are of the right symmetry to overlap with the empty π^* orbitals on the ligands forming the $2t_{2g}$ and $3t_{2g}^*$ orbitals.

The LF states are split by a number of CT states which are lower in energy than the $6e_g^*$ state. The magnitude of the ligand field splitting of the e_g and t_{2g} orbitals can be attributed to the π backbonding of the metal d-orbitals with the empty π^* orbitals on the ligands. The filled d-orbitals can pass electron density away from the metal ion onto the ligands which offers greater stabilisation and allows the metal to accept the σ-bonds more easily. The bonding between the metal orbitals and the CO ligands and the arrangement of the MO's is shown in figure 7.2.

The electronic states are central to the photodissociation process and a good understanding of these is vital. The states of interest here are listed in table 7.1 along with their symmetry labels and their main electronic transitions. In $Cr(CO)_6$ the ground electronic state is the $^1A_{1g}$ state which is predominantly a $2t_{2g}^6$ configuration. There are selection rules which govern the transitions between the electronic states in the complex. For an electronic transition the transition moment integral has the form

Table 7.1: The important electronic states involved in the photodissociation of $Cr(CO)_6$ and their main electronic transitions.

State	Main Electronic Transition
a^1T_{2u}	$2t_{2g} \rightarrow 9t_{1u}$
b^1T_{2u}	$2t_{2g} \rightarrow 2t_{2u}$
a^1T_{1u}	$2t_{2g} \rightarrow 9t_{1u}$
a^1T_{1g}	$2t_{2g} \rightarrow 3t_{2g}$
b^1T_{1g}	$2t_{2g} \rightarrow 6e_g$
a^1T_{2g}	$2t_{2g} \rightarrow 6e_g$
b^1T_{1u}	$2t_{2g} \rightarrow 2t_{2u}$
b^1T_{2g}	$2t_{2g} \rightarrow 3t_{2g}$

$$\mu_{fi} = \langle \psi_f | \hat{\mu} | \psi_i \rangle \tag{7.1}$$

where ψ_f and ψ_i are the final and initial states respectively and $\hat{\mu}$ is the dipole moment operator. $\hat{\mu}$ can be divided into two parts, $\hat{\mu}_n$, which depends only on nuclear coordinates and $\hat{\mu}_e$, which depends only on electron coordinates. By invoking the BO approximation the total wavefunction can be written

$$\psi = \chi(R)\phi(r) \tag{7.2}$$

where $\chi(R)$ and $\phi(r)$ are the nuclear and electronic wavefunctions respectively and we can write

$$\langle \chi_f \phi_f | \hat{\mu}_e + \hat{\mu}_n | \phi_i \chi_i \rangle = \langle \chi_f | \chi_i \rangle \langle \phi_f | \hat{\mu}_e | \phi_i \rangle + \langle \chi_f | \hat{\mu}_n | \chi_i \rangle \langle \phi_f | \phi_i \rangle. \tag{7.3}$$

For electronic transitions the second term is zero as

$$\langle \phi_f | \phi_i \rangle = \delta_{if}. \tag{7.4}$$

From the orthogonality of spin wavefunctions if ϕ_f and ϕ_i have different spin states then the whole integral is equal to zero. Hence the spin rule $\Delta S = 0$. For the orbital rule the integral $\langle \phi_f | \hat{\mu}_e | \phi_i \rangle$ must be non-zero. For this to be the case the direct product

$$\Gamma \phi_f \times \Gamma \hat{\mu}_e \times \Gamma \phi_i \tag{7.5}$$

must contain the totally symmetric irreducible representation of the point group of the molecule. Assuming the ground electronic state is totally symmetric (the usual case), the final state must have the symmetry of the dipole operator. Finally if the molecule has a centre of symmetry (an inversion), as the dipole moment operator always has ungerade (u) symmetry, transitions between terms of like symmetry, g → g and u → u (g is gerade and u is ungerade), are forbidden. This is the Laporte selection rule. From equation 7.3 the integral

$$\langle \chi_f | \chi_i \rangle \tag{7.6}$$

is the Franck-Condon factor and it represents the overlap of the nuclear wavefunctions of the initial and final states. The magnitude of the overlap is reflected in the intensity of the vibronic absorption bands in the spectrum.

Upon absorption of UV radiation the complex undergoes an initial excitation to a CT state which arises from the configuration $2\mathrm{t}_{2\mathrm{g}}^5 9\mathrm{t}_{1\mathrm{u}}^1$. This is referred to as a *bright state* which simply means that it is orbitally and spin allowed. Ultimately the dissociation occurs when the repulsive LF transitions ${}^1\mathrm{A}_{1\mathrm{g}}(2\mathrm{t}_{2\mathrm{g}}^6) \rightarrow^1 \mathrm{T}_{1\mathrm{g}}(2\mathrm{t}_{2\mathrm{g}}^5, 6\mathrm{e}_{\mathrm{g}}^1)$ and ${}^1\mathrm{A}_{1\mathrm{g}}(2\mathrm{t}_{2\mathrm{g}}^6) \rightarrow {}^1\mathrm{T}_{2\mathrm{g}}(2\mathrm{t}_{2\mathrm{g}}^5, 6\mathrm{e}_{\mathrm{g}}^1)$ occur. Loss of the CO ligand can be rationalised due to the σ^* antibonding character of the $6\mathrm{e}_{\mathrm{g}}^*$ orbitals.

7.3 The CAS Space and Computational Details

In order to carry out an extensive CASSCF study of this molecule it is vital to choose the correct CAS space to yield the required information. A review of work carried out so far on this molecule shows that much work has been done at the $\mathrm{O_h}$ geometry but that calculating the CT and LF states along the dissociation coordinate has until recently not been studied in detail. The issue of computational capability is encountered in terms of the size of the CAS space and the number of orbitals that can be included. Pierloot *et al* used a set of CAS spaces chosen to include the orbitals involved in either the CT or LF transitions but were unable to include all of these orbitals in just one CAS space as this would have meant having a 19 orbital CAS space, i.e. the $(2,3)\mathrm{t_{2g}}$, $(5,6)\mathrm{e_g}$, $9\mathrm{t_{1u}}$, $2\mathrm{t_{2u}}$ and $2\mathrm{t_{1g}}$, where $(2,3)\mathrm{t_{2g}}$ means the $2\mathrm{t_{2g}}$ and the $3\mathrm{t_{2g}}$ sets of orbitals. This number of orbitals was unmanageable at the time. The CAS spaces they used were:

- CAS space A (10,10) = $(2,3)\mathrm{t_{2g}}, (5,6)\mathrm{e_g}$
- CAS space B (10,13) = $(2,3)\mathrm{t_{2g}}, (5,6)\mathrm{e_g}, 2\mathrm{t_{1g}}$
- CAS space C1 (10,13) = $(2,3)\mathrm{t_{2g}}, (5,6)\mathrm{e_g}, 9\mathrm{t_{1u}}$
- CAS space C2 (10,13) = $(2,3)\mathrm{t_{2g}}, (5,6)\mathrm{e_g}, 2\mathrm{t_{2u}}$
- CAS space D (06,12) = $(2,3)\mathrm{t_{2g}}, 9\mathrm{t_{1u}}, 2\mathrm{t_{2u}}$

CAS space A includes all orbitals needed to calculate the LF excited states with transitions $2\mathrm{t_{2g}} \rightarrow 6\mathrm{e_g}, 3\mathrm{t_{2g}}$, as does CAS space B but with the addition of the $2\mathrm{t_{1g}}$ set of orbitals it also includes all MLCT states of gerade symmetry. C1 and C2 have the basic 10 plus the $9\mathrm{t_{1u}}$ and $2\mathrm{t_{2u}}$ orbitals respectively to allow for all MLCT states of ungerade symmetry. Of course by separating the $9\mathrm{t_{1u}}$ and $2\mathrm{t_{2u}}$ orbitals there can be no mixing so another CAS space was used to include both the $9\mathrm{t_{1u}}$ and $2\mathrm{t_{2u}}$ orbitals but omitting the $(5,6)\mathrm{e_g}$.

In this study we carried out state averaged CASSCF calculations for all of these CAS spaces at the O_h geometry to calculate the excited state transition energies for the lowest lying set of CT and LF states using Gaussian 03 [111]. We were unsuccessful in finding convergence for CAS spaces B, C1 and C2 and so proceeded with just A and D.

In order to find the best basis set to be used for this molecule we calculated the VEE for the 2 lowest lying LF states using CAS space A. Four different basis sets were used, 6-31G*, LANL2DZ, SDD and Dunning TZ and using Gaussian 03 apart from the latter basis set where Molpro 2006 was used.

A set of potential energy curves along the dissociation coordinate was calculated with a state averaged CAS using spaces A and D which allows for the CT and LF states to be calculated separately. The dissociation of one of the ligands was implemented by extending the internuclear separation of one Cr-C bond along the z-axis from 2.50 Å to 5.0 Å at intervals of 0.5 Å and also for a shortening of this bond to 1.7 Å.

Although CAS spaces A and D are able to yield results for the CT and LF states separately this does not provide a full picture of the mechanism in one calculation so in order to proceed to this level a larger CAS space was implemented. Using Molpro 2006 we were able to use a (10,16) CAS space which included the orbitals $(2,3)t_{2g}$, $(5,6)e_g$, $9t_{1u}$ and $2t_{2u}$ so that all excitations which contribute to the reaction mechanism were included within the one calculation. A Dunning TZ basis set with an effective core potential (ECP) was used throughout. The ECP used was ECP10MDF which replaces 10 core electrons with a pseudopotential, M means a neutral atom is used to generate the pseudopotential and DF means fully relativistic. As the Cr-C bond is extended beyond its equilibrium geometry there is a reduction in molecular symmetry from O_h to C_{4v}. At the O_h symmetry the Abelian subgroup D_{2h} is used in all calculations and for the C_{4v} symmetry the C_{2v} Abelian subgroup is used. The geometry optimisation shown in figure 7.3 was calculated with the (10,16) CAS space using a Dunning TZ basis set with a 10 electron effective core potential and using the Molpro 2006 set of programs.

7.4 Results and Discussion

7.4.1 Choice of Basis Set and Geometry Optimisation

VEE for the two lowest lying sets of LF states, b^1T_{1g} and a^1T_{2g}, were calculated at the O_h geometry for the 4 different basis sets with CAS space A. Table 7.2 shows the energies obtained for these states which correspond to electronic transitions from the $2t_{2g}$ set of orbitals to the $6e_g$ set of orbitals. It can be seen from the data that the Dunning TZ basis set provides the lowest energies at 4.83 and 5.67 eV and we continue to use this basis set throughout the study.

Table 7.2: Vertical excitation energies for the LF states corresponding to the $2t_{2g} \rightarrow 6e_g$ transition for various basis sets.

	6-31G*	LANL2DZ	SDD	Dunning TZ
b^1T_{1g}	4.96	4.87	5.09	4.83
a^1T_{2g}	5.92	5.80	6.02	5.67

The geometry optimisation calculated at the CASSCF level with the (10,16) CAS space and Dunning TZ basis set was found to show good agreement with experimental neutron diffraction data and has the following values Cr-C = 1.94 (1.91) Å and C-O 1.14 (1.14) Å, figure 7.3, experimental values are shown in brackets [112]. This optimised geometry was used in all further calculations.

7.4.2 Vertical Excitation Energies

The VEE for the low lying singlet states were calculated at the CASSCF level with CAS spaces A and D and with the larger (10,16) CAS space. Using the larger CAS space

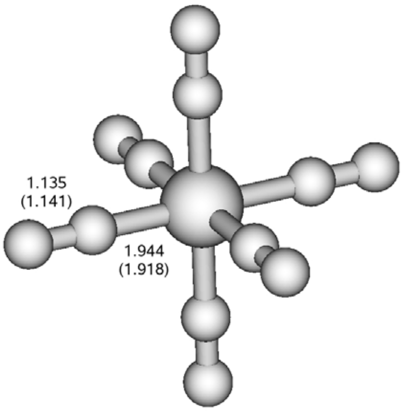

Fig. 7.3: CASSCF optimised geometry of $Cr(CO)_6$. Experimental bond lengths given in brackets [112].

we were able to calculate the MLCT transitions $a^1A_{1g} \rightarrow a^1T_{2u}$ and $a^1A_{1g} \rightarrow a^1T_{1u}$ at 4.53 and 5.42 eV and the MC transitions for $a^1A_{1g} \rightarrow b^1T_{1g}$, $a^1A_{1g} \rightarrow a^1T_{2g}$ and $a^1A_{1g} \rightarrow a^1T_{1g}$ at 4.96, 5.69 and 6.21 eV respectively. Using the (06,12) CAS space the $a^1A_{1g} \rightarrow a^1T_{2u}$ was calculated at 4.21 eV and using the (10,10) CAS space the $a^1A_{1g} \rightarrow b^1T_{1g}$ and $a^1A_{1g} \rightarrow a^1T_{2g}$ transitions were calculated at 4.82 and 5.67 eV, with both smaller CAS spaces showing good agreement with the larger one. It must be observed that the VEE given by the smaller CAS spaces are lower than those given by the larger one. This, therefore, suggests that by including the extra orbitals in the larger active space the description of the ground state has been improved to a greater extent than that of the excited states, thus bringing the ground state energy down and increasing the energy gap between the ground and excited states. This suggests that to obtain an improved description of the excited states that the active space needs to include even more orbitals.

VEE from previous studies at the DFT, CASSCF, CASPT2 and EOM-CCSD levels of theory are reported in table 7.3. By comparing the energies obtained here with those from the previous CASSCF study by Pierloot *et al* we find that the results from this study show significantly lower VEE. Pierloot *et al* used CAS spaces C1-D to calculate the a^1T_{2u} and a^1T_{1u} CT states and CAS space B for the b^1T_{1g}, a^1T_{2g} and a^1T_{1g} LF

Table 7.3: Vertical excitation energies to CT, a^1T_{2u} and a^1T_{1u}, and LF, b^1T_{1g}, a^1T_{2g} and a^1T_{1g}, states compared with DFT calculations made by [1] Baerands *et al* [106], CASSCF and CASPT2 calculations by [2] Pierloot *et al* [105] and [3]EOM-CCSD calculations by Bartlett *et al* [110].

	DFT[1]	CASSCF[2]	CASPT2[2]	EOM-CCSD[3]	(10,10)CAS	(10,16)CAS	(06,12)CAS
a^1T_{2u}	4.0	5.18 – 5.26	3.56 – 3.70	4.50		4.53	4.21
b^1T_{1g}	5.20	5.66	4.85		4.82	4.96	
a^1T_{2g}	6.30	6.42	5.08	5.50	5.67	5.69	
a^1T_{1g}		6.80	5.02	5.09		6.21	
a^1T_{1u}	5.60	5.97 – 6.15	4.11 – 4.54	5.06		5.42	

states and a contracted ANO type basis set throughout. The smaller size of these CAS spaces is some justification for the higher energies but the fact that the (06,12) and (10,10) CAS spaces used in our study also show lower energies can be attributed to basis set effects.

Pierloot *et al* also carried out CASPT2 calculations where the CASSCF wavefunctions were used as reference for the CASPT2. These results show lower energies compared with the CASSCF where dynamic correlation is not accounted for although there is some good agreement with the (10,16) CAS space especially for states $\mathrm{b}^1\mathrm{T}_{1\mathrm{g}}$ where the difference is just 0.11 eV.

The most recent study carried out is that of Bartlett *et al* in which the calculations were carried out at the EOM-CCSD level. This is a single determinant non variational based method where the determinant is constructed from HF MO's and is then operated on by an excitation operator to produce a linear combination of excited Slater determinants. Their results are comparable with those of the (10,16) CAS space but not as low as the CASPT2. The fact that the EOM-CCSD wavefunction contains excited determinants means that it does account for dynamic correlation but does not include static correlation which becomes important for dissociation and can lead to over estimated energies.

The ordering of the states found in each of these studies is reported in table 7.4. The first observation is that not all the studies find the same states. The DFT study by Baerands *et al* does not include the a^1T_{1g} LF state and the EOM-CCSD study by Baerands *et al* does not include the b^1T_{1g} LF state. The DFT method is based on single excitations only and, therefore, may not calculate states with double excitations. Both CASSCF studies are in agreement as to the ordering and the number of states. The CASPT2 results show a change in the ordering with respect to the CASSCF where the b^1T_{1g} and a^1T_{1u} states have swapped around, as have the a^1T_{1g} and a^1T_{2g}.

Table 7.4: Ordering of the CT and LF states taken from the vertical excitation energies in table 7.3

DFT[1]	CASSCF[2]	CASPT2[2]	EOM-CCSD[3]	(10,16)CASSCF
a^1T_{2u}	a^1T_{2u}	a^1T_{2u}	a^1T_{2u}	a^1T_{2u}
b^1T_{1g}	b^1T_{1g}	a^1T_{1u}	a^1T_{1u}	b^1T_{1g}
a^1T_{1u}	a^1T_{1u}	b^1T_{1g}	a^1T_{1g}	a^1T_{1u}
a^1T_{2g}	a^1T_{2g}	a^1T_{1g}	a^1T_{2g}	a^1T_{2g}
…	a^1T_{1g}	a^1T_{2g}	…	a^1T_{1g}

All of the studies are in agreement that the a^1T_{2u}, corresponding to transitions from the $2t_{2g}$ orbitals to the $9t_{1u}$ orbitals, is the lowest lying state. This has now become a well established result and is contrary to the first reported spectrum by Beach and Gray. From these results it is not possible to draw definite conclusions as to the ordering of the states but we can say that the calculations carried out in this study offer the first CAS space that is balanced for all of the electronic states involved in the reaction.

Comparisons have been made with experimental data from Beach and Gray by Bartlett *et al.* They assign the shoulder at 3.9 eV to the transition to the a^1T_{2u} state, the intense bands at 4.46 and 5.53 eV to the a^{1}T$_{1u}$ and b^{1}T$_{1u}$ states as do Pierloot *et al* and Baerands *et al* and the shoulder at 4.87 eV to the a^{1}T$_{2g}$ state. In this study we have found that the b^{1}T$_{1g}$ state lies at 4.96 eV, (10,16) CAS space, and 4.82 eV, (10,10) CAS space, which is in good agreement with the CASPT2 results from Pierloot *et al* at 4.85 eV. We would, therefore, not assign the shoulder at 4.87 eV to the a^{1}T$_{2g}$ state as Bartlett *et al* did but to this b^{1}T$_{1g}$ state. We find that Pierloot *et al* also thought that there was some uncertainty in assigning this weak shoulder and they concluded that it could be due to the b^{1}T$_{1g}$ state or could be due to a superposition of both the b^{1}T$_{1g}$ and a^{1}T$_{2g}$ states.

7.4.3 Potential Energy Curves

All calculations for the PEC's were carried out using the Molpro 2006 set of programmes and convergence was achieved for CAS spaces A and D and for the much larger (10,16) CAS space all the way along the dissociation coordinate. Figure 7.4 shows the PEC's calculated for the lowest lying CT and LF states with the (10,16) CAS space. These states have been plotted as adiabatic states which means that the character of the states is not consistent as they proceed along the dissociation coordinate. At the octahedral geometry there are two sets of triply degenerate CT states lying at 4.53 and 5.42 eV above the ground state and a set of triply degenerate LF states at 4.96 eV above the ground state. The CT states correspond to the ^{1}A$_{1g}$ → a^{1}T$_{2u}$ and ^{1}A$_{1g}$ → a^{1}T$_{1u}$ transitions and the LF states to the ^{1}A$_{1g}$ → b^{1}T$_{1g}$ transition. The a^{1}T$_{2u}$ state is a *bright* state and is populated on initial excitation of the molecule.

As the Cr-C bond length is extended the symmetry of the molecule is reduced from O$_h$ to C$_{4v}$ and the CT and LF states are split from being triply degenerate to a single state and a doubly degenerate set of states. The symmetry of the CT states changes to A$_1$ and E and the LF to A$_2$ and E within the Abelian subgroup C$_{4v}$. It can be seen in this plot that when the Cr-C bond is at about 2.1 Å that there is a crossing of the LF and CT states. In order to analyse what is happening at this point the states must

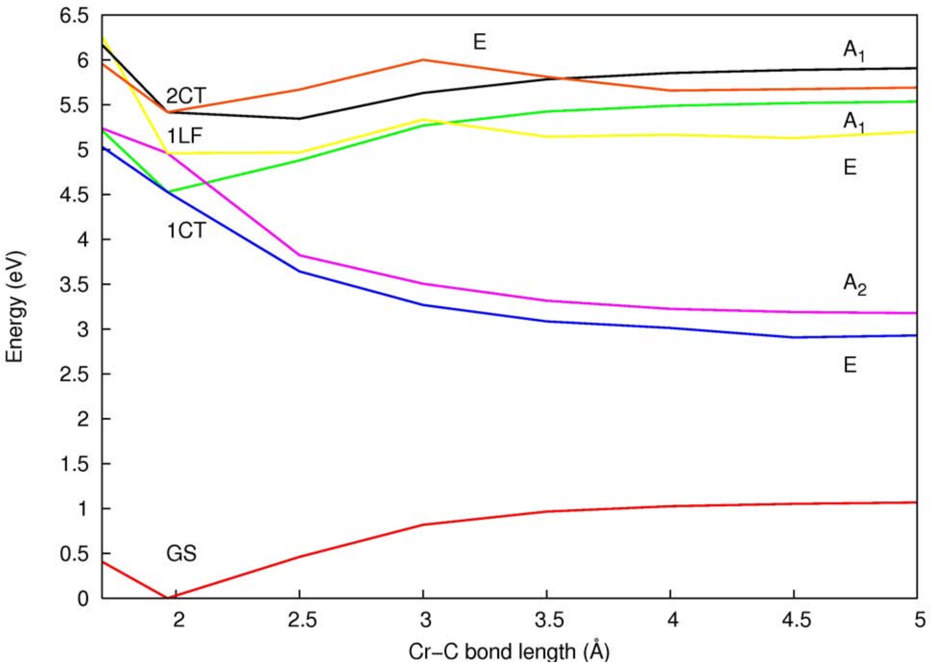

Fig. 7.4: Adiabatic potential energy curves along the dissociation coordinate of $Cr(CO)_6$ at the CASSCF level with a (10,16) CAS space.

be fully characterised. At a Cr-C bond length of 3 Å there are obvious kinks in the LF state with E symmetry and the 2nd CT state with E symmetry. This would indicate a change of character within the states and can be illustrated more clearly by plotting diabatic states where the character is maintained.

Figure 7.5 is a plot of the diabatic states where their character is maintained along the dissociation coordinate. The dotted lines illustrate where a change in character has occurred due to an intruder state mixing in that has not been calculated in this study. It is now possible to see exactly what is happening where the CT and LF states cross. As soon as the Cr-C bond length is extended to about 2.1 Å it can be seen that the states cross and that the lowest lying state is of b^1T_{1g} and, therefore LF, character. This means that after initial excitation to the a^1T_{2u} CT state the molecule can find its way to the LF state after only a small extension of the Cr-C bond length. This is also justification for the ultrafast timescale.

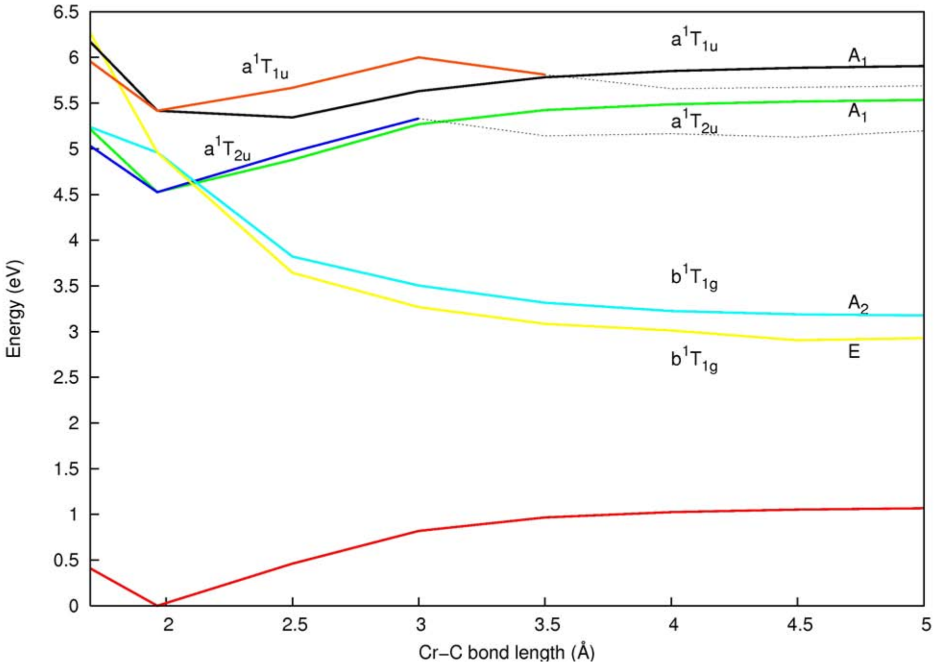

Fig. 7.5: Diabatic potential energy curves along the dissociation coordinate of $Cr(CO)_6$ at the CASSCF level with a (10,16) CAS space.

Figure 7.6 is a plot of the adiabatic states calculated with the (10,10), (06,12) and the (10,16) CAS spaces along the dissociation coordinate. The lowest lying LF and only the first set of CT states are shown for the (10,16) CAS space for comparison with the smaller CAS spaces. The states have been plotted so that the lowest energy point is at zero for each CAS space. The states for the two smaller CAS spaces would all shift upwards if the true energy were plotted. The CT states generated by the (06,12) CAS space, although separated by only 0.05 eV, are not triply degenerate as they are with the (10,16) CAS space. The (06,12) CAS space does not include any of the e_g orbitals and, therefore, it must be concluded that contributions from these orbitals are necessary in describing the a^1T_{2u} CT states.

At a Cr-C bond length of 2.5 Å the LF states of the (10,10) CAS are kinked indicating the loss of b^1T_{1g} character and the presence of intruder states. At this geometry the smaller CAS spaces become unstable which makes the states impossible

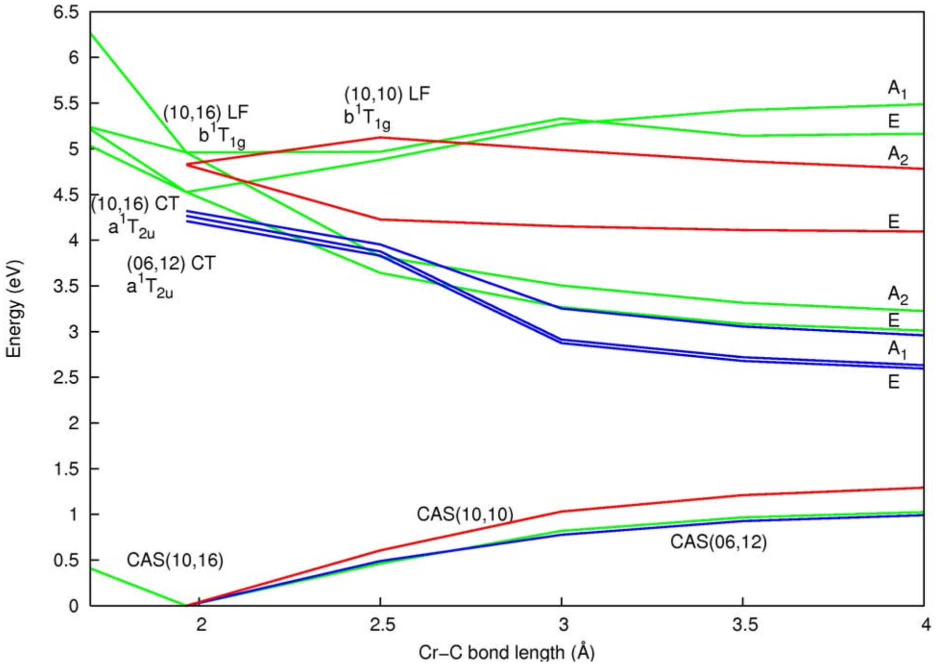

Fig. 7.6: Potential energy curves along the dissociation coordinate of $Cr(CO)_6$ for the (06,12), (10,10) and (10,16) CAS spaces.

to characterise. Likewise the (06,12) CT states suffer from the same problem and are not smooth at all away from the equilibrium geometry. We also note that as the LF states of the (10,16) CAS space split into the E and A_2 symmetries that the A_2 state is lower in energy than the E but that for the LF states of the (10,10) CAS space it is the E states that are lower in energy than the A_2 states.

These results clearly show that the smaller CAS spaces are significantly more unstable than the larger one away from the equilibrium geometry. From figure 7.5 it can be seen that out of the nine states calculated with the (10,16) CAS space, seven of them maintain their character all the way along the dissociation coordinate whilst the smaller CAS spaces suffer from intruder state problems at only a 0.5 Å extension of the Cr-C bond length.

7.5 Conclusions

In this study we have carried out detailed CASSCF calculations on $Cr(CO)_6$ and compared the results with previous studies done at the DFT, CASSCF, CASPT2 and EOM-CCSD levels of theory. It has been shown in this study that results vary with different basis sets but that the choice of CAS space has a significant effect on the results. A very large CAS space which includes all the orbitals to allow for the CT and LF transitions involved in the dissociation is computationally very expensive but is necessary in order to produce results in which the PEC's are smooth and can be characterised away from the equilibrium geometry. The (10,16) CAS space used in this study is the smallest space that can reasonably be used in an attempt to describe the photodissociation of $Cr(CO)_6$. We see an increase in VEE from the smaller active spaces to the larger one suggesting that more orbitals would need to be included to obtain an overall improvement to both the ground and excited states. Perhaps transitions to the $2t_{1g}$ set of orbitals contribute to the excited states. The results compare well with other levels of theory with regard to VEE and with the states that were found. The ordering of the states shows agreement with previous CASSCF studies and our results here agree that the lowest lying states are not LF states but that they are CT states into which initial excitation occurs.

The smaller CAS spaces, (10,10) and (06,12) give reasonable results at the O_h geometry and the energies are comparable with larger CAS spaces but when moving along the dissociation coordinate these smaller CAS spaces become unstable and suffer from intruder state problems at a short distance away from the equilibrium geometry. The relatively small size of these CAS spaces means that they do not have the flexibility to allow for a mixing in of states.

The results show that even with a very large CAS space the VEE are marginally higher than those achieved at the CASPT2 level of theory and we also observe a rearrangement in the ordering of the states. The higher excitation energies for the

CASSCF are justified by the lack of dynamic correlation which is accounted for in the CASPT2 method.

It has been found in this study that the lowest lying set of LF states is the b^1T_{1g} which shows agreement with previous calculations carried out at the CASPT2, DFT and CASSCF level. These results are not in agreement with the most recent study on $Cr(CO)_6$. Using EOM-CCSD calculations the a^1T_{2g} was found to be lowest energy state for transitions to the $6e_g$ set of orbitals where dissociation takes place. Our results show that there is a crossing between the CT and LF states and this supports experimental findings.

A natural progression for this CASSCF study would have been to carry out CASPT2 calculations using the (10,16) CAS space as a reference. The CASPT2 method is computationally more demanding than the CASSCF and was not possible with our current computational capabilities on even the smaller CAS spaces. In conclusion the instability of CASSCF for this study is evident and this means that a very large CAS space must be used but for energetically quantitative results CASPT2 is the best method.

Ultimately the aim for developing this work further would be to add more DOF and carry out a dynamics study for the molecule. A computationally demanding task but such a study would certainly enable this reaction mechanism to be explored on a new level.

Chapter 8

Conclusions

Ultrafast photodissociation occurs on the femtosecond timescale and is a process which exhibits complex behaviour due to coupling between the electronic and nuclear motions (vibronic coupling). As a consequence of this coupling CI are often a feature of the PES producing pathways for ultrafast radiationless decay. In this thesis we have closely studied the mechanisms of three different systems which undergo photodissociation. An accurate simulation of these processes is underpinned by the quality of the calculated PES.

The results obtained from wavepacket dynamics calculations offer a rigorous test of the accuracy of a PES. In particular, the absorption spectrum for a molecule obtained from the dynamics is one observable that when compared with experimental results gives a measure of the level of accuracy within the surfaces. Once the PES has been obtained, dynamical information can be calculated. Examples of this are timescales for the dissociation, branching ratios to determine the importance of different channels, and mechanistic information that shows the path followed.

The first system studied was ammonia. This is a well-studied, simple, molecule with topological features on the PES that make it an ideal candidate for dynamical studies. The excited electronic state ($\tilde{A}^1A_2''$) is quasibound with a trigonal planar (D_{3h}) minimum in the Franck-Condon region. Beyond a small energy barrier in the early part of the H-NH_2 dissociation coordinate there lies a CI between the ground ($\tilde{X}^1A_1'$) and first excited state. The reaction proceeds either adiabatically in the first excited state or non-adiabatically via the CI in the ground state. A four atom molecule such as NH_3 possesses 6 normal modes and, therefore, 15 sets of couplings. Such a large system takes us to the limit of quantum dynamics capabilities.

NH_3 was investigated by using two different models, a 2D and a 6D model. The 2D model provided us with a good simulation of the umbrella mode and allowed us to carry out extensive wavepacket dynamics without being too computationally demanding. For this reason we were able to set many parameters in preparation for our 6D model as trial calculations were not practical for such a large system. The 6D model surpasses any previous work carried out on this system in its ability to describe the molecule and in terms of the dynamics. Its improved level of accuracy over the 2D model becomes evident when we look at a plot of the excited state surface in R and ϕ and see that the CI is much more well defined in the 6D description.

Using the coupled PES from Truhlar *et al* [72,73] and carrying out dynamics across the whole surface we were able to show that dissociation occurs on both the first excited $\tilde{A}$ state and on the ground $\tilde{X}$ state via the CI. Two different dynamics calculations were carried out using the 2D model, one from the relaxation of the wavepacket into both wells of the double minimum and one from relaxation into a single well. Although we did not reproduce the experimental absorption spectrum we were able to demonstrate the origin of the peaks exhibited in the spectrum which was generated from the dynamics of the wavepacket from one well. The spectrum consists of two sets of peaks, one of which is due to excitation of a wavepacket from the ψ_0 vibrational state and one due to excitation from the ψ_1 vibrational state.

To calculate the dynamics of the 6D model we needed to get the PES function in a suitable form. For this we used a multi-reference HDMR function. Even using efficient MCTDH wavepacket propagation methods, simulations were very computationally expensive.

The spectrum generated from these 6D dynamics exhibited more than one frequency which we attributed to our calculations being in their preliminary stages. Convergence for the 6D dynamics calculations could have been achieved by increasing the number of SPFs. From experience we can conclude that the calculations should have provided a good basis but it is difficult to quantify how many more SPFs would need to be added for convergence.

The main results from our simulations were calculated branching ratios. Although previous studies have investigated the competition between the two routes to dissociation they have not produced branching ratios. Our results showed that the dissociation takes place mostly in the excited state in both models. We found that dissociation was substantially more rapid in the 6D model, by 40 fs a large portion of the wavepacket had dissociated, figure 4.17. After 40 fs the norm for the 2D model was 0.99 and for the 6D 0.70.

The second system, FNO has surprisingly complicated dynamics. After photoexcitation to the first excited state the wavepacket bifurcates, part dissociates along the NF channel and part is trapped in a shallow well within the NO channel giving rise to the main progression in the spectrum. As it is only a triatomic, the full quantum dynamics are possible. The difficulty is obtaining accurate PES on which to carry out the dynamics.

By calculating the PES for FNO using electronic structure theory we have shown how sensitive the system is to these methods. Such a thorough investigation of the surfaces has not been carried out before and in this study we have successfully produced 3 dimensional surfaces for the ground and first four excited states using the CASSCF, MS-MR-CASPT2 and MRCI methods. The previous study by Schinke *et al* only included the NO and NF bond lengths and the angular DOF was omitted. We have, therefore, by introducing the FNO angle produced a more complete description of the dissociative process.

Using a full valence active space for the CASSCF calculations produced smooth but energetically inaccurate surfaces whilst the MRCI and MS-MR-CASPT2 methods were not well behaved at large N-F bond distances. After carrying out the wavepacket dynamics on the 3D surfaces we found that there was a substantial amount of direct dissociation which yielded a broad spectrum. By fixing the angle at its equilibrium geometry and placing the wavepacket onto the excited state as Schinke did we found that we were successful in reproducing some of the main features of the spectrum. This also enabled us to explore the sensitivity of the excited state surface by altering the initial position of the wavepacket by very small amounts. We found that this had a large effect on the dynamics and that the spectrum was altered substantially by these small changes.

To compensate for this sensitivity, we set up a model Hamiltonian with parameters that can be adjusted to reproduce the experiment. From our calculations we have concluded that certain topological features in the $1^1A''$ excited state are difficult to reproduce with a single model surface.

The coupling between the excited states of A'' symmetry has not been considered in any previous work and in this study we have presented a fully coupled model Hamiltonian. After calculating the non-adiabatic coupling between several of the excited states we found that the $1^1A''$ state was strongly coupled to the $2^1A''$ excited state and $4^1A''$ excited states. Using a potential fit of the MS-MR-CASPT2 *ab initio* data including these three states and the coupling between them, the shallow well in the $1^1A''$ does indeed become apparent as a direct result of the coupling. For the fitted surfaces to be energetically accurate it was necessary to adjust the parameters for the VEE and dissociation energy. We found that by adjusting the coupling between the $1^1A''$ and $4^1A''$ states that the depth of the well in the $1^1A''$ state could be increased.

The final system investigated was $Cr(CO)_6$. On photoexcitation this molecule undergoes ultrafast photodissociation via a number of surface crossings between the CT and LF states. A large molecule with many low lying electronic states made this a challenging prospect to study. Our computational facilities enabled us to carry out CASSCF calculations using a larger active space than had previously been used. We were able to include all of the orbitals of interest in one calculation by using a 10 electron 16 orbital active space. By carrying out CASSCF calculations with smaller active spaces we were able to conclude that the (10,16) active space was the minimal from which reasonable results could be obtained.

From these calculations we conclude that we have produced a more complete picture of the reaction than has been achieved before. By extending one of the Cr-CO bonds to dissociation we calculated potential energy curves along the dissociation coordinate for the ground and 6 excited states. We found agreement with previous CASSCF work with regard to the ordering of the states in terms of VEE, but disagree with the ordering obtained by other methods such as the EOM-CCSD used in the most recent study. We have shown that there is a crossing between the CT and LF states which supports experimental findings.

We have shown in this thesis some of the challenges facing the computational chemist with regard to achieving high levels of accuracy in simulations. There are many contributing factors to take into account in a study such as this. The choice of coordinates, the types of method to be used are all important, but good PES are essential and are not easily obtained for excited states.

The work presented in this thesis will provide the starting point for further studies on all three molecules. The 6D calculations for NH_3 are in their infancy and more work is needed to converge the calculations but with such a large system these simulations are computationally time consuming. This will, however allow this prototypical reaction to be studied in great detail. The FNO potential fit provided fully coupled surfaces and with more well practised adjustments of the parameters it is highly possible that the experimental spectrum will be reproduced.

We have tried to provide a description of the dissociation mechanism in terms of coupled diabatic states to show the competition between the bound and dissociative parts of the wavepacket and this will help to understand the dynamics.

A natural progression for $Cr(CO)_6$ would be to carry out MS-MR-CASPT2 calculations to account for electron correlation and to solve the problem of state-ordering. Fitting the surfaces along the important normal modes and carrying out wavepacket dynamics would enable a more detailed analysis of how this reaction proceeds and exactly which states are involved.

Bibliography

[1] Müller, R. *A brief history of stratospheric ozone research*. Meteorologische Zeitschrift, 2009. **18**, 3–24.

[2] McConnell, J. C. & Jin, J. J. *Stratospheric ozone chemistry*. Atmosphere-ocean, 2008. **46**, 69–92.

[3] Zewail, A. H. *Femtochemistry: Atomic-scale dynamics of the chemical bond using ultrafast lasers(Nobel lecture)*. Angew. Chem. Int. Ed., 2000. **39**, 2586–2631.

[4] Zewail, A. H. *Laser femtochemistry*. Science, 1988. **242**, 1645–1653.

[5] Rose, T. S., Rosker, M. J., & Zewail, A. H. *Femtosecond real-time observations of wave packet oscillations (resonance) in dissociation reactions*. J Chem. Phys., 1988. **88**, 6672–6673.

[6] Roberts, G. & Zewail, A. H. *Femtosecond real-time probing of reactions. 7. A quantum and classical mechanical study of the ICN dissociation experiment*. J. Phys. Chem., 1991. **95**, 7973–7993.

[7] Ling, J. H. & Wilson, K. R. *Photofragment spectrum of ICN*. J. Chem. Phys., 1975. **63**, 101–109.

[8] Hess, W. P. & Leone, S. R. *Absolute I^* quantum yields for the ICN $\tilde{A}$ state by diode laser gain-vs-absorption spectroscopy*. J. Chem. Phys., 1987. **86**, 3773–3780.

[9] Scherer, N. F., Knee, J. L., Smith, D. D., & Zewail, A. H. *Femtosecond photofragment spectroscopy: The reaction ICN → CN + I*. J. Phys. Chem., 1985. **89**, 5141–5143.

[10] Yarkony, D. R. *Diabolical conical intersections*. Rev. Mod. Phys., 1996. **68**, 985–1013.

[11] Robb, M. A., Garavelli, M., Olivucci, M., & Bernardi, F. *A computational strategy for organic photochemistry*. In Lipkowitz, K. & Boyd, D., editors, *Reviews in Computational Chemistry*, volume 15. John Wiley and sons, New York, 2000 pages 87–146.

[12] Baer, M. & Billing, G. D., editors. *The role of degenerate states in chemistry*, volume 124 of *Adv. Chem. Phys*. John Wiley, New Jersey, U.S.A, 2002.

[13] Domcke, W., Yarkony, D. R., & Köppel, H., editors. *Conical intersections: Electronic structure, dynamics and spectroscopy*. World Scientific, Singapore, 2004.

[14] Worth, G. A. & Cederbaum, L. S. *Beyond Born-Oppenheimer: Conical intersections and their impact on molecular dynamics*. Ann. Rev. Phys. Chem., 2004. **55**, 127–158.

[15] Manthe, U., Meyer, H. D., & Cederbaum, L. S. *Wavepacket dynamics within the multiconfiguration hartree framework: General aspects and application to NOCl*. J. Chem. Phys., 1992. **97**, 3199–3213.

[16] Zewail, A. H. *Femtochemistry: Atomic-scale dynamics of the chemical bond*. J. Phys. Chem. A., 2000. **104**, 5660–5694.

[17] Schinke, R., Nonella, M., Suter, H. U., & Huber, J. R. *Photodissociation of ClNO in the S_1-state: A quantum mechanical ab initio study*. J. Chem. Phys., 1990. **93**, 1098.

[18] Staemmler, V. & Palma, A. *CEPA calculations of potential energy surfaces for open-shell systems. IV. photodissociation of* H_2O *in the* ${}^{1}_{A}B_1$ *state*. Chem. Phys., 1985. **93**, 63–69.

[19] Heumann, B., Düren, R., & Schinke, R. *Ab initio calculation of the two lowest excited states of* H_2S *relevant for the photodissociation in the first continuum.* Chem. Phys. Lett., 1991. **180**, 583–588.

[20] Nonella, M. & Huber, J. R. *Photodissociation of methylnitrite: an mc scf calculation of the* S_1 *potential surface*. Chem. Phys. Lett., 1986. **131**, 376–379.

[21] Nonella, M., Huber, J. R., Untch, A., & Schinke, R. *Photodissociation of* CH_3ONO *in the first absorption band : A three-dimensional classical trajectory study*. J. Chem. Phys., 1989. **91**, 194–204.

[22] Amatatsu, Y., Morokuma, K., & Yabushita, S. *Ab initio potential energy surfaces and trajectory studies of A-band photodissociation dynamics:* $CH_3I^* \rightarrow CH_3 + I$ *and* $CH_3 + I^*$.. J. Chem. Phys., 1991. **94**, 4858.

[23] Sarma, M., Adhikari, S., & Mishra, M. K. *Selective photodissociation of O-H and O-D bonds from ground vibrational state of HOD using simple UV pulses*. J. Chem. Phys., 2007. **127**, 024,305–1–024,305–5.

[24] Sarma, M. & Mishra, M. K. *Role of photolysis frequency in enhanced selectivity and yield for controlled bond breaking in HOD*. J. Phys. Chem., 2008. **112**, 4895–4905.

[25] Sinha, A., Hsiao, M. C., & Crim, F. F. *Bond-selected bimolecular chemistry:* $H + HOD(4_{\nu)_{OH}}) \rightarrow OD + H_2$. J. Chem. Phys., 1990. **92**, 6333–6335.

[26] Imre, D. G. & Zhang, J. *Dynamics and selective bond breaking in photodissociation*. Chem. Phys., 1989. **139**, 89–121.

[27] Henriksen, N. E. *Theoretical concepts in molecular photodissociation dynamics*. Adv. Chem. Phys, 1995. **91**, 433–509.

[28] Fajer, J. *Chlorophyll chemistry before and after crystals of photosynthetic reaction centers*. Photosynth. Res., 2004. **80**, 165–172.

[29] Zouni, A., Witt, H.-T., Kern, J., Fromme, P., Krauss, N., Saenger, W., & Orth, P. *Crystal structure of photosystem II from Synechococcus elongatus at 3.8ÅA resolution*. Nature, 2001. **409**, 739–743.

[30] Eberhard, S., Finazzi, G., & Wollman, F. A. *The dynamics of photosynthesis*. Ann. Rev. Gen., 2008. **42**, 463–515.

[31] Olaso-González, G., Merchán, M., & Serrano-Andrés, L. *Ultrafast electron transfer in photosynthesis: Reduced pheophytin and quinone interaction mediated by conical intersections*. J. Phys. Chem. B, 2006. **110**, 24,734–24,739.

[32] Abe, M., Ohtsuki, Y., Fujimura, Y., & Domcke, W. *Optimal control of ultrafast cis-trans photoisomerization of retinal in rhodopsin via a conical intersection*. J. Chem. Phys., 2005. **123**, 144,508–1–144,508–10.

[33] Schoenlein, R. W., Peteanu, L. A., Mathies, R. A., & Shank, C. V. *The first step in vision: Femtosecond isomerization of rhodopsin*. Science, 1991. **254**, 412–415.

[34] Nonella, M. *Electrostatic protein-chromophore interactions promote the all-trans → 13-cis isomerization of the protonated retinal schiff base in bacteriorhodopsin: An ab initio CASSCF/MRCI study*. J. Phys. Chem. B, 2000. **104**, 11,379–11,388.

[35] Hahn, S. & Stock, G. *Quantum-mechanical modelling of the femtosecond isomerization in rhodopsin*. J. Phys. Chem. B, 2000. **104**, 1146–1149.

[36] Köppel, H., Domcke, W., & Cederbaum, L. S. *Multimode molecular dynamics beyond the Born-Oppenheimer approximation*. Adv. Chem. phys., 1984. **57**, 59–246.

[37] Born, M. & Oppenheimer, R. *Quantum theory of molecules*. Ann. Phys., 1927. **84**, 457–484.

[38] Born, M. & Huang, K. *The Dynamical Theory of Crystal Lattices*. Oxford University Press, Oxford, U.K., 1954.

[39] Cederbaum, L. S., Domcke, W., Köppel, H., & von Niessen, W. *Strong vibronic coupling effects in ionization spectra: The "mystery band" of butatriene*. Chem. Phys., 1977. **26**, 169–177.

[40] Cattarius, C., Worth, G. A., Meyer, H. D., & Cederbaum, L. S. *All mode dynamics at the conical intersection of an octa-atomic molecule: Multi-configuration time-dependent Hartree (MCTDH) investigation on the butatriene cation*. J. Chem. Phys, 2001. **115**, 2088–2100.

[41] Mahapatra, S., Worth, G. A., Meyer, H.-D., Cederbaum, L. S., & Köppel, H. *The* $\tilde{A}^2\mathrm{E}/\tilde{B}^2\mathrm{B}_2$ *photoelectron bands of allene beyond the linear coupling scheme: An ab initio dynamical study including all fifteen vibrational modes*. J. Phys. Chem. A, 2001. **105**, 5567–5576.

[42] Döscher, M. & Köppel, H. *Multiple surface intersections and strong nonadiabatic coupling effects between the* $\tilde{D}^2E_{1u}$ *and* $\tilde{E}^2B_{2u}$ *states of* $C_6H_6^+$. Chem. Phys, 1997. **225**, 93–105.

[43] Worth, G. A., Beck, M. H., Jäckle, A., & Meyer, H.-D. *The Heidelberg MCTDH Package: A set of programs for multi-dimensional quantum dynamics. User's Guide, Version 8*, 2000

(The User's Guide can be downloaded from the URL: http://www.pci.uni-heidelberg.de/tc/usr/mctdh/).

[44] Mahapatra, S., Chakrabarti, N., & Sathyamurthy, N. *Time correlation function and its unifying role in molecular structure and dynamics*. Int. Rev. Phys. Chem., 1999. **18**, 235–262.

[45] Cohen, L. *Time frequency-distributions-A review*. Proc. Inst. Elect. Electron. Engrs., 1989. **77**, 941–981.

[46] Roothan, C. C. J. *New developments in molecular orbital theory*. Rev. Mod. Phys., 1951. **23**, 69–89.

[47] Werner, H.-J. & Knowles, P. J. *A Second Order Multiconfiguration SCF Procedure with Optimum Convergence*. J. Chem. Phys., 1985. **82**, 5053–5063.

[48] Knowles, P. J. & Werner, H. J. *An efficient method for the evaluation of coupling coefficients in configuration interaction calculations*. Chem. Phys. Lett., 1988. **145**, 514–522.

[49] Celani, P. & Werner, H.-J. *Multireference perturbation theory for large restricted and selected active space reference wave functions*. J. Chem. Phys., 2000. **112**, 5546–5557.

[50] Werner, H.-J. *Third-order multireference perturbation theory The CASPT3 method*. Mol. Phys., 1996. **89**, 645–661.

[51] Andersson, K. & Roos, B. O. *Multiconfigurational 2nd-order perturbation theory-A test of geometries and binding energies*. Int. J. Quantum Chem., 1993. **45**, 591–607.

[52] Pierloot, K., Persson, B. J., & Roos, B. O. *A theoretical study of the chemical bonding in* $M(CO)_x$ *(M=Cr,Fe and Ni)*. J. Chem. Phys., 1994. **101**, 6810–6821.

[53] Pierloot, K., Persson, B. J., & Roos, B. O. *Theoretical Study of the Chemical Bonding in* $[Ni(C_2H_4)]$ *and Ferrocene*. J. Phys. Chem., 1995. **99**, 3465–3472.

[54] Roos, B. O. & Andersson, K. *Multiconfigurational perturbation theory with level shift - the* Cr_2 *potential revisited*. Chem. Phys. Lett., 1995. **245**, 215–223.

[55] Kosloff, R. & Tal-Ezer, H. *A direct relaxation method for calculating eigenfunctions and eigenvalues of the Schrödinger equation on a grid*. Chem. Phys. Lett., 1986. **127**, 223.

[56] Beck, M. H., Jäckle, A., Worth, G. A., & Meyer, H.-D. *The multiconfiguration time-dependent Hartree method: A highly efficient algorithm for propagating wavepackets*. Phys. Rep., 2000. **324**, 1–105.

[57] Meyer, H.-D. & Worth, G. A. *Quantum molecular dynamics: propagating wavepackets and density operators using the multiconfiguration time-dependent Hartree method*. Theor. Chem. Acc., 2003. **109**, 251–267. Feature article.

[58] Dickinson, A. S. & Certain, P. R. *Calculation of matrix elements for one-dimensional quantum-mechanical problems*. J. Chem. Phys., 1968. **49**, 4209.

[59] Jäckle, A. & Meyer, H.-D. *Time-dependent calculation of reactive flux employing complex absorbing potentials: General aspects and application within MCTDH*. J. Chem. Phys., 1996. **105**, 6778.

[60] Leforestier, C. & Wyatt, R. E. *Optical potential for laser induced dissociation*. J. Chem. Phys., 1983. **78**, 2334.

[61] Kosloff, R. & Kosloff, D. *Absorbing boundaries for wave propagation problems*. J. Comp. Phys., 1986. **63**, 363.

[62] Ashfold, M. N. R., Bennett, C. L., & Dixon, R. N. *Dissociation dynamics of* $NH_3(\tilde{A}\,^1A_2'')$. Faraday Discuss. Chem. Soc., 1986. **82**, 163–175.

[63] Yarkony, D. R. *Exploring molecular complexity: Conical intersections and* NH_3 *photodissociation*. J. Chem. Phys., 2004. **121**, 628–631.

[64] Biesner, J., Schneider, L., Schmeer, J., Ahlers, G., Xie, X., Welge, K. H., Ashfold, M. N. R., & Dixon, R. N. *State selective photodissociation dynamics of* $\tilde{A}$ *state ammonia. I*. J. Chem. Phys., 1988. **88**, 3607–3616.

[65] Bonhommeau, D. & Truhlar, D. G. *Mixed quantum/classical investigation of the photodissociation of* $NH_3(\tilde{A})$ *and a practical method for maintaining zero-point energy in classical trajectories*. J. Chem. Phys., 2008. **129**, 014,302.

[66] Hause, M. L., Yoon, Y. H., & Crim, F. F. *Vibrationally mediated photodissociation of ammonia: The influence of N-H stretching vibrations on passage through conical intersections*. J. Chem. Phys., 2006. **125**, 174,309.

[67] Wells, K. L., Perriam, G., & Stavros, V. G. *Time-resolved velocity map ion imaging study of* NH_3 *photodissociation*. J. Chem. Phys., 2009. **130**, 074,308.

[68] Tannenbaum, E., Coffin, E. M., & Harrison, A. J. *The far ultraviolet absorption spectra of simple alkyl amines*. J. Chem. Phys., 1953. **21**, 311–318.

[69] Herzberg, G. *Molecular spectra and molecular structure 3, Electronic spectra and electronic structure of polyatomic molecules*. Van Nostrand, Princeton, N.J., 1966, p. 170.

[70] Tang, S. L., Imre, D. G., & Tannor, D. *Ammonia: Dynamical modelling of the absorption spectrum*. J. Chem. Phys., 1990. **92**, 5919–5934.

[71] Lai, W., Lin, S. H., Xie, D., & Guo, H. *Full-dimensional quantum dynamics of* $\tilde{A}$*-state photodissociation of ammonia: Absorption spectra*. J. Chem. Phys., 2008. **129**, 154,311.

[72] Li, Z. H., Valero, R., & Truhlar, D. G. *Improved direct diabatization and coupled potential energy surfaces for the photodissociation of ammonia*. Theor. Chem. Acc., 2007. **118**, 9–24.

[73] Nangia, S. & Truhlar, D. G. *Direct calculation of coupled diabatic potential-energy surfaces for ammonia and mapping of a four-dimensional conical intersection seam*. J. Chem. Phys., 2006. **124**, 124,309.

[74] Sukiasyan, S. & Meyer, H. D. *On the effect of initial rotation on reactivity. A multi-configuration time-dependent hartree (MCTDH) wavepacket propagation study on the H + D and D + H reactive scattering systems*. J. Phys. Chem. A, 2001. **105**, 2604–2611.

[75] Giri, K., Chapman, E. L., Sanz, C. S., & Worth, G. A. unpublished results.

[76] Gatti, F., Otto, F., Sukiasyan, S., & Meyer, H. D. *Rotational excitation cross sections of para-*H_2 *+ para-*H_2 *collisions. A full-dimensional wavepacket propagation study using an exact form of the kinetic energy*. J. Chem. Phys., 2005. **123**, 1–13.

[77] Rabitz, H. & Aliş, O. F. *General foundations of high-dimensional model representations*. J. Math. Chem., 1999. **25**, 197–233.

[78] Vendrell, O., Gatti, F., Lauvergnat, D., & Meyer, H. D. *Full-dimensional (15-dimensional) quantum-dynamical simulation of the protonated water dimer. I. Hamiltonian setup and analysis of the ground vibrational state*. J. Chem. Phys., 2007. **127**, 1–17.

[79] Johnston, H. S. & Bertin, H. J. *Absorption and emission spectra of nitrosyl fluoride*. J. Mol. Spectroscopy, 1959. **3**, 683–696.

[80] Petrongolo, C., Scrocco, E., & Tomasi, J. *Minimal-basis-set LCAO-SCF-MO calculations for the ground state of* O_3*,* NO_2^-*, NOF and* OF_2 *molecules*. J. Chem. Phys., 1968. **48**, 407–411.

[81] J. Peslak, J., Klett, D. S., & David, C. W. *An* ab initio *molecular orbital study of the hydrogen, lithium and fluorine derivatives of nitric oxide*. J. Am. Chem. Soc., 1971. **93**, 5001–5005.

[82] Ditchfield, R., Bene, J. D., & Pople, J. A. *Molecular orbital theory of the electronic structure of organic compounds. XIV. Equilibrium geometries and energies of the low-lying excited states*. J. Am. Chem. Soc., 1972. **94**, 4806–4811.

[83] Vasudevan, K. & Grein, F. *Theoretical study on the vertical electronic spectrum of nitrosyl fluoride (ONF)*. J. Mol. Spec., 1977. **66**, 18–29.

[84] Suter, H. U., Huber, J. R., Dirke, M. V., Untch, A., & Schinke, R. *A quantum mechanical, time-dependent wave packet interpretation of the diffuse structures in the* $\mathrm{S}_0 \rightarrow \mathrm{S}_1$ *absorption spectrum of FNO: Coexistence of direct and indirect dissociation*. J. Chem. Phys., 1992. **96**, 6727–6734.

[85] Werner, H.-J., Knowles, P. J., Lindh, R., Manby, F. R., Schütz, M., *et al.*. *MOLPRO, version 2006.1, a package of ab initio programs*, 2006. See http://www.molpro.net.

[86] Lawlor, L. J., Vasudevan, K., & Grein, F. *Ab Initio Studies on the electronic structure of ONF (nitrosyl fluoride) and NOF (nitrogen hypofluorite)*. J. Am. Chem. Soc., 1978. **100**, 8062–8068.

[87] Magnuson, D. W. *Determination of the two-dipole moment components in nitrosyl fluoride*. J. Chem. Phys., 1951. **19**, 1071.

[88] Okabe, H. *Photochemistry of small molecules*. Wiley Interscience, New York, 1978.

[89] *JANAF Thermochemical tables*, volume 37 of *Natl. Stand. Ref. Data Ser.* Natl. Bur. Stand., US, second edition, 1971.

[90] Truhlar, D. G. & Horowitz, C. J. *Functional representation of Liu and Siegbahn's accurate* ab initio *potential energy calculations for* $H + H_2$. J. Chem. Phys., 1978. **5**, 2466–2476.

[91] McLaughlin, D. R. & Thompson, D. L. *Ground and lower excited state discrete ab initio electronic potential energy surfaces for doublet* HeH_2^+. J. Chem. Phys., 1979. **70**, 2748–2769.

[92] Joseph, T. & Sathyamurthy, N. *Three-dimensional quasiclassical trajectory study of the reaction* $He + H_2^+ \rightarrow HeH^+ + H$ *on an accurate ab initio potential-energy surface*. J. Chem. Phys., 1984. **80**, 5332–5333.

[93] Siegbahn, P. & Liu, B. *An accurate three-dimensional potential energy surface for* H_3. J. Chem. Phys., 1978. **68**, 2457–2465.

[94] Carney, G. D., Sprandel, L. L., & Kern, C. W. *Variational approaches to vibration-rotation spectroscopy for polyatomic molecules*. adv. Chem. Phys, 1978. **37**, 305–379.

[95] Lai, E. K. C. Master's thesis, Indiana University, 1975.

[96] Wrighton, M. S. *The photochemistry of metal carbonyls*. Chem. Rev., 1974. **74**, 401–430.

[97] Wrighton, M. S. & Geoffroy, G. *Organometallic photochemistry*. Academic Press, New York, 1974.

[98] Trushin, S. A., Fuß, W., Schmid, W. E., & Kompa, K. L. *Femtosecond dynamics and vibrational coherence in gas-phase ultraviolet photodecomposition of* $\mathrm{Cr(CO)_6}$. J. Phys. Chem. A., 1998. **102**, 4129–4137.

[99] Robb, M. A., Paterson, M. J., Hunt, P. A., & Takahashi, O. *Non-adiabatic direct dynamics study of chromium hexacarbonyl photodissociation*. J. Phys. Chem. A., 2002. **106**, 10,494–10,504.

[100] Trushin, S. A., Fuß, W., Kompa, K. L., & Schmid, W. E. *Femtosecond dynamics of* $Fe(CO)_5$ *photodissociation at 267 nm studied by transient ionization*. J. Phys. Chem. A, 2000. **104**, 1997–2006.

[101] Gray, H. B. & Beach, N. A. *The electronic structures of octahedral metal complexes. I. Metal hexacarbonyls and hexacyanides*. J. Am. Chem. Soc., 1963. **85**, 2922–2927.

[102] Beach, N. A. & Gray, H. B. *Electronic structures of metal hexacarbonyls*. J. Am. Chem. Soc., 1968. **90**, 5713–5721.

[103] Geoffroy, G. L. & Wrighton, M. S. *Organometallic Photochemistry*. Academic Press, New York, 1979.

[104] Trushin, S. A., Fuß, W., & Schmid, W. E. *Conical intersections, pseudorotation and coherent oscillations in ultrafast photodissociation of group-6 metal hexacarbonyls*. Chem. Phys., 2000. **259**, 313–330.

[105] Pierloot, K., Tsokos, E., & Vanquickenborne, L. G. *Optical spectra of* $Ni(CO)_4$ *and* $Cr(CO)_6$ *revisited*. J. Phys. Chem., 1996. **100**, 16,545–16,550.

[106] Pollak, C., Rosa, A., & Baerands, E. J. *Cr-CO photodissociation in* $Cr(CO)_6$*: Reassessment of the role of ligand-field excited states in the photochemical dissociation of metal-ligand bonds*. J. Am. Chem. Soc., 1997. **119**, 7324–7329.

[107] Jordan, R. B. *Reaction mechanisms of inorganic and organometallic systems*. Oxford University press, Oxford, 1991.

[108] Joly, A. G. & Nelson, K. A. *Femtosecond Transient Absorption Spectroscopy of* Cr(CO)$_6$ *in Methanol: Observation of Initial Excited States and CO Dissociation*. J. Phys. Chem., 1989. **93**, 2876–2878.

[109] Wang, L., Zhu, X., & Spears, K. G. *Unsaturated transition-metal complexes in solution: Naked* Cr(CO)$_5$ *in cyclohexane solution observed by picosecond IR transient absorption*. J. Am. Chem. Soc., 1988. **110**, 8695–8696.

[110] Villaume, S., Strich, A., Daniel, C., Perera, S. A., & Bartlett, R. J. *A coupled cluster study of the electronic spectroscopy and photochemistry of* $Cr(CO)_6$. Phys. Chem. Chem. Phys., 2007. **9**, 6115–6122.

[111] Frisch, M. J., Trucks, G. W., Schlegel, H. B., Scuseria, G. E., Robb, M. A., Cheeseman, J. R., Montgomery, J. A., Jr., Vreven, T., Kudin, K. N., Burant, J. C., Millam, J. M., Iyengar, S. S., Tomasi, J., Barone, V., Mennucci, B., Cossi, M., Scalmani, G., Rega, N., Petersson, G. A., Nakatsuji, H., Hada, M., Ehara, M., Toyota, K., Fukuda, R., Hasegawa, J., Ishida, M., Nakajima, T., Honda, Y., Kitao, O., Nakai, H., Klene, M., Li, X., Knox, J. E., Hratchian, H. P., Cross, J. B., Bakken, V., Adamo, C., Jaramillo, J., Gomperts, R., Stratmann, R. E., Yazyev, O., Austin, A. J., Cammi, R., Pomelli, C., Ochterski, J. W., Ayala, P. Y., Morokuma, K., Voth, G. A., Salvador, P., Dannenberg, J. J., Zakrzewski, V. G., Dapprich, S., Daniels, A. D., Strain, M. C., Farkas, O., Malick, D. K., Rabuck, A. D., Raghavachari, K., Foresman, J. B., Ortiz, J. V., Cui, Q., Baboul, A. G., Clifford, S., Cioslowski, J., Stefanov, B. B., Liu, G., Liashenko, A., Piskorz, P., Komaromi, I., Martin, R. L., Fox, D. J., Keith, T., Al-Laham, M. A., Peng, C. Y., Nanayakkara, A., Challacombe, M., Gill, P. M. W., Johnson, B., Chen, W., Wong, M. W., Gonzalez, C., & Pople, J. A. *Gaussian 03, Revision C.02*. Gaussian, Inc., Pittsburgh PA, 2003.

[112] Jost, A., Rees, B., & Yelon, W. *Electronic structure of chromium hexacarbonyl at 78K. I. Neutron diffraction study*. Acta Cryst. B, 1975. **31**, 2649–2658.